AD-A096 051 AIR FORCE INST OF TECH WRIGHT-PATTERSON AFB OH SCHOO--ETC F/G 11/3
LASER-INDUCED DAMAGE TO THIN FILM DIELECTRIC COATINGS.(U)
OCT 80 T W WALKER
UNCLASSIFIED AFIT/DS/PH/80-4 NL

1 OF 2
AD A
096051

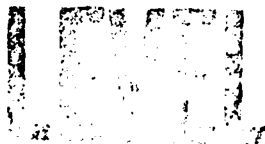

AFIT/DS/PH/80-4

AD A096051

LASER-INDUCED DAMAGE
TO THIN FILM DIELECTRIC COATINGS

DISSERTATION

Presented to the Faculty of the School of Engineering
of the Air Force Institute of Technology
Air University
in Partial Fulfillment of the
Requirements for the Degree of
Doctor of Philosophy

by
Thomas W. Walker, B.A., M.S.
Major USAF

DDC FILE COPY

Approved for public release; distribution unlimited

27 FEB 1981

FREDRIC C. LYNCH, Major, USAF
Director of Public Affairs

Air Force Institute of Technology (ATC)
Wright-Patterson AFB, OH 45433

81 3 06 072

AFIT/DS/PH/80-4

LASER-INDUCED DAMAGE

TO THIN FILM DIELECTRIC COATINGS

by

Thomas W. Walker, B.A., M.S.

Major USAF

Approved:

Co-chairman, ARTHUR H. GUENTHER	17 Nov 80
Co-Chairman, Philip E. Nielsen	17 Nov 80
GLENN R. DOUGHTY	19 Nov 80
JOHN H. ERKKILA	19 Nov 80
THEODORE E. LUKE	19 Nov 80
STANLEY R. ROBINSON	24 Nov. 80

Accepted:

J.S. PRZEMIENIECKI Dean, School of Engineering	19 Nov 80

PREFACE

Originally, when I began this research project, I was to study damage to thin film coatings as a function of laser wavelength. I had hoped that a careful experimental and theoretical study of the problem would clearly advance our knowledge of the damage process and provide invaluable data to the thin film community. As the project evolved and initial data taken, it became evident that the scope of the program had to be greatly expanded to include a study of laser pulse length and film thickness dependence of damage. Without such an expansion in scope it would not have been possible to uncover the dominant role of absorbing impurities in laser damage to thin films.

The capability of increasing the scope of this effort was due solely to the experimental knowledge of Dr. Arthur H. Guenther who proposed the original problem. I am indebted to his foresight of obtaining thin films in a variety of thicknesses and a laser system specially designed to operate at more than one pulse length. His guidance throughout the experimental evolution of this research was invaluable. I want to express my thanks to Maj. Phil Nielsen for his many helpful discussions on theoretical aspects of avalanche ionization, multiphoton absorption and impurity induced damage. While several useful products of our dialogue were published elsewhere and do not appear in this dissertation, the impurity theory is contained here. A special thanks is given to Mr. Charles Fry and Mr. Joel Jasso who assisted in taking enormous amounts of data and performing the computer analysis. Finally, my greatest thanks go to Judy, Jeff and Stacey for their moral support, understanding and unlimited patience.

CONTENTS

PAGE

PREFACE iii

LIST OF FIGURES vi

LIST OF TABLES. viii

ABSTRACT. ix

I. INTRODUCTION. 1

II. THEORY. 6

Background. 6

Avalanche Ionization. 6

Multiphoton Ionization. 11

Impurity Dominated Breakdown. 14

III. EXPERIMENT. 35

Experimental Arrangement. 35

Experimental Components 38

Optical Alignment 52

Sample Preparation. 53

Damage Threshold Determination. 53

IV. RESULTS 66

Damage Threshold Dependence on Film Thickness 68

Damage Threshold Dependence on Pulse Length 74

Damage Threshold Dependence on Wavelength 75

Observations on Damage Morphology 76

Comparison Between Theory and Experiment. 82

V. CONCLUSIONS 105

VI. UNRESOLVED QUESTIONS. 113

BIBLIOGRAPHY. 115

LIST OF FIGURES

FIGURE		PAGE
1	Damage Threshold vs. Laser Wavelength.	15
2	Approximate Solution of the Thermal Equations when q is Greater than 4	19
3	Approximate Solution of the Thermal Equations when q is Less than 4.	20
4	Exact Solution of the Thermal Equations Compared to the Approximate Solution for Metallic Impurities	24
5	Exact Solution of the Thermal Equations Compared to the Approximate Solution for Dielectric Impurities . . .	25
6	Mie Absorption Cross-sections for Exact Theory and Approximations	28
7	Damage Threshold vs. Impurity Size at 5 and 15 nanoseconds.	31
8	Damage Threshold vs. Laser Pulse Length for Fused Silica	32
9	Experimental Arrangement	36
10	Laser Profile in Time.	40
11	Vidicon Scan Pattern and Output.	42
12	Comparison of Vidicon Output and Damage Morphology in HfO_2.	46
13	Detail of Laser System	48
14	Laser Shot Pattern on the Sample	51
15	Residual Stress vs. Film Thickness in MgF_2	54

FIGURES		PAGE

16 Laser Pulse Truncation Due to Damage 57

17 Experimental Arrangement for Detecting Scattered Laser Light. 58

18 Change in Scattered Light Due to Damage. 59

19 Typical Raw Data for an Al_2O_3 Film 63

20 Standing Field Pattern in Air and Film for a HfO_2 Film. 67

21 MgO Damage Morphology vs. Wavelength 77

22 Oxide Damage Morphology at 0.26μm. 79

23 ThF_4 Damage Morphology vs. Wavelength. 80

24 Damage Threshold of ThF_4 at 1.06μm vs. Film Thickness. . 89

25 Damage Threshold of ThF_4 at 0.53μm vs. Film Thickness. . 90

26 Damage Threshold of ThF_4 at 0.35μm vs. Film Thickness. . 91

27 Damage Threshold of ThF_4 at 0.26μm vs. Film Thickness. . 92

28 Damage Morphology for Thick (1λ at 1.06μm) ThF_4 and MgF_2 Films. 95

29 Electron Micrograph of ThF_4 Damage Sites 96

30 Damage Threshold vs. Film Thickness for Al_2O_3 at 1.06μm. 97

31 Damage Threshold vs. Film Thickness for Al_2O_3 at 0.26μ 98

32 CaF_2 Damage Threshold vs. Laser Wavelength at Two Film Thicknesses 100

LIST OF TABLES

TABLE		PAGE
1	Theoretical Predictions of Damage Threshold with Laser Wavelength and Pulse Length	34
2	Analysis of MgF_2 Thin Film Coatings	55
3	CaF_2 and Al_2O_3 Damage Thresholds (J/cm^2)	69
4	MgF_2 and ThF_4 Damage Thresholds (J/cm^2)	70
5	ZrO_2 and MgO Damage Thresholds (J/cm^2)	71
6	HfO_2 and TiO_2 Damage Thresholds (J/cm^2)	72
7	SiO_2 Damage Thresholds (J/cm^2)	73
8	Evaluation of the Avalanche, Multiphoton and Impurity Models when Compared to the Experimental Data	110

ABSTRACT

The laser-induced damage thresholds of dielectric thin film coatings have been found to be more than an order of magnitude lower than the bulk material damage thresholds. Prior damage studies have been inconclusive in determining the damage mechanism which is operative in thin films. A program was conducted in which thin film damage thresholds were measured as a function of laser wavelength (1.06μm, 0.53μm, 0.35μm and 0.26μm), laser pulse length (5 and 15 nanoseconds), film material and film thickness. The large matrix of data was compared to predictions given by avalanche ionization, multiphoton ionization and impurity theories of laser damage. When Mie absorption cross-sections and the exact thermal equations were included into the impurity theory, excellent agreement with the data was found. The avalanche and multiphoton damage theories could not account for most parametric variations in the data. For example, the damage thresholds for most films increased as the film thickness decreased and only the impurity theory could account for this behavior. Other observed changes in damage threshold with changes in laser wavelength, pulse length and film material could only be adequately explained by the impurity theory. The conclusion which results from this study is that laser damage in thin film coatings results from absorbing impurities included during the deposition process.

I. INTRODUCTION

The importance of laser induced damage to optical thin film coatings has been recognized for a long time (1). High power laser systems used in fusion and high energy systems for weapons are required to operate over long periods of time without appreciable degradation in performance. The optical coatings employed in these lasers have proven to be very expensive and greatly impact the operation of the system. For example, the creation of even small damage sites within an optical coating can eventually degrade the beam quality enough to stop laser operation. Air Force programs in satellite communications and surveillance are similarly affected by this same problem and a great deal of resources are expended each year in an attempt to improve thin film coating technology.

The Air Force has funded many efforts to develop improved coatings, however, the factors affecting laser induced damage of coatings for a wide range of laser wavelengths and operating conditions are still not well understood. Much of the research has been devoted to studying thin film damage in the relatively long pulse regime (longer than 100 nanoseconds) and for continuous wave (CW) laser operation. Although many systems of interest to the Air Force operate under these conditions, short pulse lasers have become increasingly important. In addition there has been a strong thrust to develop lasers which operate at shorter wavelengths (visible). This trend is driven in a large part by the requirement for smaller and more efficient optical systems. Unfortunately, when the size of the optics is reduced the coatings must withstand even higher power or energy loadings and in many cases suitable coatings do not exist.

In order to develop quality coatings, we must understand the fundamental damage processes and how they vary with laser wavelength and pulse length. The three principal processes by which the laser energy can be coupled into the thin film material are avalanche ionization, multiphoton ionization and absorption by impurities in the films. Avalanche ionization occurs when an electron in the conduction band of the material absorbs enough energy from the electromagnetic field to impact ionize a valance electron. The two electrons can undergo the same process to produce four conduction electrons and so on. The number density of electrons in the conduction band grows exponentially with time until a plasma is formed. The plasma more efficiently absorbs energy from the electromagnetic field and catastrophic damage to the material occurs. Multiphoton ionization can also produce a plasma, however, in this case the electrons are promoted from the valance to the conduction band by direct absorption of two or more photons. The number of photons required for each ionization depends on the bandgap of the material and the laser wavelength. Impurity dominated damage is a thermal process and takes place when an impurity in the film absorbs enough laser radiation to produce melting or fracture of the host material.

An extensive amount of research has been conducted in an attempt to validate one or another of the theories. The research usually involved studying breakdown as a function of laser wavelength (2-15), pulse length (16-19), or film thickness (20-24). Historically, the wavelength dependence of laser damage has been used as the main theoretical testing ground (2-15, 25-26). In part this is because avalanche and multiphoton ionization theories predict conflicting laser wavelength dependencies.

while current theories of impurity dominated damage predict no wavelength dependence.

The original objective of this research was to obtain experimental data on the breakdown of thin film coatings at laser wavelengths ranging from the near infrared (1.06μm) to the ultraviolet (0.26μm). Carefully obtained experimental data did not exist for such a wide range of laser wavelengths, or at all for many of the materials tested in this research. The intent of this effort was to compare the results to the various theories of breakdown and explain the frequency dependence of breakdown in thin film coatings. However, initial work on the theories soon indicated that this would not be a fruitful approach. For example, one major effort was to properly include the Mie absorption coefficient into an impurity breakdown model, and for the first time use the exact solution to the thermal equations in the model. When this was done there was no longer a clear, definitive and qualitative distinction between the wavelength predictions of the multiphoton and impurity models. This lack of distinction comes about because the materials can only be tested at a few discrete points across the frequency spectrum (because of available lasers) and as will be shown later, both theories predict a general decrease in damage threshold with an increase in laser frequency. Further, a careful examination of the theories revealed that the pulse length dependence of breakdown was also an inconclusive test of any theory when studied as a single parameter in breakdown. It is shown in this work that the pulse length dependence is a measure of the magnitude of the energy loss mechanisms and can vary from a very weak to a very strong dependence in all of the theories.

These results served to point out that studies of breakdown as a function of only one parameter can not uncover the dominant mechanism of laser damage. In fact, single parameter studies have often engendered controversy, a fact supported by numerous publications in which the conclusions drawn from experimental data are in total conflict (7, 9, 26, 27).

Unfortunately, it is not possible to correlate the results of past research to obtain a multi-parameter study of the breakdown process. Each individual experiment was performed on a different set of films and usually under different experimental conditions. The films varied in method of substrate preparation, film thickness, quality of starting materials and deposition technique. The last two conditions are of vital importance in determining the type, size, distribution and quantity of impurities in a film.

With these facts in mind, the objective of this research took on a new direction, to conduct a multi-parameter study of the breakdown process under controlled conditions which would allow a correlation of all the data. The parameters that were varied were laser wavelength, pulse length, thin film thickness, and thin film materials. Although a few two-parameter studies have been conducted in the past (5, 17, 18, 26), these have been very limited in the amount of data that was taken. Standard techniques of determining the peak laser intensity during a single firing often takes hours or days to analyze. To obtain the large amount of data reported in this work, a new technique was devised which could provide the results in a matter of minutes. Over 8000 data points were acquired, which would have taken 5 to 10 years by conventional methods.

The result was not just a multi-parameter experiment, but a very comprehensive multi-parameter experiment. It was found that the only damage process which could consistantly fit with the experimental results was impurity induced damage. Although this mechanism has been argued for in the past, it had never been convincingly demonstrated.

The body of this dissertation is divided into six sections. The second section is devoted to presenting the theoretical models of laser induced damage. Each theory is discussed in terms of the predicted behavior of breakdown with a variation in the major parameters. Section III gives the experimental arrangement and technique. The sample preparation and experimental error analysis is also discussed. Section IV presents the experimental results and a comparison of the data with each of the theoretical models. The fifth section is devoted to conclusions and discussion of the results. The last section highlights the major unresolved issues and gives recommendations for future research.

II. THEORY

Background

The theoretical treatment of laser induced damage to dielectric materials has followed the three distinct paths of avalanche ionization, multiphoton ionization, and impurity induced damage. Over the past two decades there has been a concerted effort to compare the theoretical predictions of these three treatments with experimental data. Unfortunately, each of the theories is subject to uncertainties which make accurate calculations of absolute damage thresholds difficult. Both avalanche and multiphoton ionization calculations require parameters such as the material band structure and electron effective mass which are often not available for many dielectrics. The impurity model requires a detailed knowledge of types, size, and distribution of impurities in the host material which are also unknown at the present time. Because of these limitations it is impossible to calculate from first principles damage thresholds by each of these theoretical descriptions. One way to determine the most appropriate model would be to compare their predictive parametric variation of damage with laser pulse width, wavelength, and film properties. Specifically, this section will deal with the predictions of each theory of variations in the critical or damaging energy density with changes in the laser pulse width and wavelength.

Avalanche Ionization

The fundamental approach to avalanche ionization is to calculate the time evolution of the electron distribution function $f(\bar{p})$ and then obtain the electron ionization rate. The theoretical calculations

start with a quantum kinetic equation, the most general form of which has been given by Epshtein (28) with an equivalent expression by others (29, 30). Epshtein's equation is

$$\frac{\partial f(\bar{p},t)}{\partial t} = 2\pi \sum_{K} |C_K|^2 \sum_{\ell=-\infty}^{\infty} J_\ell^2\left(\frac{eE_0 k}{m\hbar^2 w^2}\right) X$$

$$\left\{\left[f_{\bar{p}+\bar{K}}(N_K+1) - f_{\bar{p}} N_K\right]\delta(\mathcal{E}_{\bar{p}+\bar{K}} - \mathcal{E}_p - \hbar w_K - \ell\hbar w) + \right. \quad (1)$$

$$\left.\left[f_{\bar{p}-\bar{K}} N_K - f_{\bar{p}}(N_K+1)\right]\delta(\mathcal{E}_{\bar{p}-\bar{K}} - \mathcal{E}_{\bar{p}} + \hbar w_K - \ell\hbar w)\right\}$$

where c_k is the matrix element for the electron-phonon interaction; J_ℓ is a Bessel function of order ℓ; E_0 is the opto-electric field amplitude; k is the phonon momentum; $\bar{p}$ is the electron momentum; w is the frequency of the electric field; N_k is the number density of phonons; ε is the electron energy. At present an analytical solution to equation (1) has not been obtained even though an approach has been put forth by Keldysh (31).

Epifanov (3, 7, 32, 35) reduced equation (1) to an energy diffusion equation with the conditions, $w \ll E_g$ where E_g is the material bandgap energy and $\Delta\varepsilon\ \partial f/\partial\varepsilon \ll f(\varepsilon)$. The first condition is valid for the large bandgap dielectrics. However, the condition is not satisfied for the smaller bandgap materials (E_g<6ev) at the short (2600Å) wavelength. The second condition requires that the electron distribution function not change significantly during the energy absorption process. Thus, the gain in energy as a result of the electron-phonon-photon

process must be small compared to the electron energy. Again this condition is valid for the large bandgap materials. The diffusion equation can then be solved with the assumed steady state solution.

$$f(\varepsilon,t) = f(\varepsilon)\, e^{\gamma t} \tag{2}$$

where γ is the ionization rate for the avalanche process. The final expression for the critical field is given by equation (3).

$$E_c^2 = \frac{G E_g m^2 V_s}{K T e^2}\left(W^2 + \frac{E_g}{m L_{ac}^2}\right)\frac{1}{\ln\left(\frac{t_p}{L\Theta}\right)} \tag{3}$$

where V_s is the velocity of sound in the solid; L_{ac} is the mean free path between electron-acoustic phonon collisions; L is the number of electron regenerations; and t_p is the laser pulse length (full width at half maximum). θ is a function of material parameters and the electric field strength. However, since θ occurs within the natural logarithm, it has only a small effect on the critical field breakdown, for reasonable ranges of the parameter.

It can be seen from equation (3) that the dependence of the breakdown field on the laser pulsewidth t_p is weak. The physical significance of this can be gleaned by recasting the critical field into the critical energy per unit area, which is the total energy utilized in

the breakdown process. The energy per unit volume is given by $(1/2)\varepsilon_0 E^2$. The total energy per unit area which is incident on the breakdown volume is $1/2\varepsilon_0 E^2 c t_p$, where c is the speed of light. We have

$$(\mathrm{ENERGY/AREA})_{critical} \propto \frac{t_p}{\ln(t_p)} \tag{4}$$

which is a strong function of the pulse width. The fact that the process depends so strongly on the rate that the energy is deposited implies that energy loss mechanisms are important. Thus equation (3) gives a solution for the damaging field when electron energy losses are high.

Two alternate derivations of the critical field have been given by Molchanov (2) and Zakharov (33). Molchanov's result is

$$E_c^2 = \frac{160\pi n^2 \sqrt{E_g}\, \rho V_s W^2}{e^2 \sqrt{2m}\, t_p K T E_1^2} \tag{5}$$

where n is the refractive index of solid E_1 is the strain energy constant for acoustic phonons. On the other hand Zakharov's formulation gives

$$E_c^2 = \frac{m^2 V_s^2 W^2 E_g}{e^2 K T} \frac{1}{\ln\left(\frac{t_p}{L\theta'}\right)} \tag{6}$$

where

$$\theta' = \frac{5\pi^{3/2}\sqrt{2}\, e^2 \rho \hbar^4 (KT)^{3/2} E_c^3}{U_\ell^3 W^3 m^{1/2} E_1^2 E_g^2}$$

It is clear that equations (6) and (3) are very similar if w^2 is much greater than E_g/mL_{ac}^2, the electron-phonon collision frequency in equation (3).

In equation (5) the critical energy per unit area is independent of pulse length. This would seem to be in conflict with the other two equations. However, both Zakharov (33) and Epifanov (32) noted that their respective formulations reporduced equation (5) if $m^2V_s^2w^2E_g/e^2E^2kT$ was much less than one. This limit must be taken in the expressions for the electron distribution function before the diffusion equation is solved. It can be shown that the quantity $m^2V_s^2w^2E_g/e^2E^2kT$ is directly proportional to the ratio of the power loss due to spontaneous emission of phonons to the coefficient of electron diffusion along the energy axis (32). It is exactly this energy loss by electrons to phonons which gives the strong time dependence of the critical energy per unit area. Equation (5) represents the "no energy loss" solution and equations (3) and (6) are the "high energy loss" solutions. The expression $m^2V_s^2w^2E_g/e^2E^2kT$ indicates that the "no energy loss" condition is not valid for dielectric materials unless the temperature exceeds several hundred degrees C. Results obtained by Manenkov (25) on the temperature dependence of breakdown were compared to equation (3) and good agreement was found, which also supports the Epifanov treatment of avalanche ionization. The conclusion is that, for dielectric materials tested in this dissertation, the expected laser pulse length dependence of the damaging energy denisty is approximately linear as given by equation (4).

The predicted dependence of breakdown on the laser frequency is identical for the equations (3), (5) and (5) when E_g/mL_{ac}^2, the square

of the electron-phonon collision frequency, in equation (3) is much less than w^2. The breakdown field clearly increases with higher laser frequency. When the above condition is not met, then by equation (3), the functional dependence on laser frequency is weaker. Thus, depending on the magnitude of E_g/mL_{ac}^2, the predicted frequency dependence varies from no dependence ($E_g/mL_{ac}^2 >> w^2$) to an w^2 dependence ($E_g/mL_{ac}^2 << w^2$).

The laser pulse width and wavelength dependencies of damage will now be examined in a multiphoton breakdown theory.

Multiphoton Ionization

Bloembergen (34) postulated that when the photon energy of the damaging light was about a third of the bandgap energy (E_g) of the solid then multiphoton absorption could contribute significantly to the breakdown process. As a result the damage threshold would go down as the laser frequency was increased beyond an equivalent photon energy of $E_g/3$. A number of experiments in bulk materials have been directed toward verifying this trend (4, 7-11, 13-17, 35). At present, in bulk solids, there seems to be some substantiation that a decrease in breakdown threshold does occur (4).

The analytic difficulties of treating multiphoton absorption in solids are comparable to those of avalanche ionization. Many theoretical treatments have been given for two-photon absorption in semiconductors (35-38, 41) where the band parameters and structure are well known. There has been no theoretical work for dielectrics, where the band structure is often unknown. Standard perturbation techniques have been used to treat up to three photon processes, however, at this level, comparison with experiment becomes almost impossible. Again, this is due mainly to a lack of knowledge of the band structures.

There are several treatments of photon absorption to all orders (39, 40, 43), of which the most widely used is that of Keldysh (39). Although the main reason for this wide use is that the final equations are simple enough to obtain numerical results without lengthy and complex computations, there are more important aspects. The Keldysh theory gives in most cases the best agreement with experiment (44). For high order absorption (greater than three) it is the only theory that can be used at present to obtain meaningful numerical results when compared to experiments. It has been stated that the Keldysh formula is only valid for high order photon absorption (35, 40, 42-44). Comparison with experimental data for one and two photon absorption indicates that this is not the case (41). Vaidyanathan and this author have shown that the Keldysh formula reduces to the well known result (46) for one photon absorption. Thus, the Keldysh formula gives meaningful results for first and higher order photon processes and will be used as a comparison with the experimental data in this thesis.

The general Keldysh formula for the ionization rate is (39)

$$\frac{1}{\tau} = \frac{2W}{9\pi}\left(\frac{mW\sqrt{1+\gamma^2}}{\hbar\gamma}\right)^{3/2} Q\left(\gamma, \frac{\tilde{E}_g}{\hbar W}\right) \exp\left\{-\pi\left\langle \frac{E}{\hbar W} + 1 \right\rangle\right. \times \left[K\left(\frac{\gamma}{\sqrt{1+\gamma^2}}\right) - E^*\left(\frac{\gamma}{\sqrt{1+\gamma^2}}\right)\right] \Bigg/ E^*\left(\frac{1}{\sqrt{1+\gamma^2}}\right) \qquad (7)$$

where $\gamma = w(\sqrt{mE_g})/eE$; E_g is the bandgap energy; K and E^* are elliptic integrals of the first and second kind; $\tilde{E}_g$ is given by

$$\tilde{E}_g = \frac{2}{\pi} E_g \frac{\sqrt{1+\gamma^2}}{\gamma} E^*\left(\frac{1}{\sqrt{1+\gamma^2}}\right)$$

The symbol <x> denotes the integer part of x. Finally,

$$Q(\gamma,X) = \left[\pi/2K\left(\frac{1}{\sqrt{1+\gamma^2}}\right)\right] \times \sum_{n=0}^{\infty} \exp\left\{-\pi\left[K\left(\frac{\gamma}{\sqrt{1+\gamma^2}}\right) - E^*\left(\frac{\gamma}{\sqrt{1+\gamma^2}}\right)\right] n \Big/ E^*\left(\frac{1}{\sqrt{1+\gamma^2}}\right)\right\} \times \Phi\left\{\left[\pi^2(2\langle X+1\rangle - 2X+n)\Big/2K\left(\frac{1}{\sqrt{1+\gamma^2}}\right)E^*\left(\frac{1}{\sqrt{1+\gamma^2}}\right)\right]^{\frac{1}{2}}\right\} \quad (8)$$

$\Phi(z)$ is the Dawson integral given by

$$\Phi(z) = \int_0^z e^{Y^2 - z^2}\, dY$$

For breakdown fields $E \approx 10^6$ volts/cm, γ is much greater than one and equation (7) reduces to

$$\frac{1}{\tau} = \frac{2W}{9\pi}\left(\frac{mW}{\hbar}\right)^{3/2} \Phi\left[\left(2\left\langle\frac{\tilde{E}_g}{\hbar W}+1\right\rangle - 2\frac{\tilde{E}_g}{\hbar W}\right)^{1/2}\right] \times \exp\left\{2\left\langle\frac{\tilde{E}_g}{\hbar W}+1\right\rangle\left(1-\frac{e^2E^2}{4mW^2E_g}\right)\right\}\left(\frac{e^2E^2}{16mW^2E_g}\right)^{\left\langle\frac{\tilde{E}_g}{\hbar W}+1\right\rangle} \quad (9)$$

The breakdown criteria can be taken as

$$\frac{1}{\tau}(t_p) = \text{critical electron density} \quad (10)$$

where t_p is the laser pulse width and τ is the electron transition rate (39). The critical electron density is not as important as the predicted behavior of breakdown with laser pulse length and wavelength. Equation (9) can be simplified by noting that in general $e^2E^2/4mw^2E_g$ is much less than 1. The dependence of the critical energy per unit area on the pulse width becomes

$$(\text{ENERGY/AREA})_c \propto \frac{(t_p)}{(t_p)^{\langle \frac{E_g}{\hbar w} + 1 \rangle}} = (t_p)^{1 - \frac{1}{\langle \frac{E}{\hbar w} \rangle + 1}} \quad (11)$$

From (11) we can see that if E_g is less than $\hbar w$, the breakdown process is time independent. For very high order photon processes, E_g much greater than $\hbar w$, the process depends linearly on time. This would be indicative of a high energy loss regime, except in the case of multi-photon absorption, where it would be more appropriately called a regime of low energy utilization.

The wavelength dependence contained in equation (9) is complicated. A computer program was written during this research to plot the breakdown field dielectric materials as a function of wavelength. The results are shown in Figure (1). Also, included in the figure are the avalanche model and a combined avalanche and multiphoton model predictions. Clearly, the multiphoton theory predicts a decrease in the breakdown field as the laser frequency increases.

Impurity Dominated Breakdown

There has been a great deal of theoretical work on damage produced by impurities in the host material (47-76). Even now it is not clear that damage in very pure bulk materials is produced by avalanche or multiphoton ionization as opposed to isolated impurity sites (75). Experimental data (17, 18, 26, 38, 75) confirms a spot size of breakdown that is difficult to explain by either multiphoton or avalanche ionization. In thin films the importance of impurities is expected to

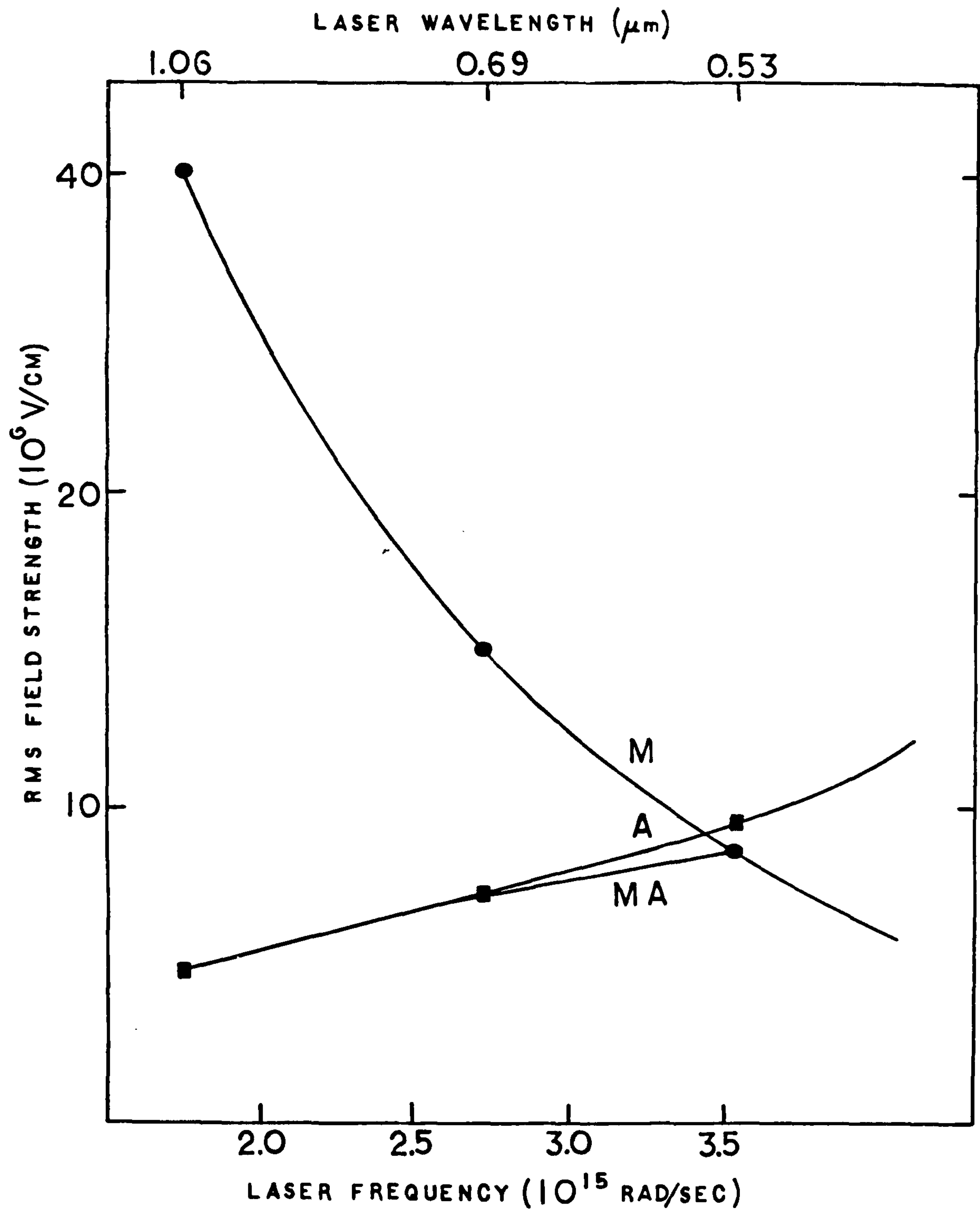

Figure 1. Damage Threshold vs. Laser Wavelength

be even greater. For example, the absorption coefficient of most thin films is between 10 cm^{-1} to 1000 cm^{-1}, and in bulk form the range is several orders of magnitude smaller. Surface absorption falls in between these two extremes. The high absorptivity of thin films is generally attributed to impurities which are included during the deposition process. Experimental data also shows that the breakdown threshold can be more than an order of magnitude lower for thin films than for the bulk form of the same materials.

The model which was developed in this research for impurity damage is that of spherical absorbing particles embedded in a host material. The impurity is assumed to absorb the incident radiation and then heat up. A straightforward solution to the thermal equations can be obtained by assuming that the heat flow out of the particle is determined only by the thermal conductivity of the host material. This assumption is true if the thermal conductivity of the impurity is infinite, in which case the temperature within the impurity is uniform. The appropriate thermal equations are given by equations (12) and (13).

$$\frac{d^2(r\bar{T})}{dr^2} - q^{*2}(r\bar{T}) = 0 \qquad r > a \qquad (12)$$

$$MC_pS\bar{T}' - \iint \frac{\partial \bar{T}'}{\partial r} dr = \frac{QI}{S} \qquad r \leq a \qquad (13)$$

$T(r,s)$ and $T^1(r,s)$ are the Laplace transformed temperatures with respect to time inside and outside of an impurity of radius a. We have the following definitions: M is the mass of the impurity; C_p specific heat

density; K_h is the thermal conductivity of the host material; $q^* = (s/D_h)^{1/2}$ where D_h is the thermal diffusivity of the host material; Q is the absorption cross-section; J is the incident laser intensity; s is the Laplace transform variable.

Equation (13) is an energy conservation equation which replaces the diffusion equation inside the impurity when a uniform temperature distribution is assumed. The solution is straightforward and the result has been given by Hopper and Uhlmann (47) for metallic impurities in a dielectric material. The temperature in the host is

$$T = \frac{3QI}{2C_pD_h m r}\left\{\frac{1}{q-m}\operatorname{erfc}\frac{r-a}{2(D_h t_p)^{1/2}} - \frac{1}{q+m}\operatorname{erfc}\frac{r-a}{2(D_h t_p)^{1/2}}\right. \quad (14)$$

$$-\frac{1}{q-m}\exp\left[\frac{(q-m)(r-a)}{2a}+\frac{(q-m)^2D_h t_p}{4a^2}\right]\operatorname{erfc}\left[\frac{r-a}{2(D_h t_p)^{1/2}}+\frac{(q-m)(D_h t_p)^{1/2}}{2a}\right]$$

$$\left.+\frac{1}{q+m}\exp\left[\frac{(q+m)(r-a)}{2a}+\frac{(q+m)^2D_h t_p}{4a^2}\right]\operatorname{erfc}\left[\frac{r-a}{2(D_h t_p)^{1/2}}+\frac{(q+m)(D_h t_p)^{1/2}}{2a}\right]\right\}$$

Inside the impurity we have

$$T_p = \frac{3QI}{2C_pD_h m a}\left\{\frac{1}{q-m}\left[1-\exp\left(\frac{D_h t_p(q-m)^2}{4a^2}\right)\operatorname{erfc}\left(\frac{(q-m)(D_h t_p)^{1/2}}{2a}\right)\right]\right. \quad (15)$$

$$\left.-\frac{1}{q+m}\left[1-\exp\left(\frac{D_h t_p(q+m)^2}{4a^2}\right)\operatorname{erfc}\left(\frac{(q+m)(D_h t_p)^{1/2}}{2a}\right)\right]\right\}$$

C_p is the volume specific heat; $q = 3C_h/C_p$ and $m = (q(q-4))^{1/2}$. Equation (15) is the result that has been often used in impurity damage work (47, 54, 76). Note that equation (15) is not valid for q less than or equal to 4. For q greater than 4 we must have C_h greater than $(4/3)C_p$ which is usually the case for metallic impurities in glass. If q is less than 4 the correct solution derived by this author is

$$T_p = \frac{3QI}{\pi a C_p D_h (q^2 + m^2)} \Bigg\{ 1 + \exp\left(\frac{(q^2-m^2)D_h t_p}{4a^2}\right) \operatorname{erfc}\left(\frac{q(D_h t_p)^{1/2}}{2a}\right) \times$$

$$\left[\frac{q}{m} \sin\left(\frac{2qmD_h t_p}{4a^2}\right) - \cos\left(\frac{2qmD_h t_p}{4a^2}\right)\right] + \frac{2}{\sqrt{\pi}} \exp\Bigg[\frac{(q^2-m^2)D_h t_p}{4a^2} \qquad (16)$$

$$- \left(\frac{q(D_h t_p)^{1/2}}{2a}\right)^2\Bigg] \Bigg[\int_0^{\frac{m\sqrt{D_h t_p}}{2a}} e^{-Y^2} \Big[\sin\left(\frac{2Yq(D_h t_p)^{1/2}}{2a} - \frac{2qmD_h t_p}{4a^2}\right)$$

$$- \frac{q}{m} \cos\left(\frac{2Yq(D_h t_p)^{1/2}}{2a} - \frac{2qmD_h t_p}{4a^2}\right)\Big] dY \Bigg] \Bigg\}$$

It can be shown that under the proper limiting process that both equation (15) and the correct equation for q = 4 are obtained from equation (16). In equation (16) m equals $(q|q-4|)^{1/2}$.

Figures (2) and (3) show plots of equations (15) and (16) respectively. These plots represent the energy per unit area incident on the impurities required to raise the impurity temperature to 2000°K. For simplicity, the cross-section Q has been taken to be equal to one. Both equations give meaningless results when the impurity size is less than some critical value because of the assumption that the temperature is uniform within the particle. If r^2 is much greater than $D_h t_p$, where r is the radius of the impurity, then the internal temperature should be approximately uniform. However, if r^2 is less than $D_h t_p$, then the thermal diffusion rate out of the impurity becomes

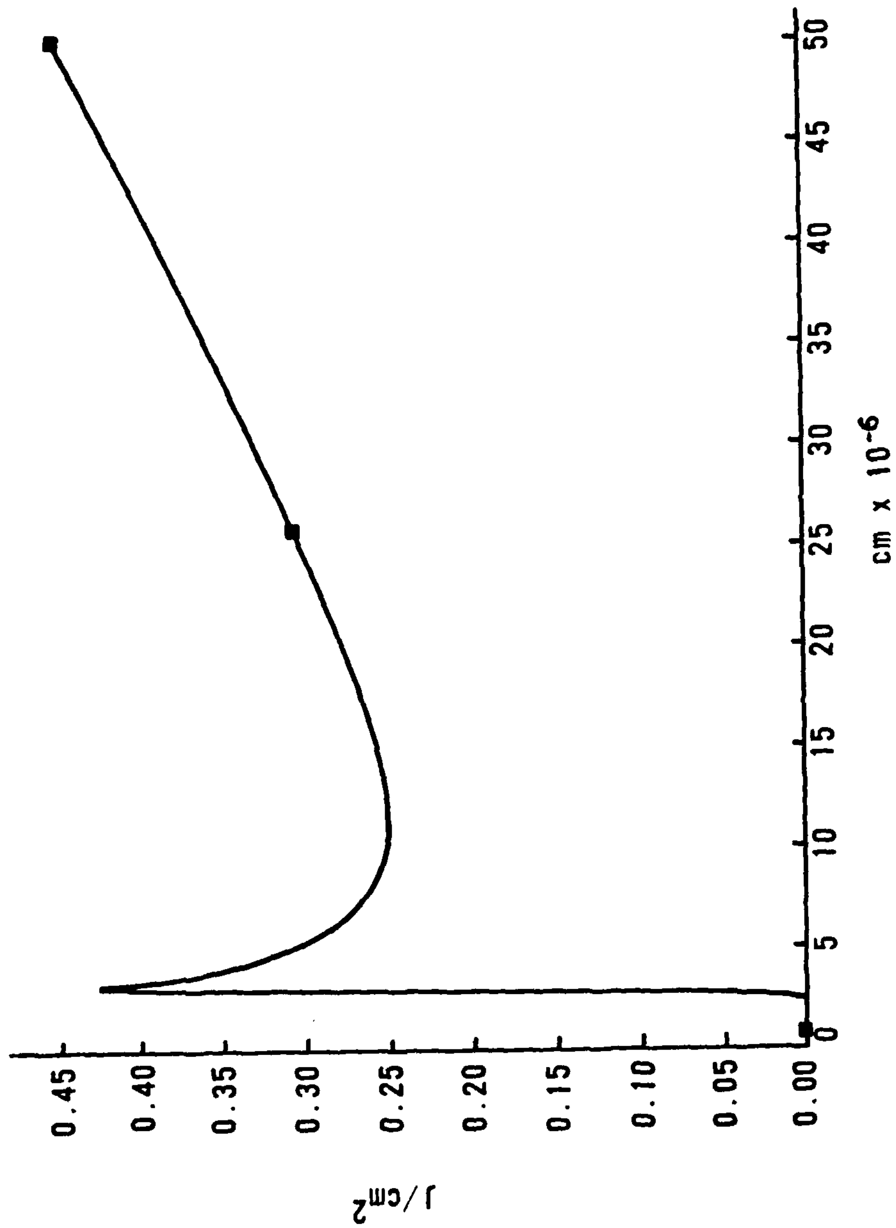

Figure 2. Approximate Solution of the Thermal Equations when q is Greater than 4

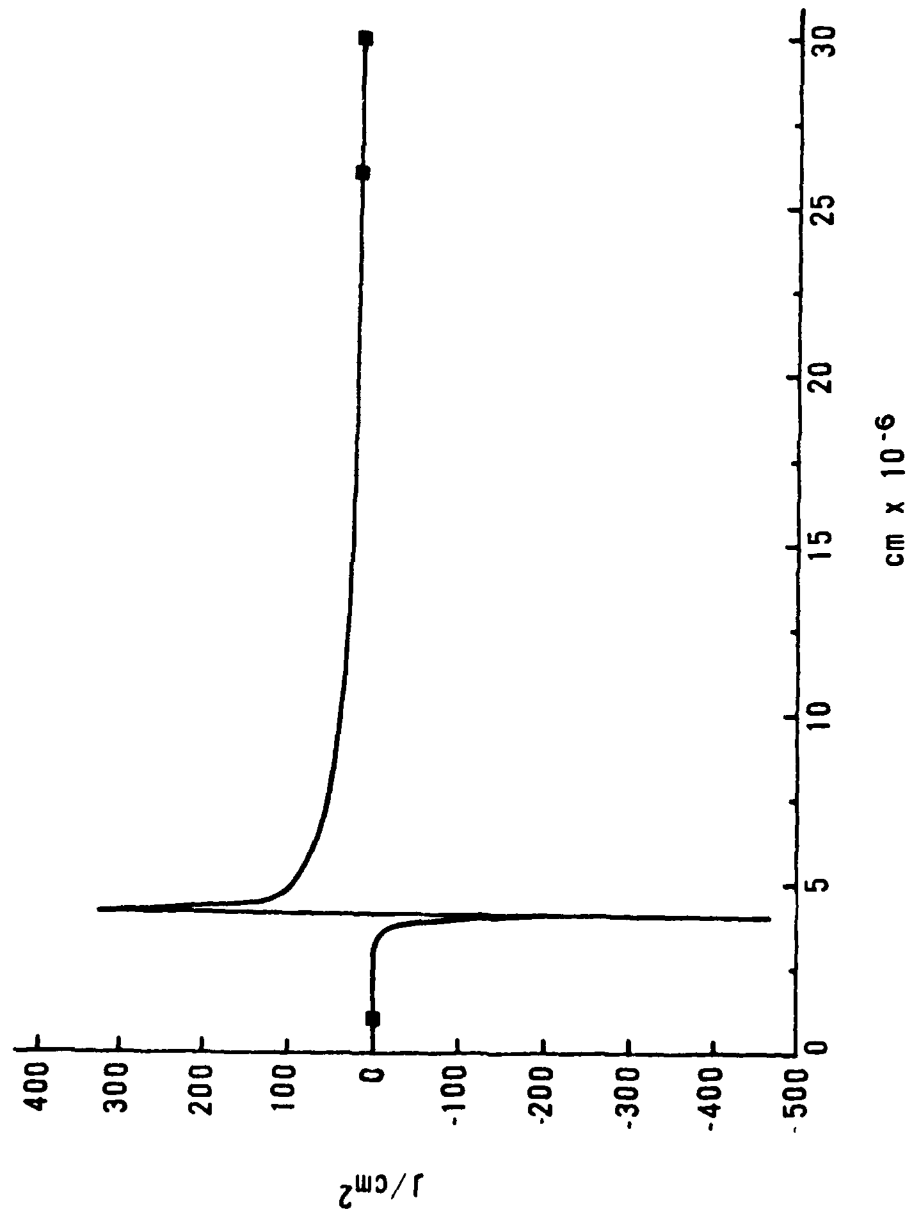

Figure 3. Approximate Solution of the Thermal Equations when q is Less than 4

great enough to make the uniform temperature assumption invalid. The points on the plots at which the equations are badly behaved correspond exactly to a non-uniform particle temperature. The equations have been checked to insure that the observed effect is a result of the equations and not due to a computer generated error. Examination of the figures would seem to imply that the range for which the equations are invalid is not significant. The size of the particles that are easiest to damage are larger than where the discontinuities occur. However, if we assume that the largest size impurities which can occur in the thin film has a diameter equal to the film thickness, then for very thin films the invalid range of the equations is important. For example, a 2600Å thick film would contain only 2600Å diameter impurities and smaller. There is evidence that this last assumption is valid (77), and is one of several reasons why equations (15) and (16) must be used carefully when applying them to thin films.

Recent research (77, 78) indicates that the impurities in fluoride thin films are oxides. For example, thorium fluoride (ThF_4) contains ThO_2 and/or $ThOF_2$. Oxides and other dielectric materials typically have a very small coefficient of thermal diffusivity (79). The small coefficient violates the basic assumption made in obtaining equations (15) and (16), and these equations can not be used in treating dielectric impurities in dielectric host materials.

In light of the above discussion, an exact solution is required to the thermal equation for spherical impurities. The exact thermal equations are given in equations (17) and (18).

$$\frac{d^2(r\bar{T}')}{dr^2} - \frac{Sr\bar{T}'}{D_p} = -\frac{rQI}{K_pS} \qquad o \leq r < a$$
$$\frac{d^2(r\bar{T})}{dr^2} - \frac{Sr\bar{T}}{D_h} = 0 \qquad r > a \tag{17}$$

$$\bar{T} = \bar{T}'$$
$$K_p\frac{d\bar{T}'}{dr} = K_h\frac{d\bar{T}}{dr} \qquad r = a \tag{18}$$

Where $\bar{T}^1$ is the Laplace transformed temperature. The solution to these equations was obtained by Goldenberg and Trantor (80). The result is

$$T = \frac{a^2QI}{K_p}\left\{\frac{1}{3}\frac{K_p}{K_h} + \frac{1}{6}\left(1 - \frac{r^2}{a^2}\right) - \frac{2ab}{r\pi}\int_0^{\infty} e^{-\frac{\gamma^2 t_p}{\gamma_1}} \frac{(\mathrm{SIN}\gamma - \gamma\mathrm{COS}\gamma)(\mathrm{SIN}(r\gamma/a))d\gamma}{[(c\,\mathrm{SIN}\gamma - \gamma\mathrm{COS}\gamma)^2 + b^2\gamma^2\mathrm{SIN}\gamma]}\right. \tag{19}$$

Where $\gamma_1 = a^2/D_p$, $c = 1-(K_h/K_p)$, $b = (K_h/K_p)(D_p/D_h)^{1/2}$. The exponential in equation (19) which involves time, contains D_pt_p/a^2, where

equations (15) and (16) contain $D_h t_p/a^2$. Since the integration in equation (19) is from zero to infinity, it is easy to make a change of variable and cast (19) into the same form as (15) and (16). Figure (4) shows a plot of the incident energy per unit area required to heat a particle's boundary (r = a) to a temperature of $2000^{o}K$ as a function of the particle size. Curves (1) and (2) are equations (15) and (19) respectively. The material parameters are for a typical metallic impurity in a glass host material. As expected the agreement between equations (15) and (19) is excellent over the range of impurity sizes that were used. Figure (5) shows a comparison of equation (19) (curve 1) and equation (16) (curve 2). The material parameters are for dielectric impurities and q less than 4. In this case very poor agreement is found between the two equations. This is a result of the uniform temperature assumption made in obtaining equation (16).

The integral in equation (19) converges rapidly and remains well behaved for all values of the impurity size, so there are no practical reasons for using equations (15) or (16) instead of (19). It is clear to the author that the Goldenberg and Trantor (80) solution to the thermal equations is not known to researchers working in the field of laser induced damage. This fact is pointed out by observing that in the work on impurity dominated damage (50-76), there is no reference to this solution. However, in the research cited there are many references to the solution of Hopper and Uhlmann (2), given by equation (15).

To date, every treatment of impurity dominated breakdown has used an assumed constant for the absorption cross-section Q. This is only valid if the impurity is much greater in size than the wavelength of incident radiation. In the case of thin films the impurity size is

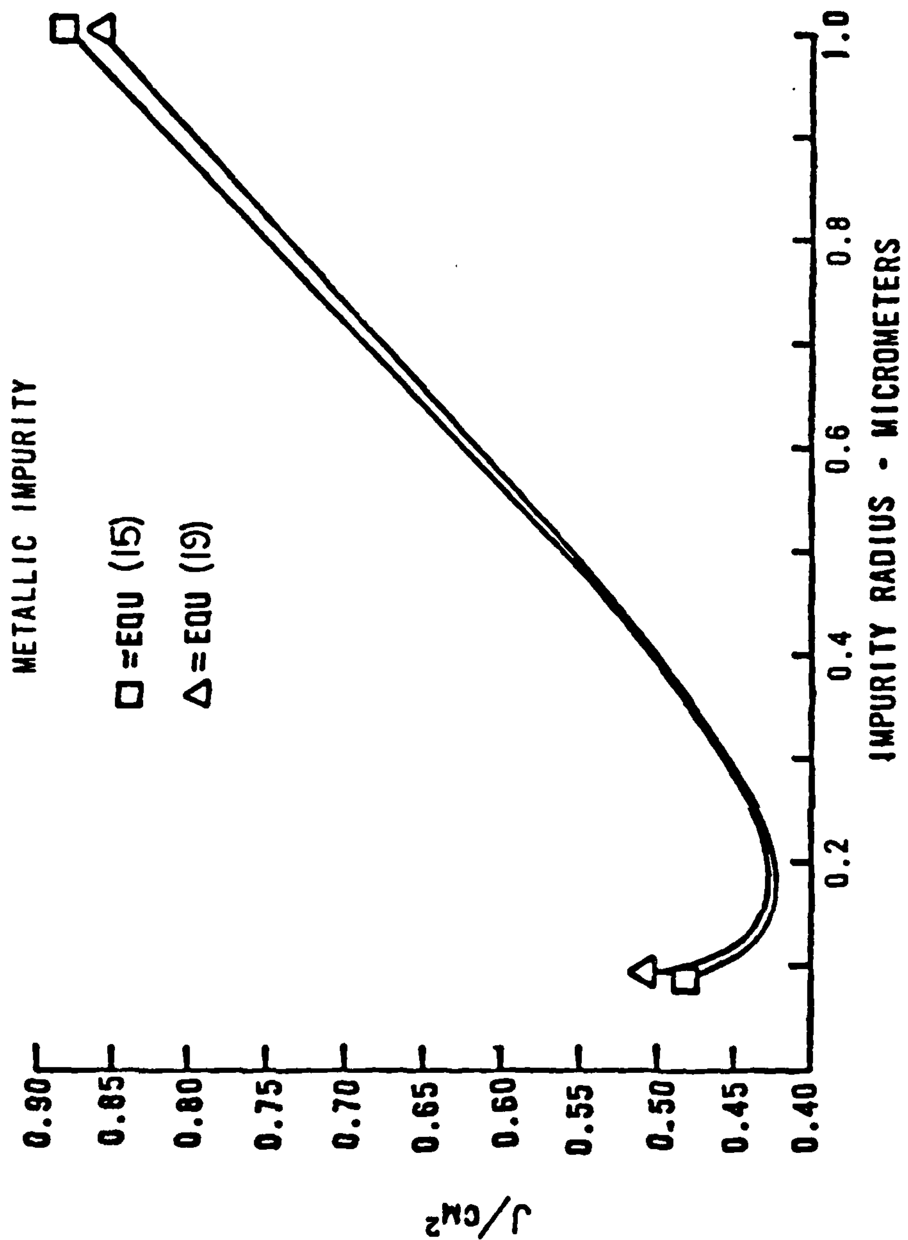

Figure 4. Exact Solution of the Thermal Equations Compared to the Approximate Solution for Metallic Impurities

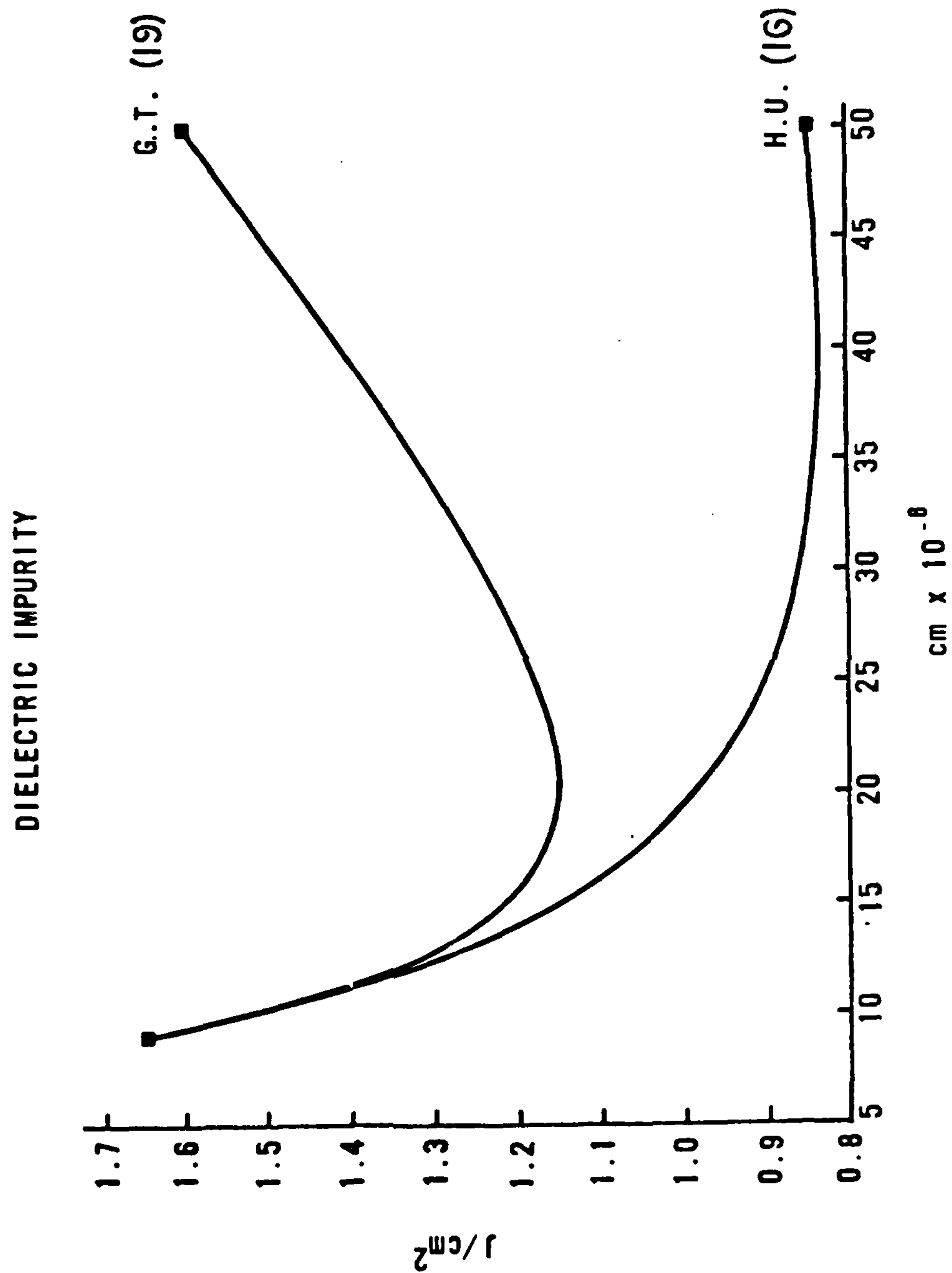

Figure 5. Exact Solution of the Thermal Equations Compared to the Approximate Solutions for Dielectric Impurities

limited by the thickness of the film and therefore, the impurity sizes are of the same order as the wavelength of light. It can also be seen from the previous figures that the size of impurity which is easiest to damage is of the same order of magnitude as the wavelengths of the laser radiation used in this research. If impurities of this size produce damage, the energy absorption is determined by the Mie absorption cross-section given by a Mie scattering calculation.

In equation (19) with a constant value of Q there is no frequency dependence. However, if we introduce an asymptotic analytic expression for the Mie absorption cross-section for Q in equation (19), this is no longer the case. Such an expression can be obtained for the Mie cross-section if the real index of refraction is between 1 and 2, and the imaginary index is much less than one. We have (81, 82)

$$Q = \pi a^2\left(1 + \frac{2e^{-\frac{8\pi n' a}{\lambda}}}{\left(\frac{8\pi n' a}{\lambda}\right)} + \frac{\left(e^{-\frac{8\pi n' a}{\lambda}} - 1\right)}{\left(\frac{8\pi n' a}{\lambda}\right)^2}\right) \qquad (20)$$

This cross-section is valid for a dielectric impurity and gives a wavelength dependence as well as an additional impurity radius dependence. The range of n and n' over which equation (20) is valid would not include metallic impurities.

The Mie absorption for metallic impurities can be approximated by

$$Q = \pi a^2\left(\frac{A\lambda}{n' a} + B\right) \qquad (21)$$

Figure (6) shows an exact and approximate equation for metallic and dielectric impurities.

An additional point must be made in connection with equation (20). Recently it has been predicted, from more sophisticated computer calculations of the Mie absorption cross-section, that resonances occur which can give rise to anomalously large absorption spikes (83, 84). Considerable discussion has been devoted to the physical meaning of the resonances (83, 85, 86). The equation (20) is a simplified analytic asymptotic approximation to the full Mie absorption cross-section. The recent computer calculations (84) give the same form as equation (20), with the exception that the resonances are superimposed.

Major points can be made in favor of retaining equation (20) in the theoretical calculations. First, the calculations are for perfect spheres. The resonances are easily destroyed by any deviation in symmetry (84). This deviation undoubtedly occurs for real impurities. Second, the predicted resonances are extremely narrow and in general for a fixed wavelength the particle radius must be exact to one part in 7000; i.e. $r = a \pm .0007$ (84). The probability of finding particles with such exact uniformity and radii would be extremely low. Finally, the resonances have never been observed experimentally, a fact that may be a result of the points discussed above. Therefore, equation (20) will be used in the theoretical calculations of this dissertation.

The greatest difficulty in applying a Mie coefficient in the theory is that the composition of the impurities is not known for most films. In addition, the imaginary index of refraction n' of the impurities is a function of frequency and as a result, comparison between experiment and theory must be relative and not absolute.

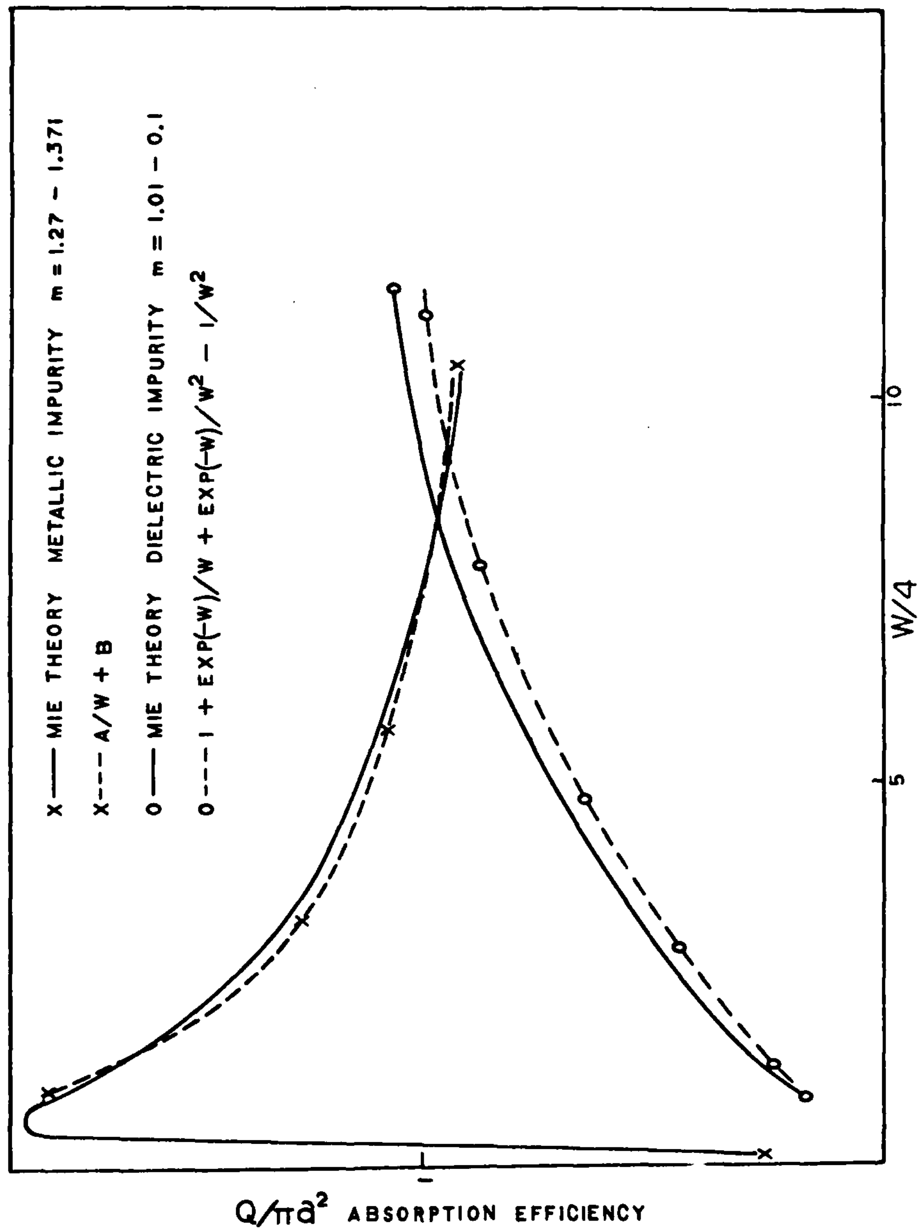

Figure 6. Mie Absorption Cross-sections for Exact Theory and Approximations ($w = 8\pi n'a/\lambda$)

That is, the impurity model can only predict trends in the breakdown field and not absolute damage thresholds.

The breakdown criterion which will be used with the Mie impurity model will be one of temperature. A fixed critical temperature is set, for example the melting temperature of the host material, and the incident energy density is plotted against the impurity size. The minimum energy per unit area required to heat an impurity to the critical temperature is taken as the damage threshold.

Calculations of impurity damage involving stresses (47), shock waves (57, 66, 71), and even avalanche ionization (55) have been carried out in an attempt to study the final stages of damage. It is assumed in this work that once the critical temperature is reached the damage proceeds catastrophically. This assumption is supported by the fact that as the temperature approaches the melting point of the host or impurity, the absorption increases dramatically (55, 57, 66, 71, 74). At this point the breakdown then develops non-linearly and rapidly. The slower process by which the critical temperature is reached determines most of the physical nature of the breakdown event. Therefore, the critical temperature criterion for breakdown should predict the relative trends in the experimental data.

The time dependence contained in equations (15), (16) and (19) is not obvious. Hopper and Ulhmann (47) have taken limiting cases of equation (15) in order to examine the time dependence of the impurity temperature. They obtained

$$T_p \simeq \left(\frac{3QIt_p}{4C_p a}\right) \qquad a >> (D_h t_p)^{1/2}$$

$$T_p \simeq \frac{QIa}{4K_h}\left(1 - \frac{a}{(\pi D_h t_p)^{1/2}}\right) \qquad a << (D_h t_p)^{1/2} \qquad (22)$$

The first equation of (22) is expected and is the constant energy per unit area result when there are no diffusion losses. The second equation gives the maximum loss case and the $a/(\Pi D_h t_p)^{1/2}$ term can be neglected. The breakdown energy per unit area is linear with the laser pulse width. Again this gives the same limiting cases as in avalanche and multiphoton ionization.

Researchers have found that in the nanosecond time regime the critical energy/area fits closely to a square root of time dependence (19). This time dependence obviously falls between the two limiting cases of equation (15). It is interesting to compare the laser pulse width dependence predicted by equation (19) with experimental data taken for bulk surfaces. Figure (7) shows how this can be accomplished. The two curves represent 5 and 15 ns damage curves as a function of particle size. It is clear that as the pulse width is decreased the threshold decreases and smaller sized particles are damaged. If a large number of these curves are plotted for different laser pulse widths, then the minimum thresholds can be plotted as a function of pulse width. The resulting graph gives the desired theor tical curve. The procedure was used to obtain the theoretical curve for fused silica that is shown in figure (8). The data was taken from Milam, et al. (19) and is for fused silica surfaces. The agreement between the theory and the data is excellent. Milam (19) made a best fit to a $(t_p)^{1/2}$ curve and found a good fit to the data. However, the $(t_p)^{1/2}$ fit is not as good in a least squares sense as that shown in Figure (3).

The wavelength dependence of the breakdown threshold is contained in the Mie absorption coefficient. It can be seen from Figure (6) that as the wavelength decreases or n' increases, the cross-section for oxide

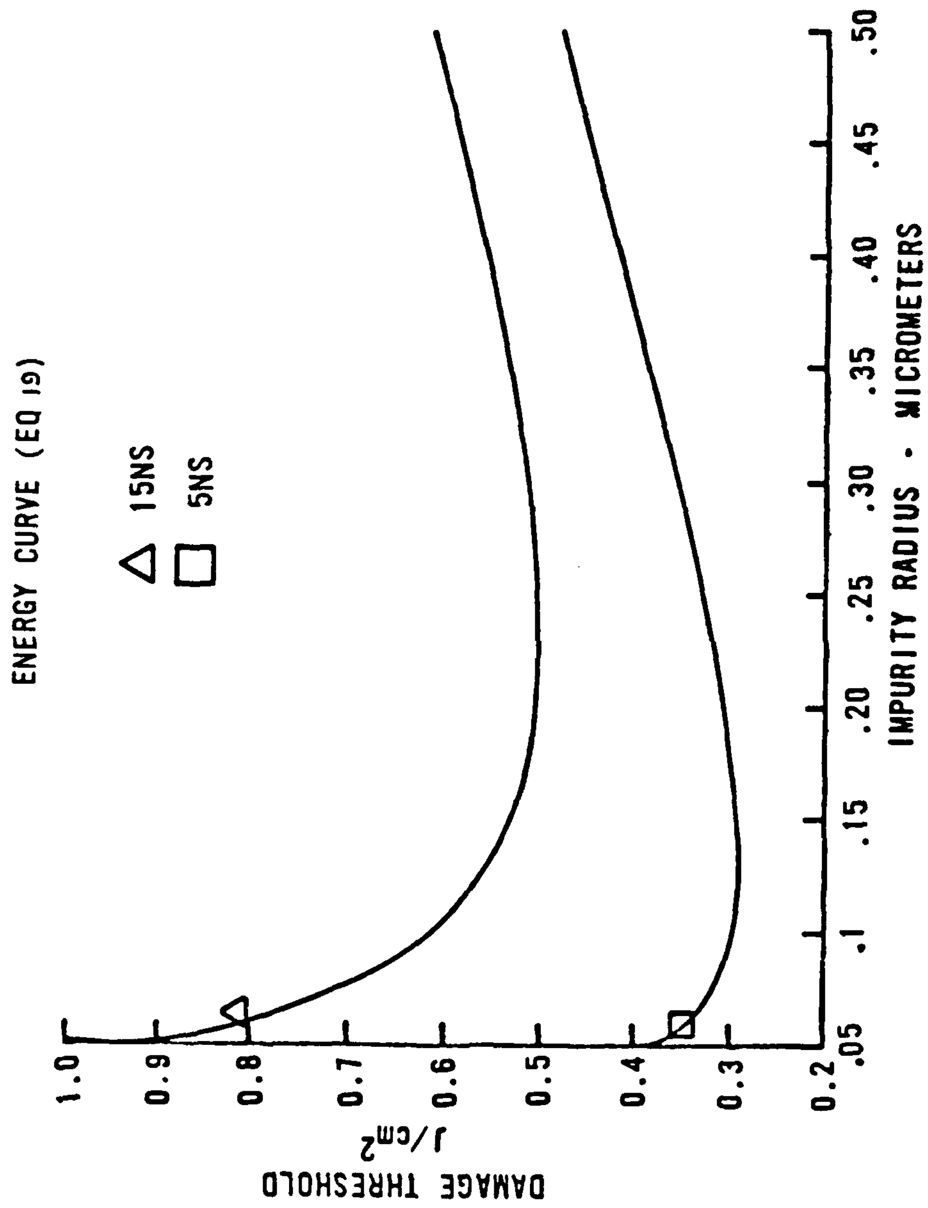

Figure 7. Damage Threshold vs. Impurity Size at 5 and 15 Nanoseconds

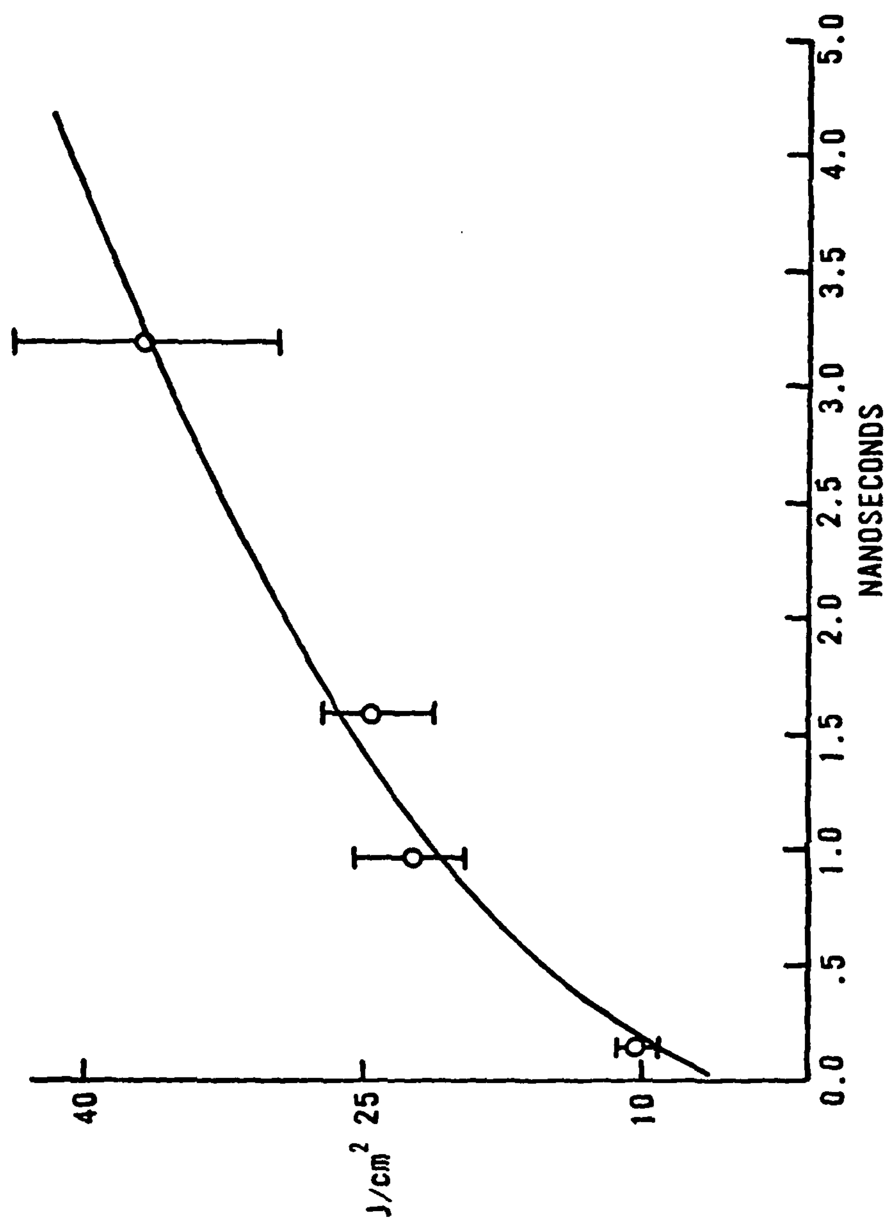

Figure 8. Damage Threshold vs. Laser Pulse Length for Fused Silica

impurities increase and the threshold goes down. However, equation (21) for metallic impurities is somewhat misleading. The cross-section would decrease with decreasing wavelength if n were a constant. This is not the case because n decreases with a decrease in wavelength (87) and the cross-section actually increases. Thus, we expect the breakdown threshold to decrease at shorter wavelengths for both oxide and metallic impurities.

Table I summarizes the results of this section. We note that the avalanche ionization equations (3) and (6) predicts a very strong laser pulse length dependence, almost linear with the laser pulse length. The multiphoton ionization predicts a strong pulse length dependence at long wavelengths. For example from equation (11), for dielectric films at 1.06μm the pulse dependence is $\sim t_p^{.88}$. At 0.26μm the dependence is $\sim (t_p)^{1/2}$. The predicted pulse dependence from the impurity model fits closely to a $t_p^{1/2}$ curve.

MODEL \ PARAMETER	PULSE LENGTH	WAVELENGTH
AVALANCHE	$\approx \frac{t_p}{LN\, t_p}$	$\lambda \downarrow$ E_c CONST. OR $\lambda \downarrow$ $E_c \uparrow$
MULTIPHOTON	$\approx t_p^{.88}$ AT 1.06 μm $\approx t_p^{1/2}$ AT 0.26 μm	$\lambda \downarrow$ $E_c \downarrow$
IMPURITY	$\approx t_p^{1/2}$	$\lambda \downarrow$ $E_c \downarrow$

Table 1. Theoretical Predictions of Damage Threshold With Laser Wavelength and Pulse Length

III. EXPERIMENT

Experimental Arrangement

The results presented in the theoretical section point out that a single parameter study of damage does not provide adequate data to select among the competing damage mechanisms. The experiment in this research was designed to study the damage process as a function of laser pulse length and wavelength. The dielectric coatings that were tested were selected to provide a wide range of material parameters such as bandgaps, thermal properties and refractive index. Additionally, different film thickness were tested to provide data on the effects of different standing field patterns in the dielectrics.

The experimental arrangement is shown in Figure (9). The experiment was designed to divide the beam into three separate paths. Path A contains more than 99.9% of the energy after it is reflected by the dichroic beamsplitter [1]. This is the high energy path and is used to irradiate the thin film samples placed at [3]. Path B which contains less than 0.1% of the energy was used to measure the spatial profile of the beam. Path C contains less tham 0.01% of the energy and was used to measure the temporal profile of the laser pulse.

The dichroic beamsplitters shown [1] and [2] in Figure (9) were specially designed to reflect one of the harmonics of 1.06μm and transmit any others. Thus, there was a set of beamsplitters designed to reflect either 1.06, 0.53, 0.35, or 0.26μm radiation and transmit the others. They served the necessary function of filtering any of the unwanted harmonics from path A and B in the experiment.

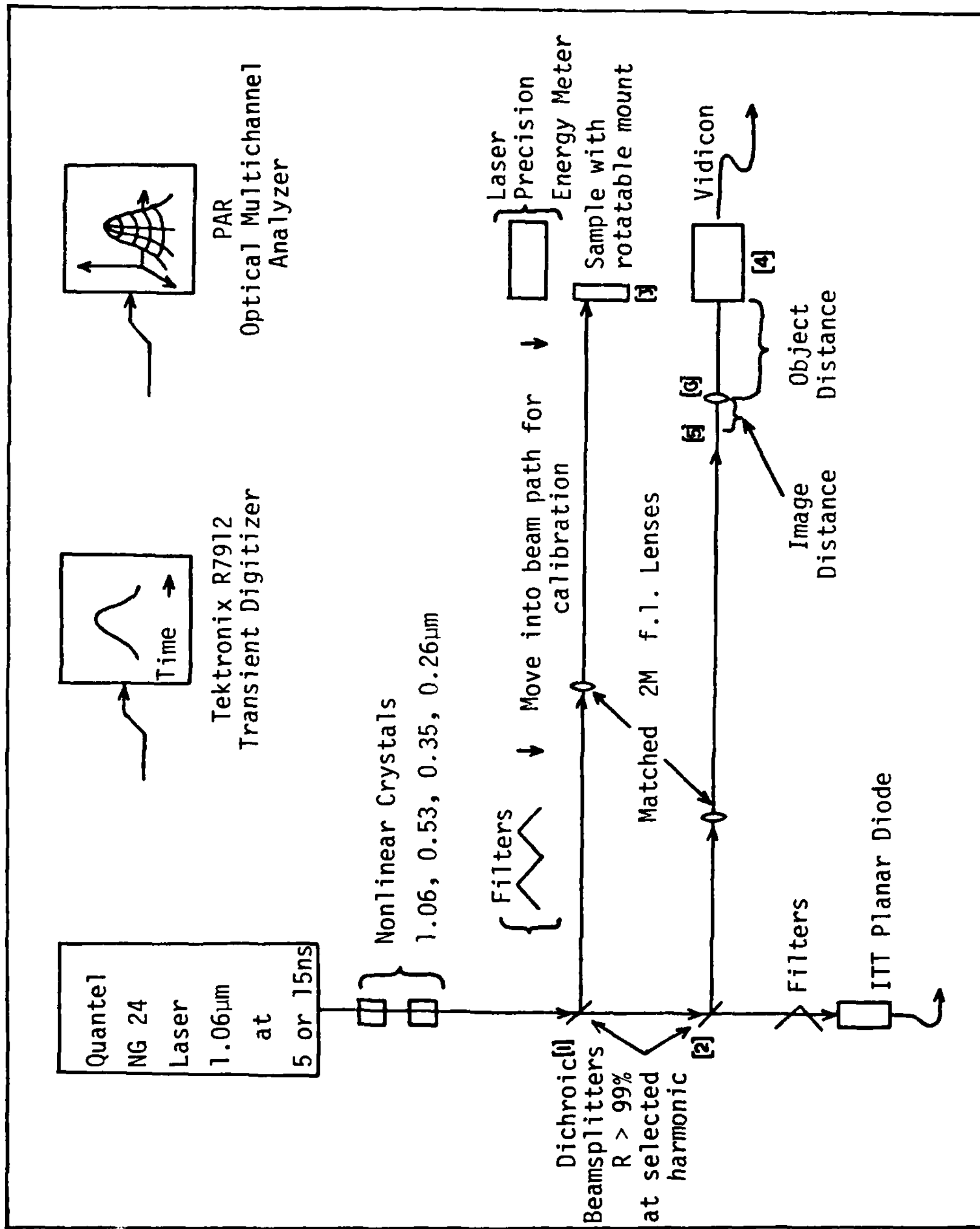

Figure 9. Experimental Arrangement

The beamsplitter at [1] also acted as an attenuator and reduced the number of filters needed in front of the detector at [4] . This minimized the amount of spatial distortion introduced by filters.

It was crucial to the experiment that the beam profiles in paths A and B be identical to each other, since the final goal was to characterize the beam at the sample site [3] by using the low energy path B. Several precautions were taken to insure that the two beams were identical in spatial profile. First, the beamsplitters were flat to $\lambda/20$ at 0.63μm wavelength. Second, the lenses at L_1 and L_2 were selected to have as nearly the same focal lengths and spherical abberations as possible. Third, the lenses were placed at identical distances from the laser. This was necessary because the laser beam was slightly converging as it exited the laser. Positioning the lenses at exact distances insured that the laser spot sizes were the same onto both lenses.

It was necessary to vary the total energy from the laser during the experiment to determine the damage thresholds of the samples. The usual procedures of changing the energy in the high energy path is to place calibrated attenuators in the path (88-91). The effects of this technique on the beam spatial profile were tested in the following manner. Both paths A and B were adjusted to fall onto the detector array at [4] . This detector will be described in detail later. An additional beamsplitter was placed in path A so that the energy in both paths were comparable and the spatial profiles of the two beams could be observed simultaneously. The point by point variation of the two beams varied by no more than $\pm 7\%$. That is, equivalent points in the profiles had the same relative magnitude with respect to any other equivalent points within the two profiles. As will be discussed

later most of this variation can be associated with the non-uniformity of the detector response across the active elements and not spatial profile variations between the two beams. It was found that when attenuators were placed in Path A substantial beam distortion was produced. The distortion was so large that equivalent points could not be identified between the two profiles. The attenuators might have been placed in the beam before the beamsplitters 1 and 2 which would have produced the same distortions in both paths. However, the distortions appeared in some cases as small spikes on the profile and this might have influenced the damage results during the experiment. In order to obtain as smooth a profile as possible, the attenuators were not used. Actual control of the energy, which will be described later, was finally accomplished by adjusting the voltage settings for the flash lamps in the laser.

Experimental Components

It has already been stated that the most crucial requirement of a laser damage experiment is to characterize the laser beam in both time and space at the damage site. The temporal behavior of the pulse was recorded with fast planar diode detectors. An ITT F112 detector was used to record the time profiles of 1.06 and 0.53μm laser pulses; at 0.35 and 0.26μm an ITT F4000 detector was used. The rise time of these detectors was controlled by applying a bias voltage and was set to less than 0.5 nanoseconds (ns). The output signal of the detectors was then processed by a Tektronix R7912 Transient Digitizer, which is a high-speed signal acquisition instrument that digitizes the input analog signal. The operation of the R7912 is similar to an oscilliscope in that an electron

beam is scanned horizontally and deflected by the input signal. The target of the electron beam is, however, an array of diodes which record the vertical and horizontal position of the beam. The digitized signal is then displayed at a slower speed on a video monitor and transferred to a PDP-11 computer, which was programmed to calculate the full width at half maximum (FWHM) of the laser pulse. Figure (10) shows the computer output for a 6 and 16 ns laser pulse.

The spatial characterization of the beam was obtained with a Princeton Applied Research optical multichannel analyzer (OMA). The OMA is a vidicon system which utilizes an electronic camera and a microprocessor. The vidicon contains a 12.5 x 12.5 mm active area composed of small diodes which are given a surface charge by an electron beam. When light is incident on the diodes, the photons create electron-hole pairs which deplete the surface charge. The amount of depletion is therefore, a direct measure of the number of photons incident on the diodes. The electron beam then recharges the diodes and the required current is measured. This current is then directly proportional to the laser energy incident on the diodes.

The electron beam diameter at the active surface or target is 25μm and covers approximately nine diodes at the surface. Each data point is then the sum of the contributions from all nine diodes. It is also apparent that the minimum resolution of the vidicon is 25μm x 25μm, as determined by the diameter of the electron beam.

The purpose of the electronic camera and the microprocessor is to scan the electron beam across the detector surface in any desired pattern and to store the data in a usable format. During the

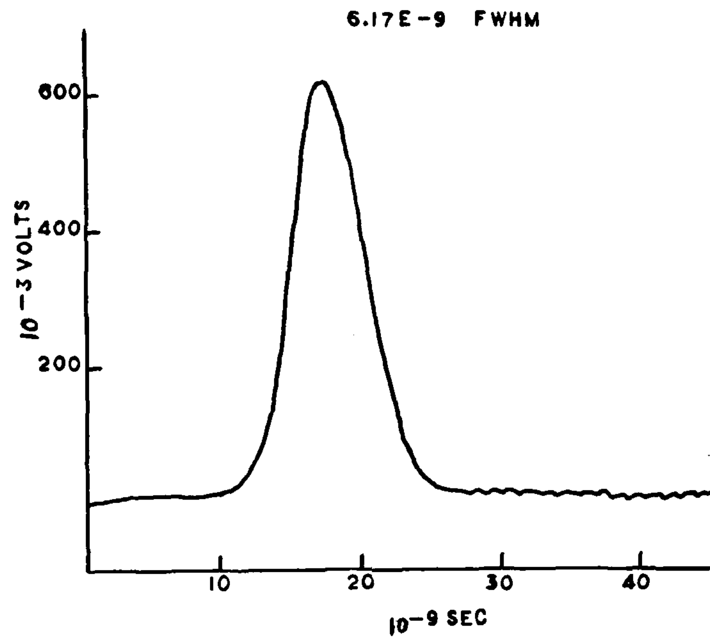

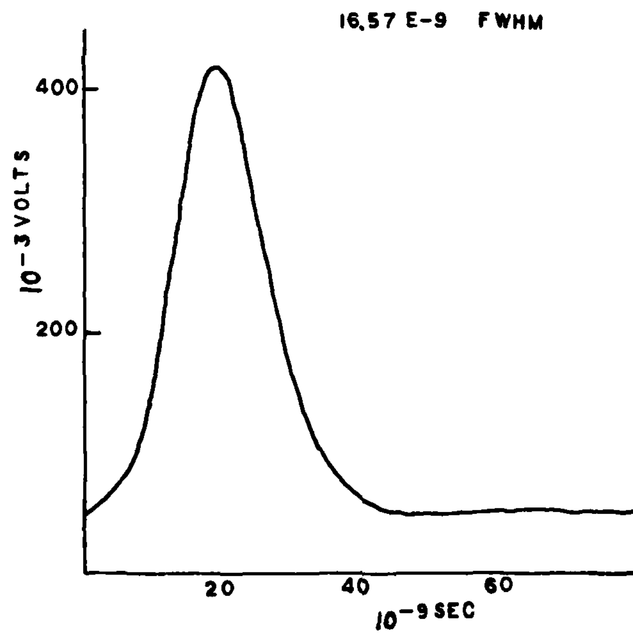

Figure 10. Laser Profile in Time

experiment the vidicon target was scanned by the electron beam in horizontal paths or tracks, as shown in Figure (11). Each track contained a maximum of 250 data points across the active surface area and a total of forty tracks could be programmed into the OMA.

Although the maximum resolution of the vidicon was 25μm x 25μm, in practice it was not used. The laser spot size on the thin film sample was as small as 170μm and, only about seven data points would have spanned the laser profile. To obtain a better resolution the beam spot was magnified and reimaged on the vidicon. With sufficient magnification, the output of all the photo-diodes in an area of 4 x 4 electron beam diameters could be integrated together while still improving the effective profile resolution. Another advantage of this approach was that the background noise of the vidicon was signicantly reduced and the dynamic range was increased. During the experiment each data point represented a physical area of 100μm x 100μm.

The following technique was used to magnify and reimage the laser spot in the diagnostic Path B. Location [5] (see Figure (9)) is the equivalent focal plane in Path B to that in Path A at the thin film sample, [3] . The object distance is between the focal plane and the lens at [6] and the image distance is between the lens [6] and the vidicon [4] . The lens 6 had a focal length of 10mm and the object distance was set to produce a magnification of about 12. Exact determination of the magnification was made by placing a thin wire (98.4μm) in the beam path at [5] . Using a special holding and positioning apparatus, built to allow fine control of the wire position, the laser was fired and the wire shadow was viewed by the vidicon. The vidicon was mounted on two Aerotech mounts which provided position control. The image distance was adjusted by moving one Aerotech

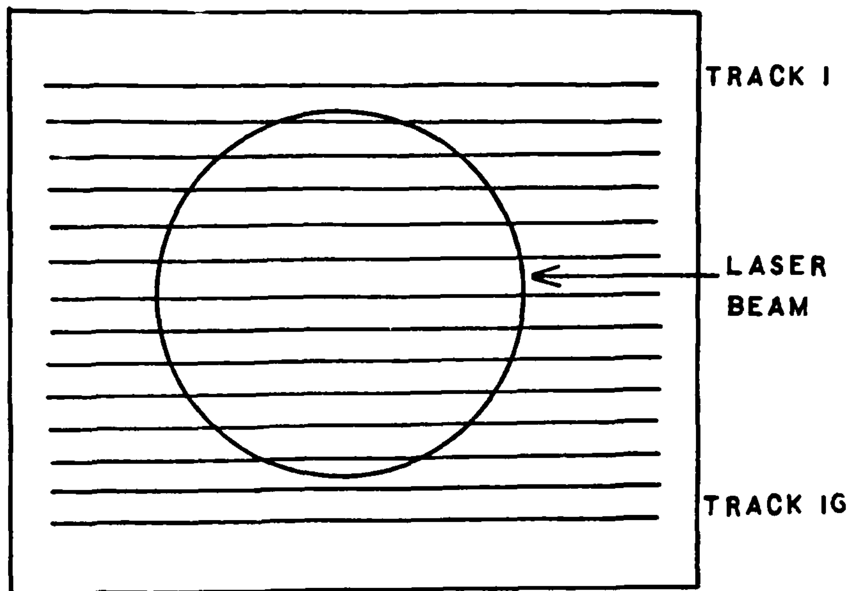

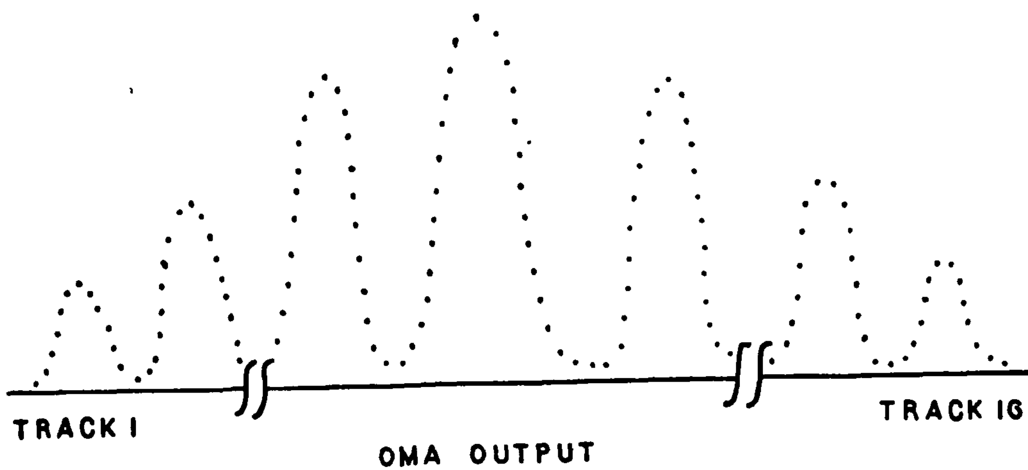

Figure 11. Vidicon Scan Pattern and Output

mount until the wire shadow was as sharp as possible, and the number of data points across the edge of the shadow was minimized. This was easily done by shifting the vidicon along the optical axis while recording the output. The span of the reimaged wire shadow was determined by the number of data points across the shadow. Since each data point represented a 100μm physical width the image size was obtained directly, although it was necessary to go through a calibration procedure of the vidicon to insure that the electron beam was focused to its minimum 25μm diameter. The magnification factor was obtained by dividing the image size of the wire shadow by the measured wire size. An effective resolution of the vidicon of 8.5μm was obtained by dividing the 100μmm vidicon element size by the measured magnification.

The next step was to calibrate the output response of the vidicon. First, the uniformity of the vidicon response was measured across the active surface area by using a Helium-Neon (He-Ne) laser operating in the TEM_{00} mode. The beam was expanded, collimated and directed onto a pinhole. The Airy pattern formed by the pinhole then fell onto the vidicon. The distance between the pinhole and the vidicon was predetermined by calculation so that the total variation in laser intensity across the vidicon was less than 1%. The output of the vidicon across the target area was then recorded, which showed a maximum variation of $\pm 7\%$. It should be pointed out that two different detectors were used in the experiment. A PAR 1252 was used at 1.06 and 0.53μm and a PAR 1254E used at 0.53, 0.35, and 0.26μm. The overlap in wavelength at 0.53μm between the two detectors

provided a cross calibration of the two. Both detectors exhibited the same ±7% in response uniformity.

An absolute calibration of the vidicon output was obtained by placing an energy meter at the location of the thin film sample. This is shown in Figure (9). The energy meter was a Laser Precision Rk-3200 readout unit and a RkP-331 probe. The spectral response was flat to within ±4% from 0.26 to 1.06μm. The detector was apertured to the same diameter as the lens at [6] to eliminate energy in the wings of the beam that would not be seen by the vidicon. The laser was fired with the oscillator cavity spoiled so that it did not lase and a background reading was taken from the energy meter. At the same time the vidicon response was recorded and stored on a floppy disc. The laser was then fired with the cavity unspoiled; then the energy reading was recorded and the stored background subtracted. Each data point obtained from the vidicon was given in terms of counts, which represent the amount of electron beam current required to replenish the surface charge of the photodiodes. Within the linear range of the vidicon the counts are directly proportional to the energy. To obtain the vidicon calibration all of the counts in the spatial profile were integrated together and then divided into the energy reading to obtain the energy per count. To find the peak energy/area, it was necessary to scan the spatial profile, find the maximum data point, then convert counts to energy and divide by the effective area of the data point. For a single calibration a total of ten shots were taken and the results averaged. The maximum variation from the average of a single calibration shot was always less than ±5%. During all test sequences the

calibration was conducted before, during, and after the sequence to insure that the calibration did not change.

A test was previously described in which the beam profiles in Paths A and B were compared. A second test was employed during the experiment. It was found that at 0.26μm the damage morphology of Hafium Oxide (HfO_2) films showed a uniform removal of the thin film materials from the substrate. This is in contrast to the isolated circular pits observed at longer wavelengths. This uniform removal appeared to reproduce the beam profile contour quite closely. Noting this, the laser beam was purposefully distorted in the near field to produce random "hot spots" of energy in the far field. The HfO_2 samples were subjected to damaging pulses, the damage sites were photographed and the complete intensity profiles were recorded with the OMA in the diagnostic Path B. The comparison of an actual damage site with the vidicon output is shown in Figure (12). The lines of constant energy per unit area are drawn on the vidicon output and the photograph was taken with a Nomarski microscope. It is clear that the distributions are essentially the same and that areas of high material removal correspond to areas of high energy deposition. This served as one of the checks employed to insure that the planes at [4] and [5] (Figure 9) were equivalent.

This is the first damage threshold experiment in which the vidicon technique was used to obtain the laser spatial profiles. A similar vidicon system was designed and built by Smith, et al. (92) and compared with the usual photographic film techniques used to obtain spatial profiles. As yet this system has not been used in damage experiments.

Figure 12. Comparison of Vidicon Output and Damage Morphology in HfO_2

The vidicon allows the first real time damage experiments which have the same degree of accuracy as experiments using the much slower photographic film techniques. In fact, the very large amount of data taken in this dissertation would not have been possible without the vidicon beam profiling technique.

The laser system, which was built by Quantel Corp., has a Nd-YAG oscillator and preamplifier, and is shown in Figure (13). A Nd^{3+} doped silicated glass rod is used as the main amplifier of the system, and produces a maximum output energy of two joules in a 20 nanosecond pulse. The beam as it exits the main amplifier is diverging and a long focal length lens 19 is used to make the beam slightly converging. The laser was passively Q-switched with a saturable dye (BDN) placed in the oscillator cavity at [2] . The pulse length of the laser was controlled by the dye concentration and the cavity length of the oscillator. The output mirrors at M1 and M3 could be rotated into and out of the beam path to obtain the variation in the cavity length. With M1 in and M3 out, a shorter cavity is produced and with the proper dye concentration a 5ns pulse is obtained. Some variation in pulse length could be obtained by varying the dye concentration, however, the most stable operation occured with the 5ns pulse. The longer cavity was designed for 20ns pulses, but it was found that using a dye concentration which produced 15-18ns pulses gave the most stable and reproducible output.

The nonlinear crystals were placed at [20] and [21] . The second harmonic of 1.06μm was produced by frequency doubling using a KDP crystal at [20] . The third harmonic at 0.35μm was produced by sum frequency generation with a second crystal at [21] . This crystal

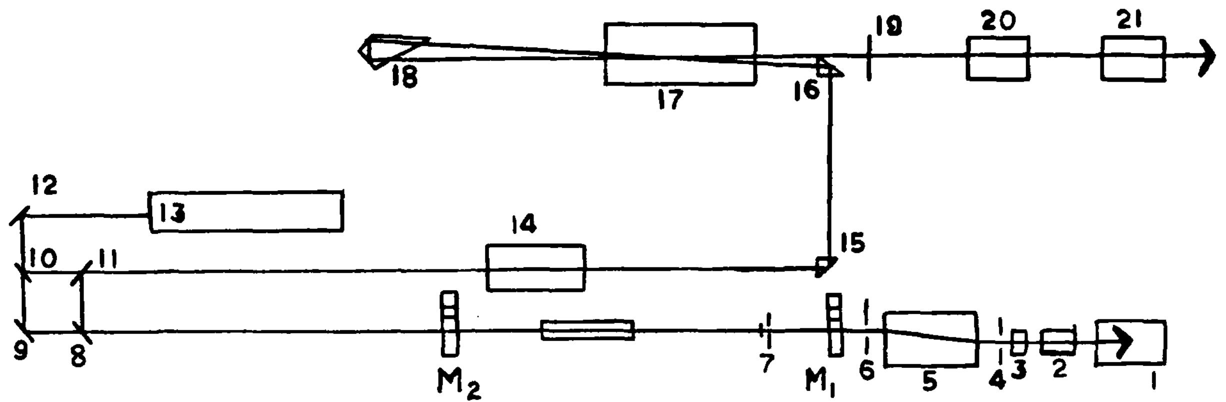

1) MS 390 with 5 mm RC mirror (R M 1.06 μ)
2) CL06 Pockels cell
3) Polarizer
4) D_2 Diaphragm
5) HH 305 laser head
6) D_1 Diaphragm
7) Beam shutter
8) Corner mirror for 1.06 μ
9) Silver mirror for the HeNe
10) Silver mirror for the HeNe
11) Corner mirror for the 1.06 μ
12) Silver mirror for the HeNe
13) HeNe laser
14) HH 305 laser head
15) AR coated 90° prism
16) AR coated 90° prism
17) SF 320-16 laser head
18) Double pass prism
19) Lens
20) FD 312 Harmonic generator
21) FT 312 for FQ 312 Harmonic generator

Figure 13. Detail of Laser System

combined the fundamental (1.06μm) and the second harmonic (0.53μm) to produce w + 2w = 3w (0.35μm). The fourth harmonic at 0.26μm was obtained by frequency doubling the second harmonic. The crystals were angle turned for index matching and were temperature stabilized.

It was found that beam quality in the far field was steadily degraded from the near gaussian profile at 1.06μm as one progressed to 0.26μm. This degradation is a normal occurence and is due to the nonlinear response of the crystals to structure in the 1.06μm near field pattern. There was also shot to shot jitter in the position of the laser spot at the target site. This was measured to be as much as 100μm and was caused by thermal gradients and vibrations within the laser system. The positional jitter was accentuated by the long optical path of the laser to the target site (∿4M). The combined beam degradation and jitter rendered some previously used beam spatial diagnostic techniques unsuitable. For example a pinhole arrangement used extensively by Newnam (19, 21, 30) and Solieu (14, 15, 75) requires a stable output and a gaussian profile. The pinhole is placed at the equivalent focal plane in the diagnostic path and positioned so that the peak of the beam spatial profile falls on the pinhole. The diameter of the pinhole is picked so that the variation in energy over the hole diameter is less than 5%. The measured energy through the pinhole is ratioed with a total energy measurement on each shot to insure that there is no beam jitter on the pinhole. With the laser system employed in this experiment this technique could not be used and the OMA system was the only approach which could be used to obtain the large amount of data needed.

There were several important experimental factors associated with

the laser that need to be considered when interpreting the final data. The first is the variation of the laser pulse width as the frequency is changed. Again, due to the non-linear response of the crystals, the pulse width decreases as the fundamental frequency is doubled, tripled and quadrupled. Under the conditions of the experiment the short pulse widths (FWHM) at 1.06; 0.53; 0.35; 0.26μm were 5±.25; 4.5±.22; 4.1±.22; 4.1±.2; 3.7±.18ns and the long pulse widths 15.5±.8; 13.5±.7; 12.5±.6; 11±.5ns. Since only two different pulse lengths were used at each laser wavelength there was no practical way to correct the data for the pulse width variation.

The second factor was the change in laser spot size with frequency. Because of space limitations within the laboratory, the longest focal length lens that could be used in the experiment was two meters. A one meter focal length fl lens was used at 1.06μm which produced a 360μm (FWHM) spotsize at the thin film sample. No difference in the breakdown threshold was found when a two meter fl lens was used at 1.06μm, which produced a spot size of 360μm at 0.53μm. At 0.35μm the spot size was 250μm and at 0.26μm it was 170μm. The spot sizes given here are all FWHM points and represent an average at each wavelength. In general, the beam was not gaussian and the spot uniformity would vary with alignment drift in the non-linear crystals. Also the profiles were not symmetrical. The spot sizes given here are essentially the minimum dimension recorded at each wavelength. The maximum values were about 15% larger than the quoted sizes.

A standard technique that has been used to keep the spot size the same at each frequency is to move the sample closer to the lens at the shorter wavelengths (13, 93). This means that the target sample is no

longer in the far field. The beam profile was examined with the OMA away from the focal plane of the focusing lens in path B. It was found that at only a few centimeters from the focal plane that the beam had so much structure the technique was not usable, a conclusion supported by the work of Morgan, et al. (94). Thus, in the experiment it was not possible to hold the spot size constant as the frequency was changed. This will be discussed in more detail in Section IV.

The thin film target samples were mounted into a holder designed by Bettis (95) and House (96). The holder allowed the samples to be rotated around an axis parallel to the beam axis. In this way new sites on the target could be rotated into the beam path. The holder also had three axis translational control so that the sample could be initially positioned and once a row was completely filled by laser shots, could be moved to start a new row. The shot pattern created on the sample is shown in Figure (14). Each laser shot site is 1.5mm from the next site in the same row. The holder was rotated a set number of degrees to obtain this spacing. Each row is 1.5mm from the next row.

For this experiment a duplicate holder was made for the Nomarski microscope, which allowed the sample to be removed from the experiment and examined under the microscope for damage.

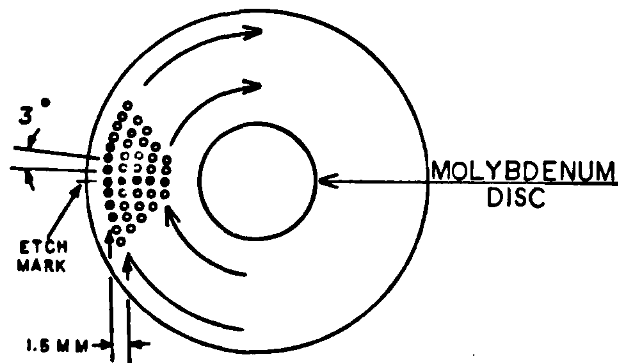

Figure 14. Laser Shot Pattern on the Sample

Optical Alignment

The optical alignment of the system was important, particularly the lens at [6] in Figure (9). First the beamsplitters at [1] and [2] were positioned so that the beam was incident on the centers. The two paths A and B were adjusted to be parallel. The vidicon and the sample holder were placed in their respective paths and centered on the beams. Next the focusing lenses at [1] and [2] were positioned into the beam paths so that the beams were still centered on the vidicon and holder. The lens at [6] was moved into the beam path and adjusted until the beam was again centered on the vidicon. This could be done easily by watching the vidicon output while adjusting the lens position. To complete the alignment in Path B, the wire which was used to calibrate the magnification was moved into position at [5] . The exact position was again adjusted by watching the position of the shadow in the vidicon output. Last, the vidicon position was adjusted until the shadow edges were the most narrow.

The sample was then placed into the holder and adjusted until the reflected beam made a 3° angle with the incident beam. This angle prevented the reflected beam from feeding back into the laser system. Each sample was etched with a file on the edge to serve as a reference mark. The sample was then positioned so that the beam was incident onto the etch mark and the first row of shots was begun by moving the sample 4mm with respect to the laser beam. After the first row was completed the beam was realigned on the etch mark and moved perpendicular to the beam 5.5mm, and another circular row of sites were tested. With this technique a total of 250 sites could be tested on each sample.

Sample Preparation

The thin film materials used in the experiment were Thorium Floride (ThF_4), Calcium Fluoride (CaF_2), Magnesium Fluoride (MgF_2), Silicon Dioxide (SiO_2), Hafium Oxide (HfO_2), Titanium Oxide (TiO_2), Aluminum Oxide (Al_2O_3), Zirconium Oxide (ZrO_2), and Magnesium Oxide (MgO_2). These films were chosen based on their use as dielectric coatings in the visible range and because their ultraviolet (UV) cutoff permitted an evaluation of multiphoton effects. Each film was deposited in five different thicknesses which at 1.06μm were 1λ, 1/2λ, 1/4λ, 1/6λ, and 1/8λ, to within a 10% degree of accuracy. If the optical thickness of the film at the wavelength of interest is an integral multiple of λ/2 the absorptance is

$$a = (Tu + Ru) - (Tc + Rc)$$

where Tu and Ru are the transmittance and reflectance of the uncoated samples and Tc and Rc are the same quantities obtained after coating. Although this is neither the most sensitive nor accurate technique for measuring the thin film absorptance it does provide a valuable indication of the amount of absorptance in the thin films. Typical process parameter and measurements for MgF_2 are shown in Figure (15) and Table (2).

Damage Threshold Determination

It is extremely desirable to have a method of determining whether or not damage occurs in the sample after each laser shot without having to remove the sample and place it under the microscope. In the past there have been several techniques developed to determine damage at the time of the laser shot. One is to monitor the damaging pulse after it has exited the target sample. When breakdown occurs the latter part of the

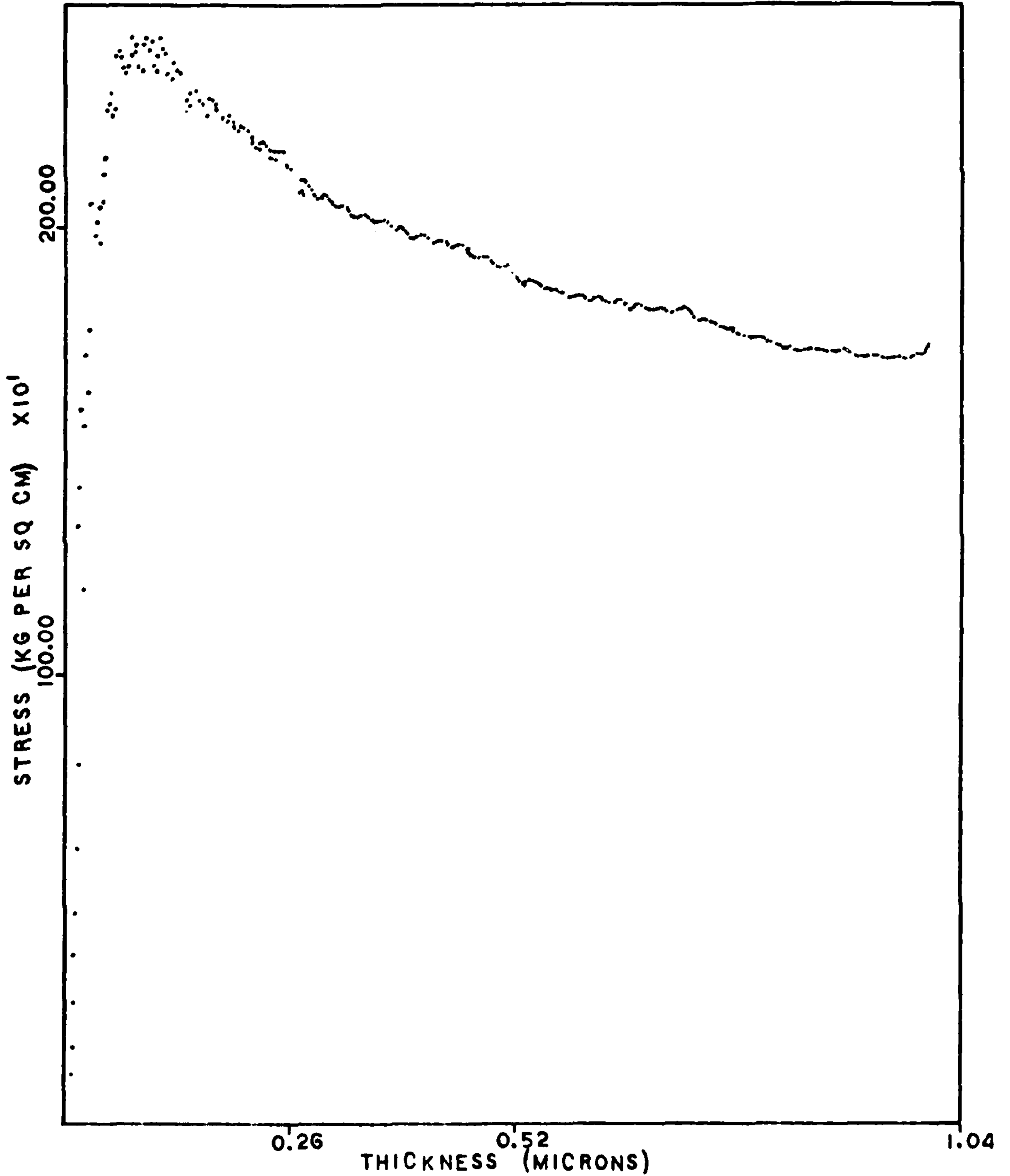

Figure 15. Residual Stress vs. Film Thickness in MgF_2

MgF_2 Deposition Analysis

Substrate temperature = 250°C

Ultimate pressure = 8×10^{-7}

Deposition pressure = 2×10^{-6} torr

No O_2 bleed

Sample Number	Film Optical Thickness	Uncoated Surface Roughness (FECO) (A)	Percent T.I.S. @ 6328 μm Uncoated	Percent T.I.S. @ 6328 μm Coated
1100		9	0.035	0.35
1101	1.102λ @ 1.06 μm	9	0.34	0.36
1202		9	0.36	0.17
1203	0.572λ @1.06 μm	9	0.32	0.28
1404	0.558λ @ 0.530 μm	9	0.32	0.040
1405		9	0.036	0.042
1606	0.537λ @ 0.353 μm	9	0.36	0.020
1607		9	0.038	0.034
1808		9	0.036	0.036
1809	0.419λ @ 0.265 μm	9	0.034	0.030

Refractive Index Data

λ_1 (μm)	$n(\lambda_1)$
1.539	1.339
0.946	1.351
0.668	1.390
0.519	1.387
0.425	1.392
0.361	1.385
0.315	1.427
0.279	1.426
0.251	1.432

Absorptance Data

λ_2 (μm)	$a(\lambda_2)$
1.167	0.0015
0.789	0.0058
0.585	0.0055
0.469	0.0067
0.393	0.0076
0.337	0.024
0.297	0.033
0.265	0.036

Table 2. Analysis of MgF_2 Thin Film Coatings

damaging pulse is truncated. Figure (16) shows the non-deformed shape from a damaging pulse and the truncated pulse obtained through the damaged site. It was found in this experiment that when damage occurred and the beam was truncated that heavy damage was the result. That is, small damage could be found under the microscope even when the beam was not truncated. The truncation of the beam is associated with the formation of a plasma sufficient to block the beam from the detector. This observation has been cited as support for the theory of avalanche ionization (11) and for an impurity initiated avalanche model (75). The definition of heavy damage, used here, refers to the creation of ten or more isolated pits or craters within the thin film. The energy level for heavy damage was substantially higher than for single site damage.

A seond method shown in Figure (17) was developed in this effort and utilized the non-specularly reflected light from the sample target site. A complete description of the method was detailed in a previous publication (97). When damage occurred, an increase in the scattered light was produced. This technique proved to be the most sensitive for monitoring damage, and a single damage site of less than 1μm in diameter could be detected. However, since the amount of scattered light is proportional to the ratio of the laser spot size to the damage site size, the spot size of the laser could be no larger than 100μm in order to detect 1μm damage sites. This spot size was smaller than desired for the experiment in order to exclude any spot size dependence, and the technique was not used to determine damage events. In spite of this, useful data was obtained with this technique, and a typical damage sequence is shown in Figure (18). The laser was fired at a low energy

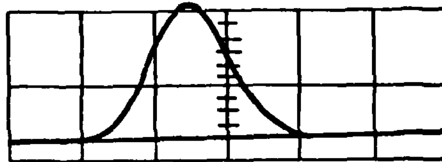

A. NO DAMAGE TO SAMPLE

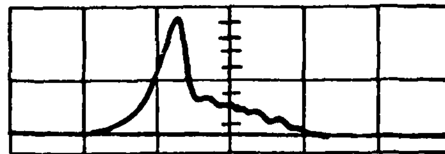

B. DAMAGE TO SAMPLE PULSE IS TRUNCATED.

Figure 16. Laser Pulse Truncation
Due to Damage

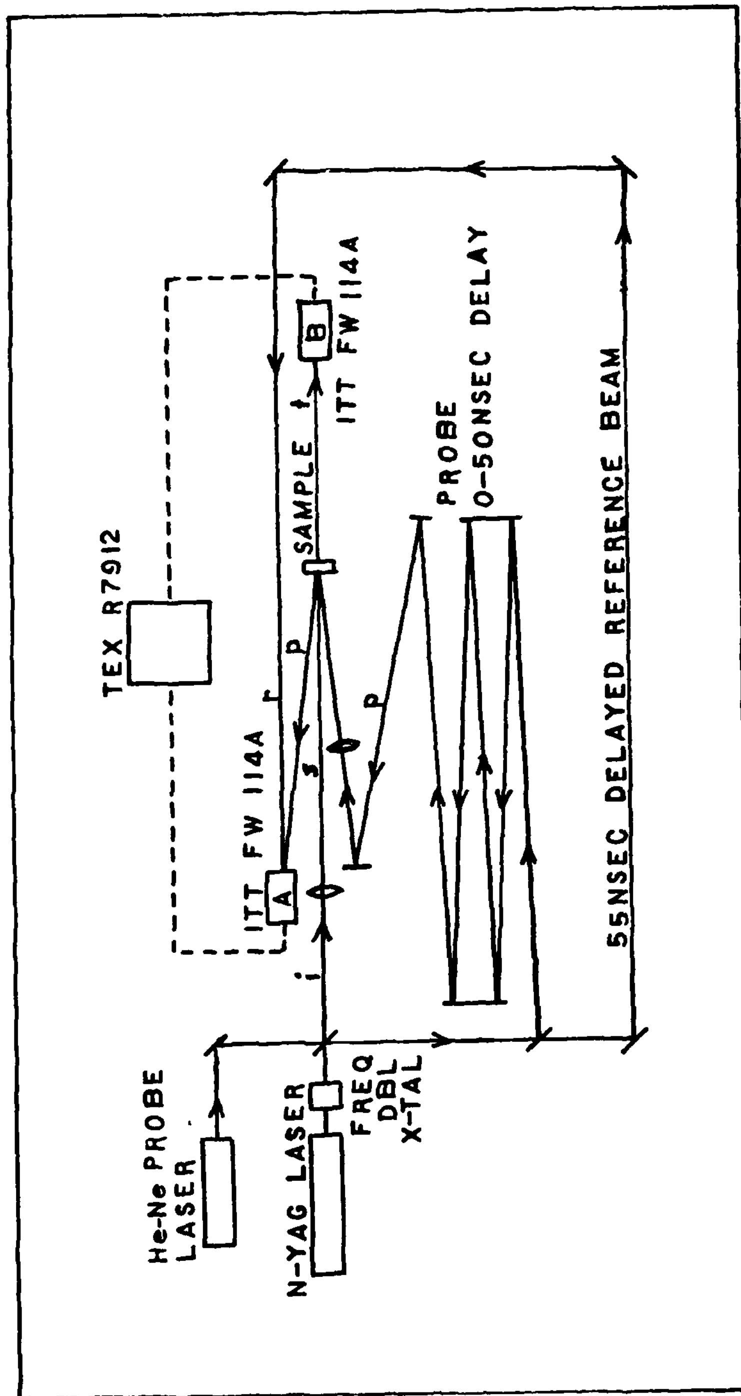

Figure 17. Experimental Arrangement for Detecting Scattered Laser Light

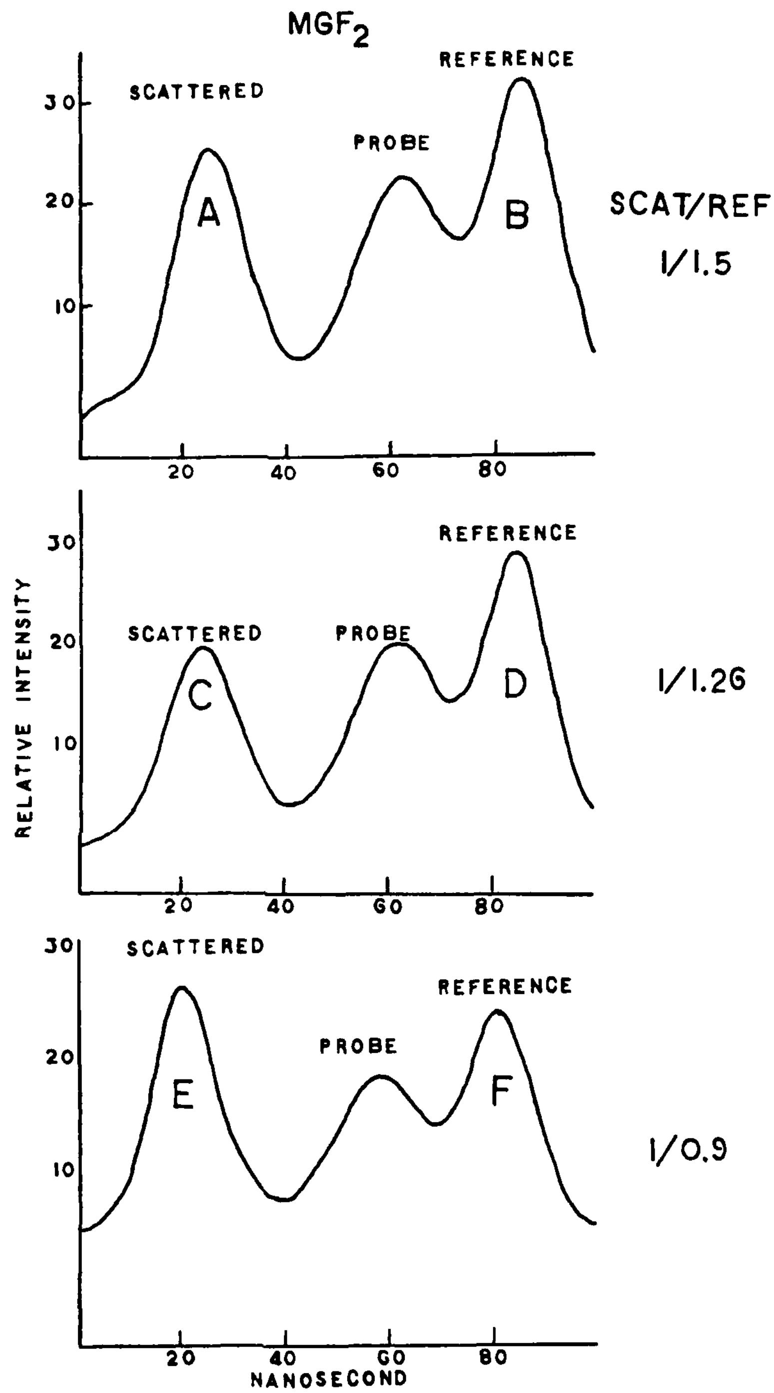

Figure 18. Change in Scattered Light Due to Damage

level and the scattered light (pulse A) was measured as well as a reference pulse (pulse B). The ratio of the scattered pulse to the reference pulse was used to measure any change in the quantity of scattered light. A damaging shot is shown in the second picture of Figure (18) and the scattered pulse (C) has increased slightly relative to the reference pulse (D). The pulses at (E) (scattered) and (F) (reference) were produced when the laser was fired again at the low energy level. It is clear most of the change has occurred after the damaging pulse has passed through the sample. This explains why monitoring the damaging pulse after it has exited the sample is not as sensitive in detecting damage in thin films as monitoring changes in the scattered light.

The third technique also utilizes scattered light from the damaged site. This approach is called laser induced scattering (LIS) and is still in use (15, 98). A He-Ne laser beam is directed coincident with the damaging pulse onto the target site. The target site to be tested is viewed through a low power telescope and the scattered light from the He-Ne laser is observed. A change in the scattered light occurs after damage to the target site. This technique has been shown to be effective for detecting single site damage with diameters as small as 3μm (15). This technique is certainly equivalent to the previous one, only the human eye replaces the photodetector. Besides being subjective rather than quantitative, there are other major drawbacks of LIS. It takes considerable practice on the part of the experimenter to obtain the above quoted sensitivity, and in some cases single site damage with a diameter of less than one micron frequently occurs.

Because of the limitations of the above techniques, only visual confirmation of damage under the Nomarski microscope was used to determine the damage threshold. During a test sequence the first and last shot on the sample were heavily damaged. This allowed easy identification of the shot sequence under the microscope and also provided a check of the duplicate alignment stage on the Nomarski microscope to insure that each target site was being rotated into the field of view. For most test sequences it was found that the sample could be rotated from the first damage site to the last under the microscope without any additional adjustment to the sample position. This was possible with a magnification of about 5000 and sites less than 1μm in diameter could be found.

During the course of the experiment between 8,000 and 10,000 target sites were scanned which was only possible because of the ability to rotate through the target sites under the microscope. A complete shot record was kept on each thin film sample and the data recorded was the pulse length, wavelength, and energy level used at every target site. It is possible, by using the shot record and the etch mark on the sample, to find any desired target site under the microscope. This technique was used to obtain the photographs of damage morphology which appear in this dissertation.

A single test run on a specific dielectric thin film sample at one pulse width and wavelength consisted of between 25 and 30 laser shots. The variation in number of shots usually resulted from laser output fluctuations or alignment problems during a run. After the first damaging shot, the next five shots were distributed uniformly over a range

from very low energy to an energy at which a visual plasma could barely be detected. The five sites were examined under the microscope and the highest energy at which no damage occurred and the lowest energy at which damage occurred were noted. The next five shots were placed within this range and so on.

The samples were cleaned prior to each experimental test. The procedure used was to place the samples on a "clean" table. An 8 x 10-1/2 inch sheet of lens cleaning tissue was placed on top of the sample and a small drop of spectral grade ethanol was deposited on the tissue over the sample. Just enough ethanol was used to wet the sample surface. Touching only the tissue, the tissue was pulled across the sample surface until the surface was dry. This was repeated twice.

Figure (19) shows a typical experimental test plotted by the procedure of Bettis, et al. (95, 96). The damage threshold was determined by

$$\text{ENERGY/AREA} = \frac{(E_n + E_d)}{2} \tag{23}$$

where E_n is the highest energy density at which no damage occurs and E_d is the lowest energy density at which damage occurs. The spread in the threshold is taken as

$$E_s = \left(\frac{2|E_n - E_d|}{(E_n + E_d)}\right) \tag{24}$$

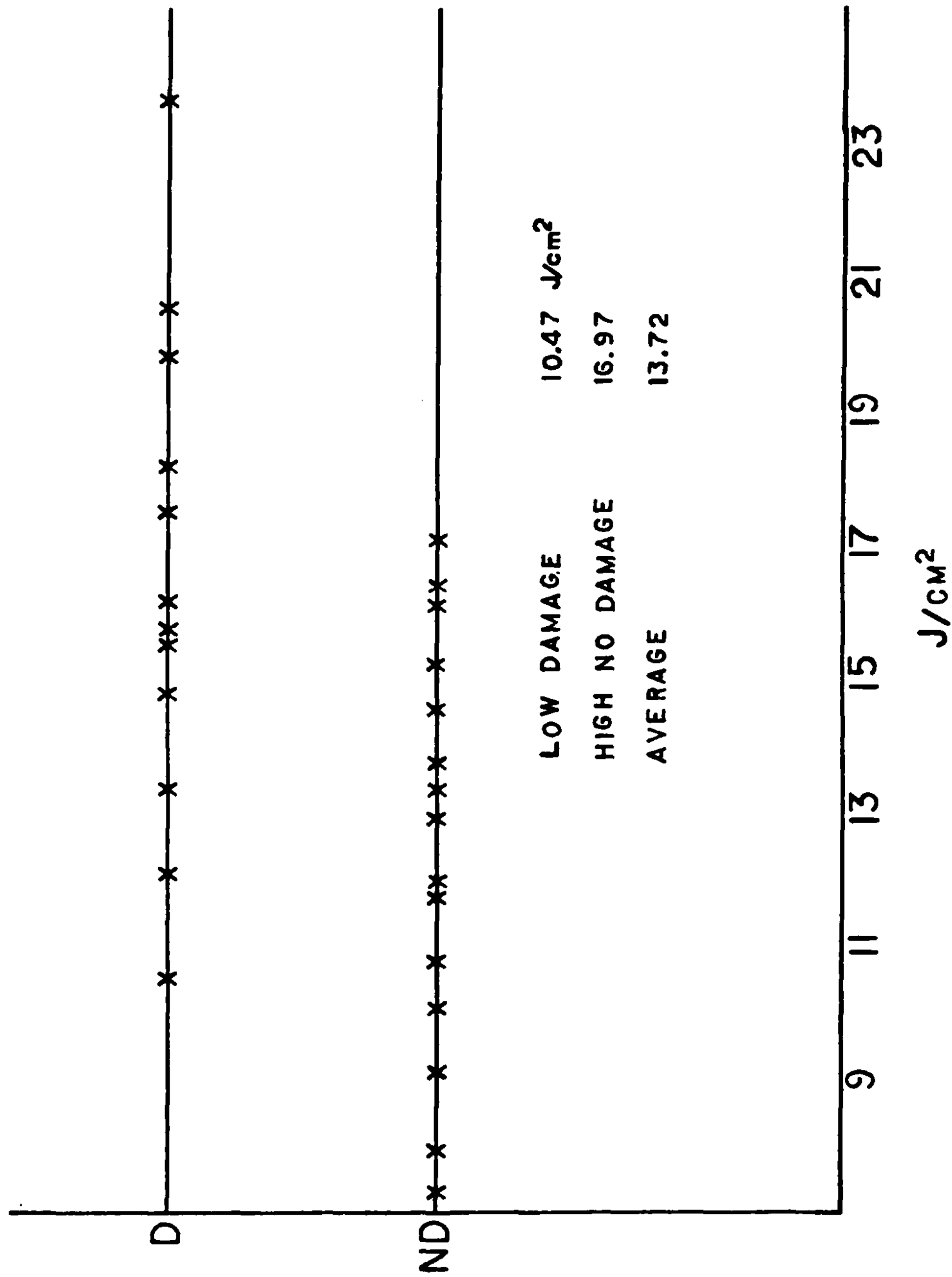

Figure 19. Typical Raw Data for an Al_2O_3 Film

The spread given by E_s is usually taken as a measure of the statistical nature of the breakdown process, but some care must be taken in this interpretation. The experimental errors are found by the following procedure and are errors from the energy measurement, the vidicon response variation, and the measurement of calibration wire diameter. These errors are expressed as fractional standard deviations and were 5%, 7%, and 5% respectively. The fractional standard deviation (fsd) of the experiment can be determined from

$$\frac{\delta(\text{ENERGY/AREA})}{\text{ENERGY/AREA}} = \frac{\left(\frac{\partial f}{\partial M}\right)^2(\partial M)^2 + \left(\frac{\partial f}{\partial C}\right)^2(\partial C)^2 + \left(\frac{\partial f}{\partial X}\right)^2(\partial X)^2}{f(M,C,X)} \qquad (25)$$

where M = energy(E)/vidicon counts(C) and is the calibration factor for the vidicon. The function f(M,C,x) for this experiment is

$$f(MCX) = \frac{MC}{X^2} \qquad (26)$$

x is the effective element width, determined by the wire calibration. In using equation (25) it is assumed that the errors in M, C and x are statistically independent. It is also assumed that systematic errors occur mostly in determining the damage threshold under the microscope. The trends in the data as a function of the various parameters are affected by the systematic errors and therefore do not alter the conclusions of this work. The final calculated fractional standard deviation was 17.1% and is used for the error bars on the data in the graphs in Section IV. The calculated fractional standard deviation due to errors in M alone, was 12.1%. If the measured fsd of 5% had

been used for M, the total experimental fsd would have been 14.8%.

In any event the precision found in the damage thresholds by equation (24) was generally better than either of the above values. In fact, the average variation for the different materials ranged from 7.1% to 10.3% and the average for all of the materials was 9.2%. In this research effort it is not possible to ascribe the variation of the breakdown threshold to the statistics of the damage as opposed to the statistics of the experimental error.

IV. RESULTS

In the previous section the experiment was described and an error analysis of the data was given. In this section the data will be presented, discussed and compared to the three theoretical treatments discussed in Section II. However, before this can be done the following point must be discussed. Since the tested films were deposited in different thicknesses and covered a wide range of indices of refraction, the standing electromagnetic wave formed inside the films had to be considered. The equation for calculating the standing field patterns has been given by Newnam et al. (20), and for normal incidence is

$$\left|\frac{E_1}{E_0}\right|^2 = \frac{t_1^2\left[1 + r_2^2 + 2 r_2 \cos(\delta_1 - k_1 z)\right]}{A^2 + B^2} \tag{27}$$

where

$$A = (1 + r_2)\left[\cos\left(\frac{\delta_1 - k_0 z}{2}\right) + r_1 \cos\left(\frac{\delta_1 + k_0 z}{2}\right)\right]$$

$$B = (1 + r_2)\left[\sin\left(\frac{\delta_1 - k_0 z}{2}\right) + r_1 \sin\left(\frac{\delta_1 + k_0 z}{2}\right)\right]$$

$$\delta_m = 2 k_m d_m \qquad k_m = \frac{4\pi n_m}{\lambda_0}$$

$$r_m = \frac{n_{m-1} - n_m}{n_{m-1} + n_m} \qquad t_m = \frac{2 n_{m-1}}{n_{m-1} + n_m}$$

The indices 0, 1 and 2 refer to air, thin film and substrate respectively. E is the electric field strength, n is the index of refraction and d is the layer thickness.

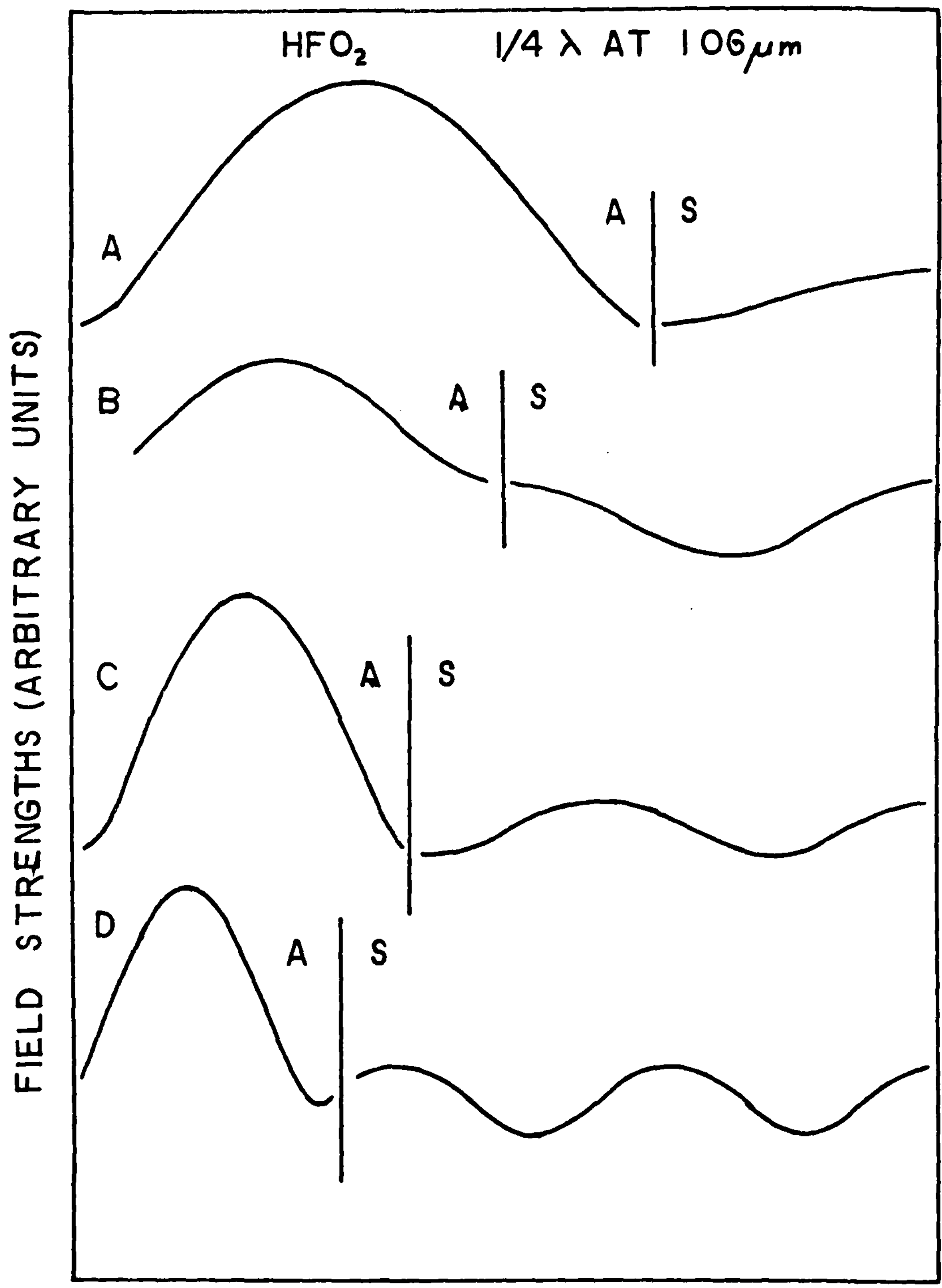

Figure 20. Standing Field Pattern in Air (A) and Film (S) for a HfO_2 Film (A, B, C and D are for 1.06, 0.53, 0.35 and 0.26μm Wavelengths)

Figure (20) shows that the standing field pattern for a 1μm thick HfO_2 film at the four wavelengths of laser radiation. The calculated ratio of the peak internal field (squared) to the peak incident field (squared) was used to obtain the same ratio for the peak energies per unit area incident onto the film. The measured energy/area incident onto the film was multiplied by this ratio to obtain the internal energy densities shown in tables (3-7).

The percentages shown after the data represent the spread in the experimental data given by equation (24) in Section III. The interpretation of these percentages was discussed at the end of the last section and should not be confused with the experimental error which was 17%.

Damage Threshold Changes with Film Thickness

Newnam (20) reported a dependence of the breakdown threshold of TiO_2 films on the film thickness. This dependence was attributed to the different field strengths in the films and the thresholds were found to correlate with the internal field strengths. It can be seen in the data for TiO_2, which has been corrected for the internal field strength, that there is very little difference in thresholds. The fact that the film thickness dependence of damage to TiO_2 disappears when the data is corrected for the internal field strength would seem to support the conclusions of Newnam. However, an examination of all the data for the different film materials reveals that there is an additional thickness dependence of damage in many of the materials. For example, at 15ns and 1.06μm the 1/8λ ThF_4 film damage threshold is more than four times greater than the 1λ film. Since the data has been corrected for the

	λ (at 1.06 μm)	1.06 μm 5 ns	1.06 μm 15 ns	.53 μm 5 ns	.53 μm 15 ns	.353 μm 5 ns	.353 μm 15 ns	.26 μm 5 ns	.26 μm 15 ns
CaF_2	1	12.81± 5.32%	16.61± 7.69%	5.08± 19.9%	10.53± 7.25%	3.29± 4.65%	4.21± 2.57%	2.76± 4.64%	4.60± 18.25%
	1/2	--	19.23± 3.9	6.47± .41	11.94± 9.4	--	--	1.37±36	--
	1/4	16.38± 9.7	27.21±25.74	12.19± 7.79	18.09± 2.4	2.61±41.46	4.94± 9.63	2.23± 1.15	3.64± 0.0
	1/6	--	--	9.70±12.64	19.46± 3.32	5.97± 3.32	9.98± 2.35	2.38±19.46	4.78± 12.9
	1/8	20.21±14.03	31.68± 4.40	14.22± 4.21	22.83± 2.75	9.22± 6.69	18.01±10	2.57± 1.24	5.82± 2.96
Al_2O_3	1	11.40± 9	15.17±14.52	--	13.21± 9.7	3.29±10	6.69±23.11	1.56± 7.16	2.31± 6.35
	1/2	--	17.92±11.80	6.59±0.1	11.71±10.8	--	--	--	--
	1/4	13.15± 1.4	20.14± 9.4	7.33± 5	13.39± 6.3	2.79±10	6.07±10	2.21± 5.86	2.02±11.62
	1/6	--	--	7.13±12.74	13.81± 7.67	3.24±16	5.12± 8.71	--	2.51±15.5
	1/8	20.02±15.33	21.55± 0.89	8.51± 3.8	14.09±19.5	2.92±10	5.98±10	1.76±17.43	2.23±15.28

Table 3. CaF_2 and Al_2O_3 Damage Thresholds (J/cm^2)

	λ(at 1.06 µm)	1.06 µm 5 ns	1.06 µm 15 ns	.53 µm 5 ns	.53 µm 15 ns	.353 µm 5 ns	.353 µm 15 ns	.26 µm 5 ns	.26 µm 15 ns
MgF_2	1	9.29±11 %	13.17± 6.80 %	3.69±10 %	7.90±10.1 %	3.60±10.75 %	4.20± 6.56 %	2.91± 7.91 %	2.43±15.43 %
	1/2	-	15.88± 4.69 %	6.98±13.99%	12.12± 9.7%	-	-	-	2.02± 9.02
	1/4	11.57±16.6%	16.93± 6.89%	7.22±11.5%	14.43± 2.5%	2.72±14.49%	4.7[illegible]± 2.66%	1.93±16.39%	2.95± 9.63%
	1/6	-	-	8.16±10%	14.48± 8.01%	2.85± 7.7%	5.76± 9.69%	1.81± 5.38	3.06± 5.31%
	1/8	27.43±20.86%	37.01±16.49%	8.94± 5.33%	13.96±13.09%	2.37± 7.69%	5.48± 9.65%	1.38±16.28%	3.03± 1.69%
ThF_4	1	6.90± 0.4%	12.27± 9.78%	3.53±10%	8.98± 8.27	4.30± 0.36%	5.63± 2.08	1.50± 9.18%	2.16± 0.22%
	1/2	-	12.91±14.0	6.09±10%	12.58±28%	-	-	-	2.36±15%
	1/4	-	34.77± 9.43%	7.69±10.06%	16.56±12.23	3.16± 6.32%	7.40± 3.40%	1.20± 0.96%	3.95± 2.16%
	1/6	-	-	24.10±28.9%	42.12± 9%	4.14±12.69%	7.69± 2.7%	1.52± 6.55%	3.82± 0.0%
	1/8	28.3[illegible]%	51.86±10.7%	2[illegible].21± 7.81%	43.00± 8.56%	6.93± 5.81%	9.56±15.44%	1.87±14.33%	5.31± 2.89%

Table 4. MgF_2 and ThF_4 Damage thresholds (J/cm^2)

	λ (at 1.06 μm)	1.06 μm 5 ns	1.06 μm 15 ns	.53 μm 5 ns	.53 μm 15 ns	.353 μm 5 ns	.353 μm 15 ns	.26 μm 5 ns	.26 μm 15 ns
ZrO_2	1	8.37±10.15%	-	4.46±14.2%	-	1.17± 3%	-	.82± 4.35%	.76± 7.8%
	1/2	10.02± 5	-	-	-	1.50±29.6	-	-	.59±25.49%
	1/4	10.08±11.7%	9.53± 0.83%	6.78± 2.06%	6.23±13	1.89± 5.95%	2.27± 1.27%	.54±31.79%	-
	1/6	-	-	4.25± 5.25%	4.97±13.36%	1.46± 4.99%	-	.95±18.13	1.14±18.14%
	1/8	10.61± 5.6%	10.90±15.62%	6.01± 5.89%	6.93± 3.4	2.79± 7.81	2.64± 2.88	.70± 1.37	1.07± 4.7
MgO	1	-	-	-	11.47±20	-	-	-	-
	1/2	10.27± 1.4%	9.86± 4.3%	6.19±14.87%	10.03±11.88%	-	-	-	-
	1/4	14.95± 5.7	15.01± 7.4%	8.87± 6.53%	16.25± 2.51%	2.86± 9.11%	3.91± 1.11%	1.31± 5.49%	2.34± 6.15%
	1/6	-	-	7.87±10.94%	14.35± 6.94%	3.15±14.4%	5.53±13.74%	2.18± 2.76%	2.99± 5.23
	1/8	12.21± 3.8%	12.83± 3.8%	10.66±16.88%	14.27± 5.30%	2.87±23.61%	4.30± 9.89	1.66±31.66%	2.61±15.53

Table 5. ZrO_2 and MgO Damage Thresholds (J/cm^2)

	λ(at 1.06 μm)	1.06 μm		.53 μm		.353 μm		.26 μm	
		5 ns	15 ns	5 ns	15 ns	5 ns	15 ns	5 ns	15 ns
HfO_2	1	12.81± 9.5%	-	3.99±19.75%	-	.93± 5.3%	-	1.20± 6	1.19± 7.69%
	1/2	-	-	5.04±10	-	-	-	-	-
	1/4	8.52± 0.5%	13.16± 2.38%	1.78± 4	9.20±14.18%	3.47± 6.67%	4.3[illegible]±22%	.77± 9.63	1.42± 6
	1/6	-	-	.39±10	.73±10	.71±11.71	-	.32± 0.85%	.24± 0.0
	1/8	5.40± 3.5%	7.94± 6.85%	3.47± 2.5%	5.44± 6.59%	[illegible].64± 1.55%	2.73± 8.79%	.43± 5.88%	.73± 1.75
TiO_2	1	8.88±11.5%	-	4.38±28.5%	-	.15± 8%	-	-	-
	1/2	11.42± 9%	-	4.82± 8.2%	-	-	-	-	-
	1/4	14.91± 2.9%	1[illegible].96±14%	6.64± 4%	11.82± 3.12%	.16±10.[illegible]	-	-	-
	1/6	-	-	[illegible].28± 9.46%	8.88± 2.7%	.06± [illegible]	-	-	-
	1/8	10.07±10%	9.88± 7.06%	6.44±13.93%	10.82± 1.1%	.62± 0.0%	-	-	-

Table 6. HfO_2 and TiO_2 Damage Thresholds (J/cm^2)

SiO_2	λ(at 1.06 μm)	1.06 μm 5 ns	1.06 μm 15 ns	.53 μm 5 ns	.53 μm 15 ns	.353 μm 5 ns	.353 μm 15 ns	.26 μm 5 ns	.26 μm 15 ns
	1	-	-	-	-	-	-	-	-
	1/2	-	-	7.85± 5.71%	-	-	-	-	-
	1/4	22.49± 0.20%	45.09±12.31%	9.41±14.5%	19.61± 5.9%	5.63± 9.33%	10.72± 2.2%	.96± 9.84%	1.69±10.56%
	1/6	-	-	-	-	-	-	1.36± 9.42%	-
	1/8	41.44± 1.3%	47.32±10.25%	21.16±13.4%	48.47± 4.29%	-	13.50± 9.71%	2.25± 9.42%	2.54±12.29%

Table 7. SiO_2 Damage Thresholds (J/cm^2)

internal field strengths, this film thickness dependence of damage is unexplained.

All of the fluoride films show a prominent increase in damage threshold with a decrease in the film thickness. This phenomenon is weaker and in some cases non-existent in the oxide films. Al_2O_3, MgO and SiO_2 all had a film thickness dependence of damage, however, ZrO_2, HfO_2 and TiO_2 showed essentially no dependence.

The film thickness dependence of damage is further complicated by changes in the laser wavelength and pulse length. All of the data shows that the thickness dependence in fluorides is strong at 1.06μm and becomes progressively weaker at shorter wavelengths and pulse lengths. In fact, there is no thickness dependence in ThF_4 at 0.26μm and 5ns pulse length. SiO_2, Al_2O_3 and MgO damage thresholds exhibited a weaker but similar trend with changes in film thickness.

Damage Threshold Dependence on Pulse Length

The MgO and TiO_2 thin film damage contain another important feature. There is essentially no laser pulse length dependence in the TiO_2 films at 1.06μm; however at 0.53μm the damage threshold increases with longer laser pulses. The MgO films behave the same at 0.53, 0.35 and 0.26μm in that they show a pulse width dependence at these wavelengths, but not at 1.06μm.

The fluoride films show a much stronger dependence of damage on pulse width at 0.26μm than the oxides. In fact Al_2O_3, SiO_2 and ZrO_2 film data indicates a weak laser pulse width dependence at 0.26μm. The only oxide films which exhibit a marked time dependence at 0.26μm are MgO and HfO_2.

Damage Threshold Dependence on Wavelength

Another important aspect of the data is the change in damage threshold with the laser wavelength. In most cases the threshold drops as the laser wavelength decreases. There are a few exceptions to this observation; at 15ns the 1/8λ(λ=1.06μm)TiO_2 and the 1/8λ and 1/4λ MgO films do not decrease in damage threshold between 1.06 and 0.53μm, but at 5ns the damage threshold of all the films decrease as the laser wavelength decreases.

The variation of damage threshold with wavelength can also be determined from the data to be a function of the film thickness. For example, the 1/8λ ThF_4 film decreases by a factor of about fifteen in going from 1.06 to 0.26μm, whereas the 1λ film only decreased by a factor of about three. This phenomenon is seen to hold true for all of the materials except TiO_2, which was not tested at 0.26μm, ZrO_2 and MgO.

To summarize the observations made to this point, we can say that in general the films exhibit a thickness dependence on damage threshold which cannot be explained by the different internal electromagnetic fields in the films. This influence of film thickness on damage is further affected by the laser pulse width and wavelength. The next feature which can be clearly seen in the data is the dependence of damage threshold on laser pulse width. This phenomenon has been reported in other research (3, 19, 21-25, 53). This effort is unique in that a large number of different thin film materials (nine) have been tested at two different laser pulse widths over a range of different film thicknesses and wavelengths. The large matrix of data

obtained will aid in evaluating the physical causes of the influence of laser pulse width on the breakdown threshold.

The pulse length dependence is stronger for the fluoride films than for the oxide films. We note for example that at 1.06μm CaF_2 data shows a consistent increase in damage threshold at all film thicknesses in going from 5ns to 15ns. The same behavior is not as marked in Al_2O_3, TiO_2, MgO, or ZrO_2 data. In fact, the last three materials do not exhibit any laser pulse width effect at 1.06μm.

Observations on Damage Morphology

Wavelength, pulse length and film thickness are all important parameters which have been observed to influence the damage threshold of thin films. There is another parameter which can be utilized to provide clues to the nature of the breakdown mechanism. This is the observation of the damage site morphology. In Figure (21) a sequence of four damage sites for MgO is shown. Each photograph was taken on the same MgO film at the same magnification. The damage sites were produced by 5ns laser pulses at wavelengths of 1.06, 0.53, 0.35 and 0.26μm. The two most obvious features of the morphology are the decrease in damage site size and increase in the number density of sites as the laser wavelength decreases. The same general behavior of the morphology was observed in all the thin film although the change was not as dramatic in the oxide films, except for MgO, as in the fluoride films.

At 0.26μm there was an additional change in the oxide film damage morphology. At the longer wavelengths the morphology was that of individual cratered sites as shown in Figure (21). At 0.26μm the damage morphology became more uniform in appearance. The damage at 0.26μm for

1.06 μm

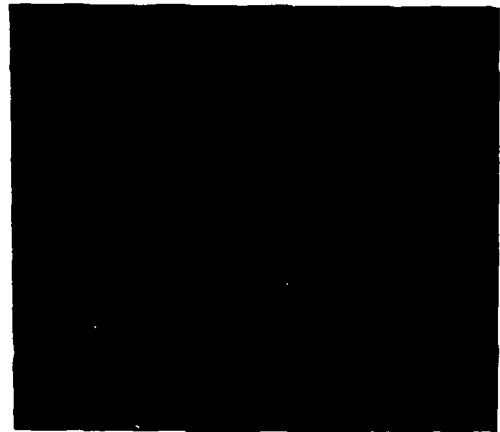

0.53 μm

0.35 μm

0.26 μm

Figure 21. MgO Damage Morphology vs. Wavelength

Al_2O_3, SiO_2, HfO_2, and ZrO_2 is shown in Figure (22). For completeness, the damage sites in ThF_4 for different wavelengths are shown in Figure (23). The individual crater sites, which are evident in the damage at 0.26μm, were observed for all the fluoride films and MgO as opposed to the uniform and diffuse damage in the rest of the oxide thin films.

All of the films were not tested at every wavelength, pulse length and film thickness. The two most obvious cases are the MgO and TiO_2. The 1μm MgO film was not tested at most wavelengths because of the quality of the film. Under the microscope there were so many "chunks" of impurities or foreign matter in the film that it was generally impossible to locate the damage sites unless the damage was catastrophic. The TiO_2 films were tested at 0.26μm, however, the threshold was so low that to obtain meaningful data the dynamic range of the vidicon system would have required adjusting and recalibrating the system. Time constraints would not permit this.

An additional point concerning the TiO_2 films involves the absorption edge of bulk TiO_2 which is at 0.3μm, close to the 0.35μm laser radiation. It can be seen from the data that the damage threshold drops by more than an order of magnitude in going from 0.53μm to 0.35μm. The measured absorptance is a factor of four higher at 0.35μm than at 0.53μm; a similar change for the other oxides occurs between 0.35μm and 0.26μm. At 0.26μm the laser radiation photon energy is well past the absorption edge of TiO_2 and damage can be ascribed to linear absorption. The damage morphology of TiO_2 goes from single site to uniform morphology just as the other oxide films; however, in the case of TiO_2

TiO_2

HfO_2

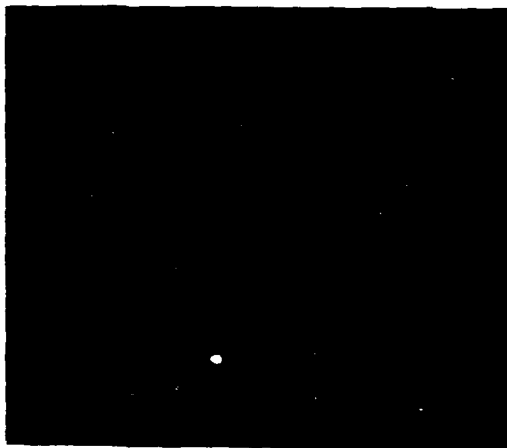

ZrO_2

SiO_2

Figure 22. Oxide Damage Morphology at 0.26μm

1.06 μm

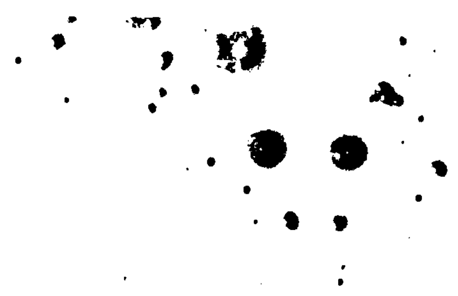

0.53 μm

0.35 μm

0.26 μm

Figure 23. ThF_4 Damage Morphology vs. Wavelength

the change occurs at 0.35μm rather than 0.26μm. The TiO_2 damage at 0.35μm looks the same as the ZrO_2 damage at 0.26μm shown in Figure (22). Between 1.06 and 0.53μm TiO_2 films show the same decrease in single site size and increase in density as the other materials.

The observations made above can be summarized as follows:

1. In general, films exhibit a damage threshold which depends on film thickness in a way that can not be explained by internal electromagnetic fields.
2. The fluoride films show a stronger dependence of damage threshold on film thickness than the oxide films.
3. MgO and TiO_2 damage thresholds have no pulse width dependence at 1.06μm but do at shorter wavelengths.
4. The damage thresholds of fluoride films show a stronger laser pulse width dependence than those of oxide films.
5. ZrO_2 damage thresholds have essentially no pulse width dependence at any wavelength.
6. Al_2O_3, SiO_2, and ZrO_2 damage thresholds exhibit little or no pulse width dependence at 0.26μm.
7. MgO and HfO_2 damage thresholds have a marked time dependence at 0.26μm.
8. The thin film damage thresholds decrease with decreasing laser wavelength.
9. In general the film thickness dependence becomes weaker at shorter wavelengths. That is, the decrease in damage threshold is more pronounced for thin films than for thick films.

10. The individual damage site size decreases and the number density of sites increases with decreasing laser wavelength.
11. The change in site size with wavelength is not as pronounced for the oxides as for fluorides except in the case of MgO.
12. The damage morphology of most oxide films changes at 0.26μm from individual craters to a uniform area damage.
13. The damage morphology of TiO_2 films changes at 0.35μm.
14. The damage morphology of the $1/6\lambda(\lambda = 1.06\mu m)$ HfO_2 film is the same at all wavelengths and looks like the 0.26μm damage morphology of the oxides shown in Figure (22). Also the damage thresholds of the $1/6\lambda$ HfO_2 is much lower than any other HfO_2 film.

Comparison of Theory and Experiment

The predicted pulse width dependence was discussed in Section II for the three theoretical models. The weak pulse width dependence of some of the oxide film data, particularly ZrO_2, does not come close to fitting with the expected pulse width dependence given by equations (3) and (6) for the avalanche ionization. Because the avalanche model predicts an extremely strong pulse width dependence ($\sim t_p$) the fluoride film data also can not be explained by this model in terms of laser pulse width effects which more closely fits a $t_p^{1/2}$ dependence. More importantly, there is nothing in the avalanche model which can account for a change in the pulse width dependence of damage with a decrease in laser wavelength, as observed in MgO and TiO_2. The conclusion is that the avalanche ionization model does not provide a good explanation of the observed pulse width dependence trends in the data.

The multiphoton model does predict a change in pulse width dependence with laser wavelength. It can be seen from equation (11) that as the laser wavelength is decreased the pulse width dependence of damage becomes weaker, which is in exact contradiction with the experimental data, especially for the oxides. The closest that the multiphoton model comes to agreeing with the oxide film data is at 0.26μm. At this wavelength the multiphoton model would predict, based on equation (11) and bulk material parameters, a pulse width dependence which would go like $(t_p)^{1/2}$. Although this dependence fits for some of the oxide materials it does not for the majority. However, since fluoride bulk material band gaps are around 8 electron volts, the predictions of equation (11) do give reasonable agreement with the fluoride data at 0.26μm.

For one photon or linear absorption, equation (11) predicts that there would be no pulse width dependence. At 0.26μm the photon energy is slightly less than 5 electron volts (ev) and therefore, based on bulk parameters one photon absorption would not occur in the films. The band edges of all the oxides which exhibit weak pulse length dependence are all greater than 5ev. Atomic impurities, structural inhomogeneities and finite physical dimensions of crystalline structure in thin film form, produce energy levels within the band gap. Although for dielectric materials these levels are generally shallow, they can reduce the effective band gap of the material. Thus it is possible that one-photon absorption based on bulk material parameters could explain the oxide film data at 0.26μm.

In support of the above comments on one-photon absorption is the fact that the measured absorptance of TiO_2 at 0.35μm, which is just below the bulk material band gap in photon energy, was .133. Near 0.26μm the rest of the oxides, except MgO, which had a lower absorptance, had an absorptance of about .15. Thus the similarity of absorptance between TiO_2 at 0.35μm and the other oxides at 0.26μm suggests that the effective band gap could be substantially smaller than theory would indicate.

To conclude the comparison of multiphoton theory with the data, we can say that multiphoton theory gives a good pulse width dependence only with the fluoride data at 0.26μm. One-photon absorption would agree with the pulse dependence observed in Al_2O_3, SiO_2, and ZrO_2 at 0.26μm. The similarity in absorptance in these oxides at 0.26μm and TiO_2 at 0.35μm lends some support to one-photon absorption as a damage mechanism in these materials at 0.26μm.

The wavelength dependence of breakdown in the avalanche model is clearly contained in equation (3). Unless $(E_g/mL_{ac}^2)^{1/2}$ is much greater than the laser frequency w, the damage threshold increases as the laser wavelength decreases. An examination of the experimental data in tables (3-7) shows this prediction to be in contradiction with the data. The MgO data for a 15ns laser pulse at 1.06 and 0.53μm is the only data which does not decrease in going to shorter wavelengths. The avalanche model would predict a constant damage threshold with decreasing wavelength if $(E_g/mL_{ac}^2)^{1/2}$ were much greater than w, in agreement with the MgO data. However, this model completely fails in explaining the wavelength dependence of damage in the rest of the data.

The multiphoton model based on the Keldysh theory (39) predicts a damage threshold which decreases with decreasing wavelength as shown in Figure (1). This is the same trend that is seen in all of the experimental data except for MgO between 1.06 and 0.53μm. However, the calculations based on bulk material parameters give absolute damage thresholds which are usually more than an order of magnitude larger than the thresholds measured in this effort (92). Neglecting the last point we could conclude that the multiphoton model predicts the observed trends of damage threshold with laser wavelength in the experimental data.

The damage morphology must also be discussed in terms of the avalanche and multiphoton models. There is no conflict with the observed single site crater morphology shown in Figures (21 and 23). Originally it was believed that this type of morphology was indicative of impurity damage (53, 63). However, it has been pointed out by Epifanov (6) that formation of small plasmas as a result of avalanche ionization could produce the same morphology in the nanosecond pulse regime. In this pulse width regime the electron diffusion rate would not be significant in a volume whose diameter was between one and three microns. In this research work the problem in explaining this morphology within the context of avalanche ionization is the change of morphology with laser wavelength. A decrease in site size could be explained in the avalanche model through a change in pulse length which affects the extent of the electron diffusion. However, nothing in the avalanche model can account for a change in site size with wavelength, or the increase in the number density of the sites at shorter wavelengths.

With this model the density of sites has to be interpreted in terms of the location and density of initiating electrons and the density of initiating electrons is not a function of laser wavelength.

For a pure intrinsic material the multiphoton model would give even less agreement. The absorption would occur uniformly over some area which coincided with the peak irradiance of the laser pulse. The resultant damage morphology would be uniform like the morphologies shown in Figure (22), and the morphology would not appear as isolated damage sites.

Certainly thin films can not be regarded as intrinsic materials. It may be possible that a high density cluster of atomic impurity levels occurs in the film and produces an isolated damage site. This type of effect could also explain the observed increase in number density as the wavelength decreases since more impurity clusters might participate in the damage process as the number of photons required decreases. The major difficulty with the cluster hypothesis is an explanation of a decrease in site size with a decrease in laser wavelength. We would have to argue that the size of the clusters which produce damage is influenced by laser wavelength. Currently there is no physical evidence or reasonable conceptual mechanism on which to argue this case.

The morphology discussion given above suggests the possibility that a combination of the multiphoton and avalanche models could give a better fit to the experimental data. For example, it is possible to explain the increase in number density of damage sites by multiphoton initiated avalanche ionization in MgO. This could explain the lack of decrease in threshold between 1.06 and 0.53μm and then the decrease at shorter wavelengths as multiphoton effects begin to dominate. This

situation is given as the combined theory in Figure (1). Some of the other materials such as ZrO_2, HfO_2 and TiO_2 which have a weak decline in damage threshold between 1.06 and 0.53µm and then a stronger decline at shorter wavelengths might also be explained by a combined theory. The materials which show a strong decline between 1.06 and 0.53µm would have to be explained by a strictly multiphoton dominated process.

The last point highlights some of the failings of the combined theory. If multiphoton processes were to dominate over avalanche ionization at some wavelength, they would be expected to do so first in materials with the smallest band gaps. The absoprtion edges for MgO, HfO_2, ZrO_2 and TiO_2 are 0.175, 0.24, 0.24 and 0.3µm respectively (93). For MgF_2 and CaF_2 they are 0.113 and 0.124µm. Based on bulk material parameters the multiphoton process should dominate in the oxides before the fluorides which is in exact contradiction with the experimental data. The major difficulty in trying to interpret the experimental data with the combined theory is that the interpretations based on pulse width and wavelength behavior for one material give inconsistent results when applied to another material. In addition, there is no explanation for the change in damage site size with wavelength.

The only conclusion that can be drawn is that although both the avalanche and multiphoton models, either separately or combined, can account for isolated sections of the data, but contradictions accrue when all of the data is dealt with as a whole. The trends observed in the data are not adequately described by these two models.

This conclusion is further substantiated by the fact that neither the avalanche nor the multiphoton theory contain any feature which [illegible] account for the observed film thickness dependence [illegible]

AD-A096 051 AIR FORCE INST OF TECH WRIGHT-PATTERSON AFB OH SCHOO--ETC F/6 11/3
LASER-INDUCED DAMAGE TO THIN FILM DIELECTRIC COATINGS.(U)
OCT 80 T W WALKER
UNCLASSIFIED AFIT/DS/PH/80-4 NL

2 OF 2
AD A
096051

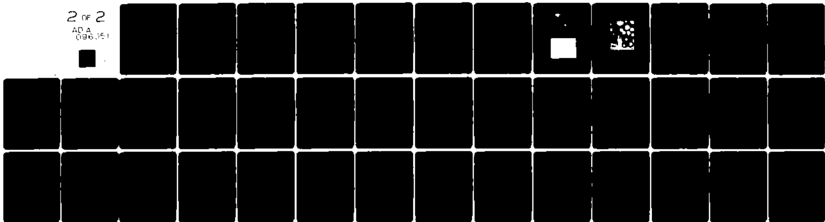

END
DATE
FILMED
4-81
DTIC

not occur naturally in these two theories.

The impurity model can be examined in terms of the same trends in the experimental data. Figures (24) to (27) provide a comparison of the ThF_4 data to theoretical calculations based on equations (19) and (20). In each figure the damage threshold is plotted as a function of the film thickness and the solid curves are the theoretical calculations. In the case of ThF_4 the impurity was modeled as ThO_2. The existence of this impurity or $ThOF_2$ in ThF_4 films has been supported (78) and fortunately, thermal constants for ThO_2 were available.

The most obvious feature of this impurity model is the prediction of an increase in damage threshold with a decrease in film thickness. This occurs because it is assumed in the model that the maximum size an impurity can have is limited by the film thickness. That is, as the film thickness increases so do the impurity sizes. This situation has been well supported by work at Perkin-Elmer (77) in which this phenomenon has been observed for many types of films.

The theoretical curves in the figures are adjusted to the data at each wavelength. This is done by selecting one data point for either the 5ns or 15ns data and normalizing the appropriate theoretical curve at that point. The other theoretical curve for the remaining pulse width is then normalized by the same factor so that the relative position between the two curves are not changed. Therefore, the theortical curves in each figure have been normalized to a single data point.

It is apparent from the figures that this model gives a good prediction of both the film thickness and the pulse width dependence of the damage threshold in ThF_4. The theoretical curves also fit the data

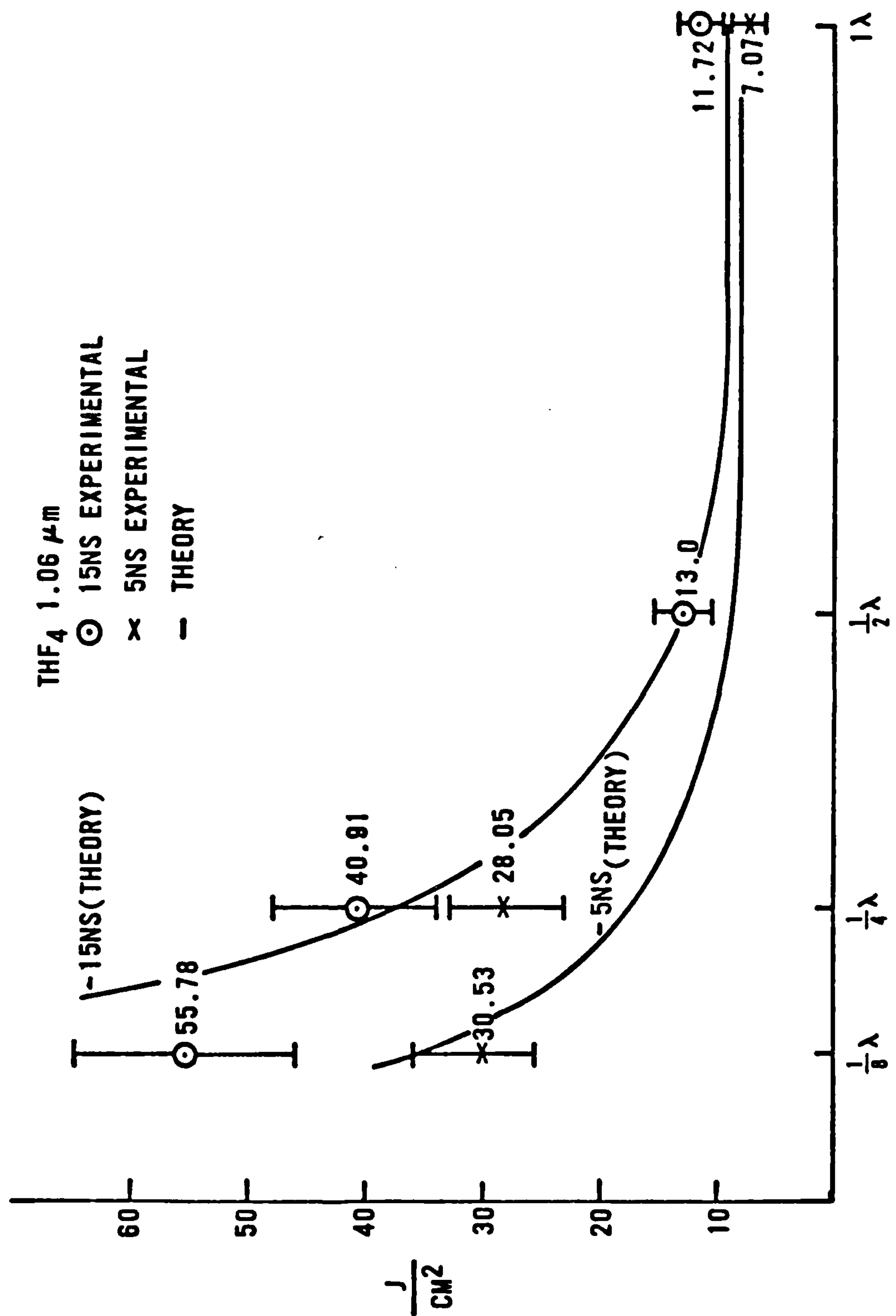

Figure 24. Damage Threshold of ThF_4 at 1.06μm vs. Film Thickness

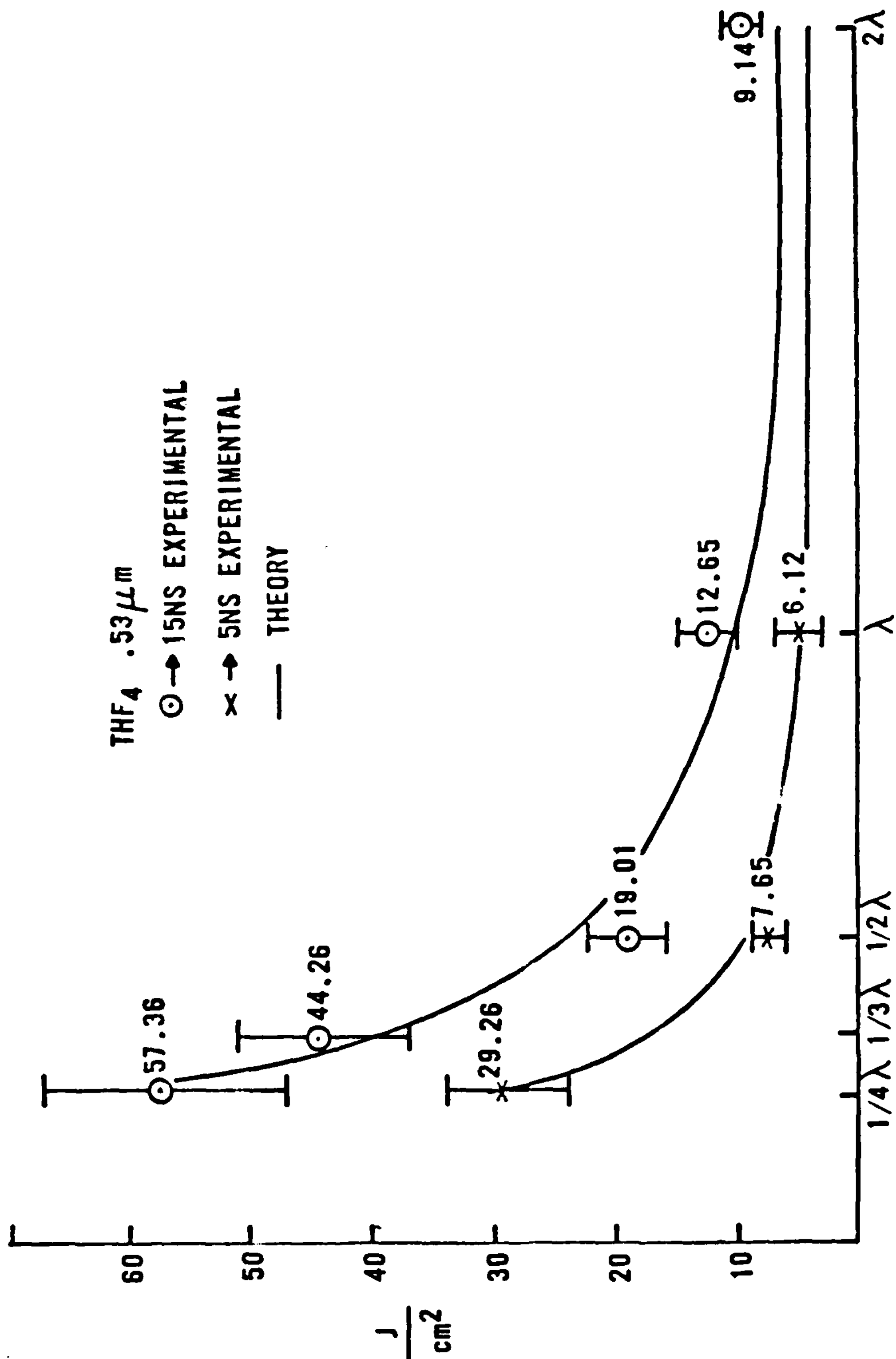

Figure 25. Damage Threshold of ThF_4 at 0.53μm vs. Film Thickness

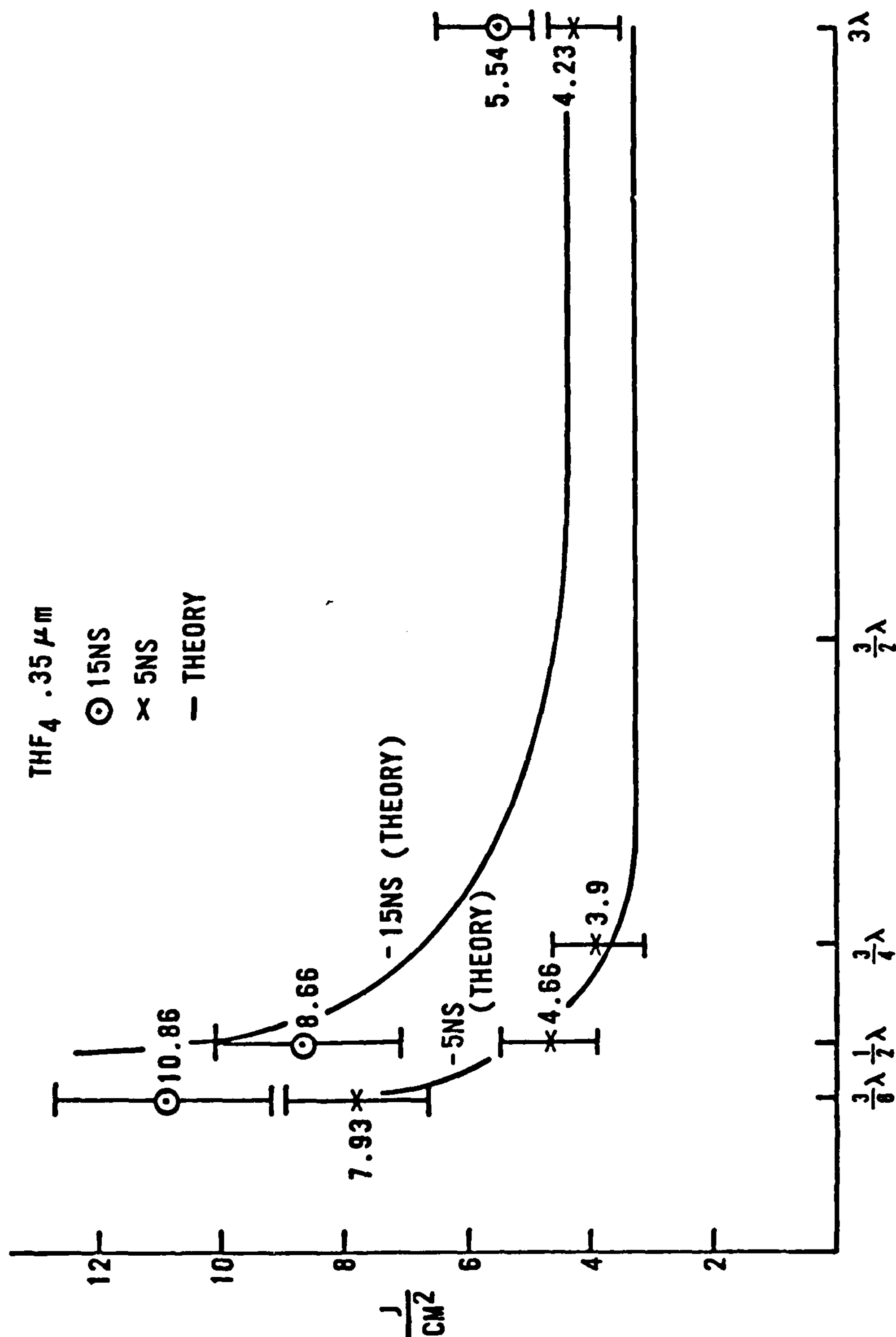

Figure 26. Damage Threshold of ThF_4 at 0.35μm vs. Film Thickness

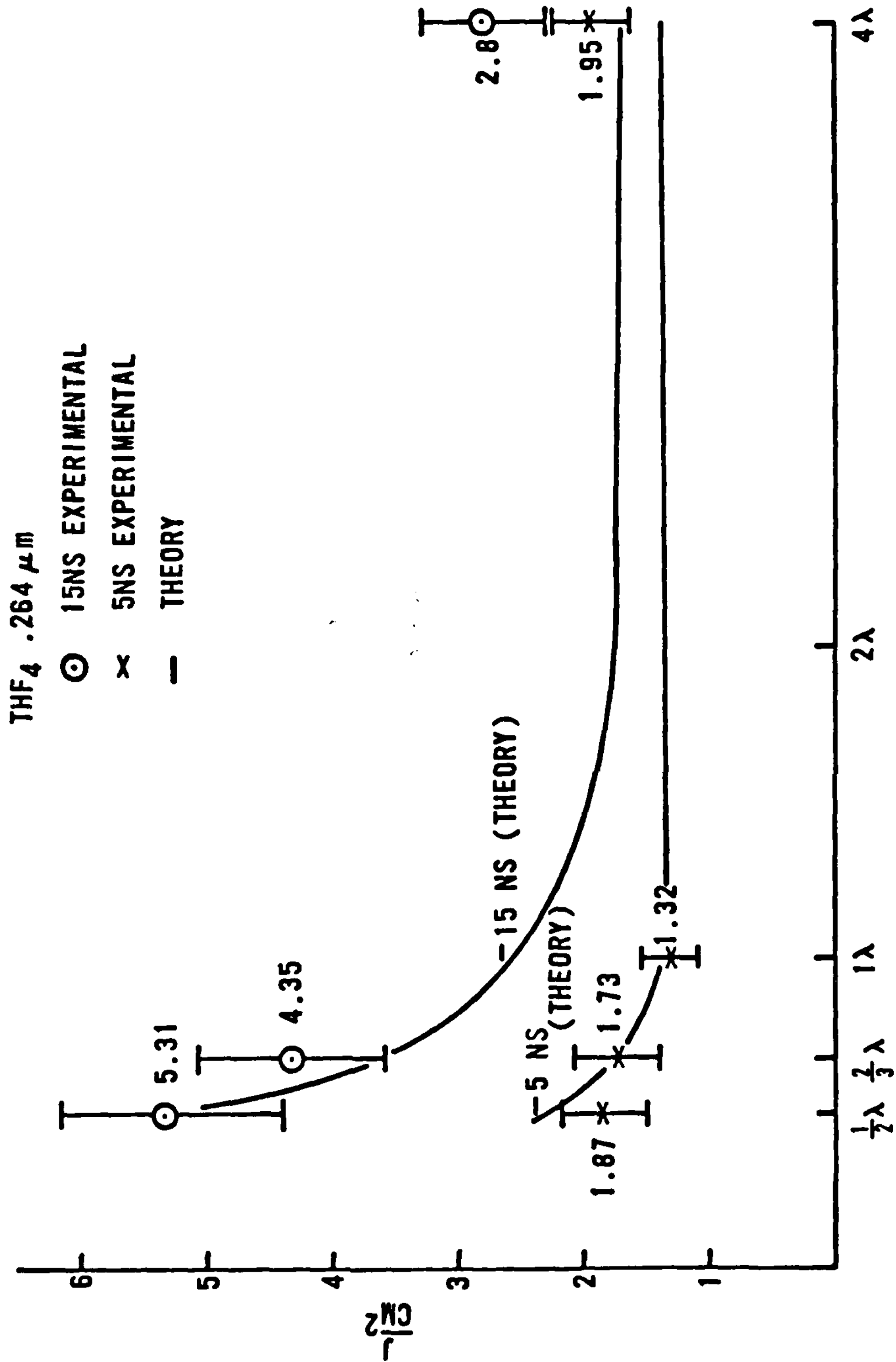

Figure 27. Damage Threshold of ThF_4 at 0.26μm vs. Film Thickness

as a function of the laser wavelength and predict the observed decrease in film thickness dependence of damage at shorter wavelengths. The greatest point of disagreement is at 15ns and 1.06μm for the 1/8μm thick film. The measured damage threshold is close to that of the bare surface fused silica threshold. It is at this point that we would expect the greatest departure from theory because of the very high energy densities involved. Many more effects can become important at these high field strengths which could reduce the measured from the predicted threshold. The theoretical curves show a flattening over more of the film thickness at 0.35 and 0.26μm as opposed to 1.06 and 0.53μm. It is not evident in the Mie cross-section given in equation (20) and the thermal equation (19), but the impurity theory predicts that when the laser wavelength is reduced, the size of the impurity that is most sensitive to damage is also reduced. The flattening of the theoretical curves at the shorter wavelengths occurs because the size of the impurity which is easiest to damage is not exluded by most of the very thin films. The value of film thickness at which the damage thresholds begin to rise is also shifted to thinner films at shorter wavelengths for the same reason. Both of these trends are observed in the data.

The 0.35 and 0.26μm curves indicate that the 1μm thick film damage thresholds are above the theoretical curves. One explanation for this is that as the impurities become smaller the ratio of the volume of film material required to be removed during the damage process to volume of impurity increases. The smaller particles absorb less total energy and additional energy must be deposited for material removal to occur and be visually recorded as damage. Evidence for this effect is shown

in Figure (28). The damage sites are for MgF_2 and ThF_4 1μm thick films damaged at 0.26μm. The small light spots appear to be damage sites at which the film surface has not yet been ruptured. These light spots are seen only in regions that have been irradiated by the laser beam. A more graphic recording of this effect is shown in Figure (29). This picture of ThF_4 damage was taken with a scanning electron microscope (SEM) and shows clearly the development of cratering as a result of damage. If the film is damaged with an even higher energy laser pulse, material is removed in a large region as if the density of the craters became high enough to overlap (Figure 28). The center of the region is covered with many small pits and the light spots are seen only outside the edge of the area.

The curves for the ThF_4 data are representative of all the fluoride film data. In contrast, Figures (30) and (31) show the behavior of Al_2O_3 which are for 1.06 and 0.26μm laser wavelengths. We note that there is a weaker sensitivity of damage to film thickness, and although the agreement is not as good as with fluorides this feature is accounted for in the impurity theory. The decrease in sensitivity of damage on film thickness is a result of the five to six times smaller thermal conductivity of Al_2O_3, compared to the fluorides. A lower thermal conductivity of the host material relative to the impurity reduces the thermal losses from the impurity and smaller impurities are damaged. This behavior has the same effect in Al_2O_3 as going to shorter wavelengths in ThF_4. In fact the 1.06μm curve for Al_2O_3 is quite similar to the 0.26μm curve for the ThF_4 films.

ThF_4

MgF_2

Figure 28. Damage Morphology for Thick (1λ at 1.06μm) ThF_4 and MgF_2 Films

Figure 29. Electron Micrograph of ThF_4 Damage Sites

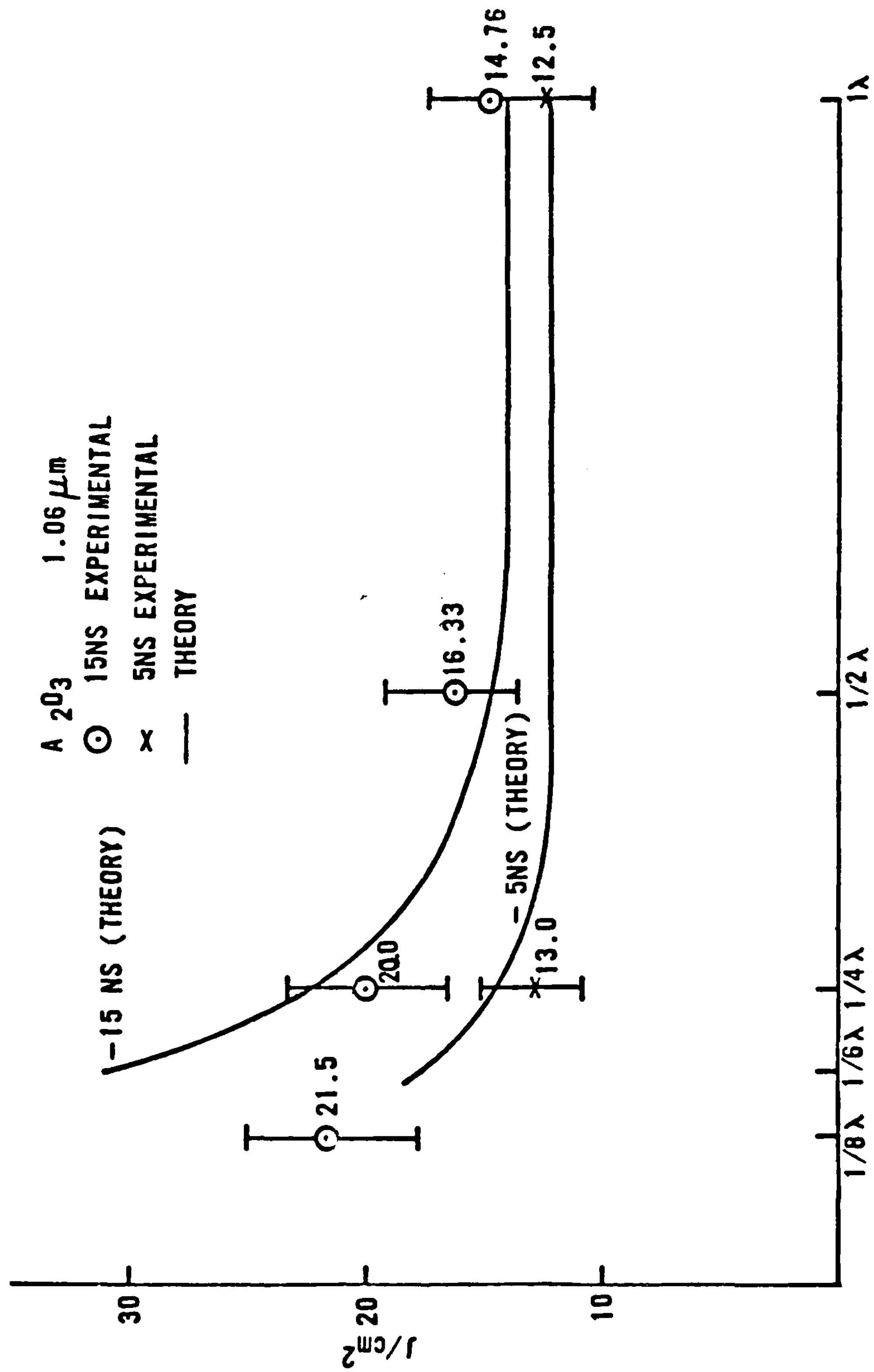

Figure 30. Damage Threshold vs. Film Thickness for Al_2O_3 at 1.06μm

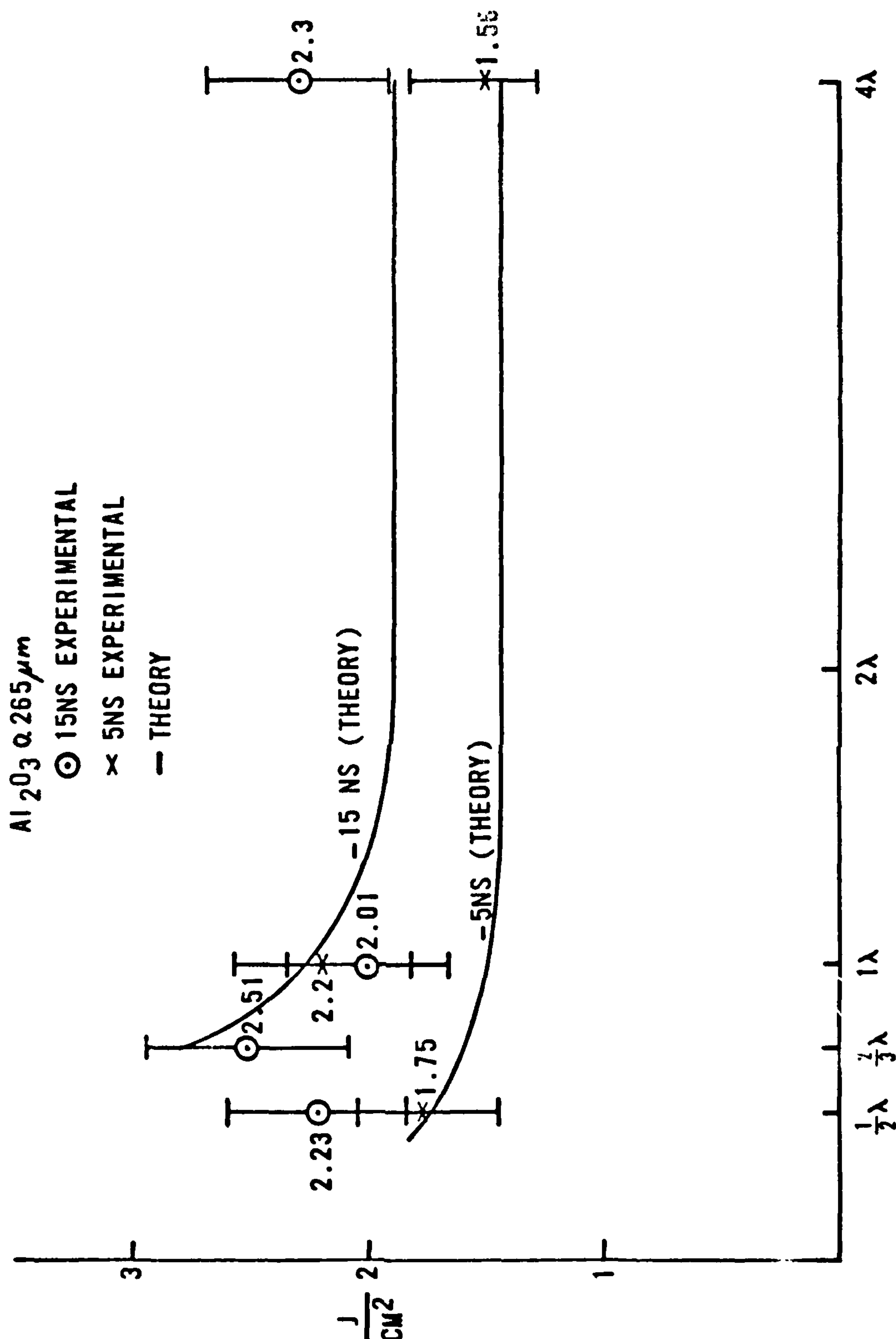

Figure 31. Damage Threshold vs. Film Thickness for Al_2O_3 at 0.26μm

The composition of the impurities in Al_2O_3 films is not known so the parameters of a dielectric type impurity were used and varied to obtain a reasonable fit to the data. From Figure (6) and equation (21), it can be shown that the Mie cross-section for metallic impurities increases for smaller particles over the wavelength range of interest. Thus, metallic impurities would damage at even smaller sizes, and further weaken the film thickness dependence.

In general, the thermal conductivity of oxide materials is smaller, by a factor of five to an order of magnitude, than the thermal conductivity of fluoride materials. The smaller energy loss from impurities in oxide films leads to a prediction by the impurity model of weaker pulse width and film thickness dependence in oxide films than in fluoride films. These trends were observed in the data. The impurity model also predicts that the film thickness dependence in oxides should become weaker and the pulse width dependence stronger with a decrease in laser wavelength. This predicted behavior is observed in Al_2O_3, TiO_2 and MgO.

Since the comparison between theory and experiment in Figures (24) through (27) was made by normalizing the curves at each wavelength, they do not provide a reasonable picture of the predicted wavelength dependence. Figure (32) compares the theoretical and experimental values of the damage threshold of CaF_2 films as a function of wavelength. The theoretical predictions and experimental data are given for both 1/8 and 1μm thick films. The theory and experiment both show a faster drop in the damage threshold for the 1/8μm film than for the 1μm film as the wavelength decreases. The theoretical curve for the 1/8μm has

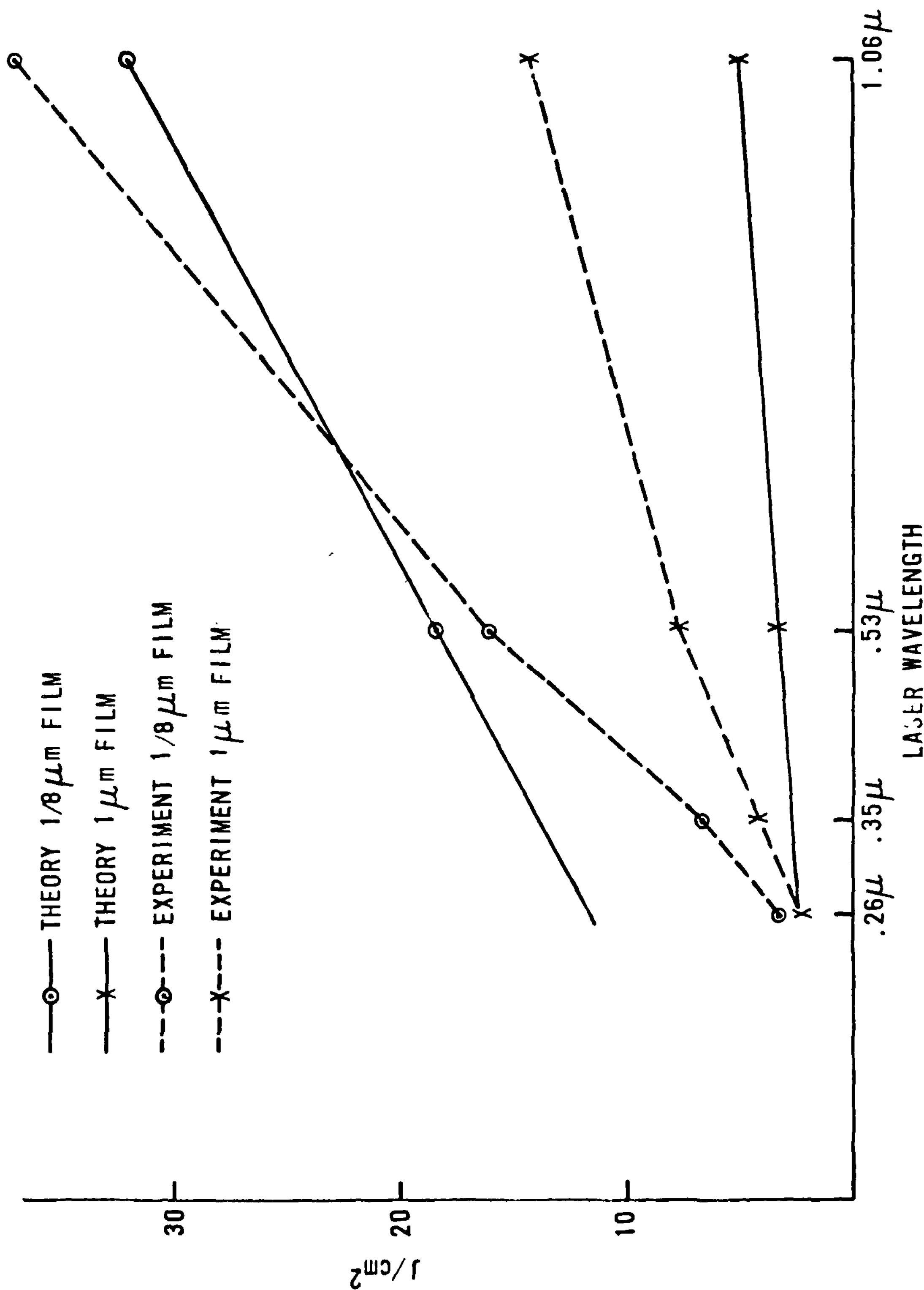

Figure 32. CaF_2 Damage Thresold vs. Laser Wavclength at Two Film Thicknesses

been normalized for clarity to the 1.06μm data point. Although the theoretical curve for the 1μm film is normalized at 1.06μm the relative positions of the two curves was not changed. The experimental data shows a faster decrease in the damage threshold at 0.53μm than the theoretical curves. One explanation for this can be found in the imaginary index of refraction used in the Mie absorption cross-section. The index was picked to fit with a transparent dielectric impurity (less than .01) at 1.06μm. For this case the imaginary index of refraction increases with decreasing wavelength. This fact was not included in the theory because of the lack of knowledge of the impurity composition. Based on absorption curves for dielectric materials this increase could be expected to be more pronounced at wavelengths shorter than 0.53μm. However, without a detailed knowledge of the impurities it is not possible to bound the magnitude of this effect. What can be said is, that if the wavelength dependence of the index could have been included in the theory, the curves would also have exhibited a faster drop in the damage threshold at shorter wavelengths. However, the impurity theory does predict the observed general trends of a drop in damage threshold as the wavelength is decreased.

Finally, we will examine the observed damage morphology within the context of the impurity model. Figures (21) and (23) show that the individual damage sites decreased in size with decreasing wavelength. This trend was noted to be a general behavior in all of the films except TiO_2 at 0.35μm and the other oxides at 0.26μm. Since the impurity model predicts that the size of the damaging impurity decreases with decreasing wavelength, this would explain the observed morphology.

Research has been conducted to characterize the number density of impurities as a function of their scattering cross section in thin films (62, 68). Artm'ev et al. (62) showed that the number density increased by two orders of magnitude as the cross-section decreased from $3x10^{-9}$ to $1x10^{-9}$ cm^2. For particles smaller than the test wavelength (Artem'ev used 1.06μm) the cross-section decreases as the particle size decreases (81, 94). The particular particle size at which the decrease in cross-section begins, depends on the real and imaginary index of refraction; but in general it occurs for particles whose radius is slightly smaller than the wavelength of the light. The implied increase in number density with a decrease in particle size is supported by the work of Leonov, et al. (73). They found, in bulk glass, that the number density of microinclusions increased from $3x10^6$ to $1x10^{11}$ cm^{-3} as the particle radius decreased from 0.3 to 0.1μm. With this strong evidence as support, the impurity model would also predict an increase in the number density of damage sites with a decrease in laser wavelength. From Figures (21) and (23) we can see that this is exactly what occurs.

It was noted that the oxides in general do not exhibit as marked a change in morphology with wavelength as do the fluorides. The theory predicts that smaller impurities will damage in the oxides than fluorides because of their smaller thermal conductivities. In this case it would be expected that the morphology change would be less noticeable. Also the apparent morphology change in the oxide films at 0.26μm shown in Figure (22) might be similarly explained.

As previously noted, number densities as high as 10^{11} cm^{-3} were reported by Leonov (73) in bulk material. The morphology such as that

seen in Figure (22) could result from very densely packed small sized impurities. In addition if the damage is produced by many closely spaced impurities then the total damaging process would be a collective action of many impurity interactions. An impurity model based on this mechanism has been treated to some degree by several Soviet workers (60, 67). The amount of energy which thermally diffuses is reduced from any one impurity since the host material is heated by numerous close neighbor impurities and the heat flow from any one impurity depends, of course, on the temperature gradient. If the host is heated to a critical temperature and damaged by this process, the pulse width dependence should be weak. In either case, whether damage occurs as many small sites or within the host material itself, we would expect a weakening of the pulse width dependence in these cases. Within experimental error, this was observed for some of the oxide films at 0.26μm. A weak time or pulse width dependence and a uniform damage morphology has been observed for damage by 100 nanosecond pulses (14), where the diffusion time is much greater. It should be possible to treat damage in this regime by a collective impurity model such as those given by the Soviet workers (60, 67).

The damage morphology of MgO in Figure (21) appears more like that of the fluoride films. The thermal conductivity of MgO is larger than those of the other oxides and falls within the range of the fluoride conductivities (79). Based on the impurity model it would be expected that the inclusion morphology of the MgO films would be similar to that of the fluoride films. It should also be noted that MgO was the only

oxide material which did not exhibit a uniform morphology at 0.26μm, and was similar to the fluoride morphology at this wavelength.

V. CONCLUSIONS

In the last section fourteen specific observations were made on the experimental data and then examined in terms of each of the theoretical models. The results of this examination are summarized below.

OBSERVATION	POSSIBLE EXPLANATION(S)
1. The damage threshold increases with thinner films	Impurity Model. (Exclusion of larger, easier to damage impurities).
2. Fluoride films show a stronger change in damage threshold with film thickness than oxides.	Impurity Model. (Lower thermal conductivity of oxides results in damage to smaller impurities).
3. MgO and TiO_2 damage thresholds show no pulse with dependence at 1.06μm but do at shorter wavelengths.	Impurity Model. (Mie absorption increases at shorter wavelengths for smaller impurities which have higher thermal diffusion losses. Because of the lower thermal conductivity of oxides a "no pulse width dependence" would be seen in in oxides at longer wavelengths before fluorides).
4. Fluoride film damage thresholds have a stronger pulse width dependence than oxide film damage.	Impurity Model. (Same reason as in 2 and 3). Multiphoton Model. (Higher bandgaps of fluorides than oxides).

5. ZrO_2 damage threshold has no pulse width dependence at any wavelength.

Impurity Model. (Very low thermal conductivity in ZrO_2, about an order of magnitude less than the other oxides).

6. Al_2O_3, SiO_2 and ZrO_2 damage thresholds exhibit weak or no pulse dependent at 0.26μm.

Impurity Model. (Mie absorption increases for smaller impurities to the extent that they collectively damage, resulting in less total energy diffusion loss).

One Photon Absorption. (Linear absorption).

7. MgO has marked damage threshold dependence on pulse width at 0.26μm.

Impurity Model. (Thermal conductivity similar to fluorides).

8. Thin film damage threshold decreases with decreasing wavelength.

Impurity Model. (Mie absorption increases).

Multiphoton Model. (Order of process decreases).

9. The damage threshold of thick films decreases more slowly with decreasing wavelength than thin films.

Impurity Model. (At long wavelengths the larger easy to damage impurities are excluded in the thinner films giving a much higher damage threshold. At shorter wavelengths the smaller impurities are damaged).

Observation	Explanation
10. Damage site size and number density of sites increases with decreasing laser wavelength.	Impurity Model. (Smaller and more numerous impurities are damaged).
11. Change in site size with wavelength is not as sharp for oxides as fluorides except MgO.	Impurity Model. (Lower oxide thermal conductivity, except MgO, results in smaller impurities being damaged).
12. Damage morphology of most oxide films changes at 0.26μm from individual craters to uniform area damage.	Impurity Model. (Same reason as in 6; high density of small impurities.) One Photon Absorption. (Direct band edge absorption.)
13. The damage morphology of TiO_2 becomes uniform at 0.35μm.	Impurity Model. (Same reason as in 12.) One Photon Absorption. (Same reason as in 12.)
14. HfO_2 damage does not fit with the film thickness behavior seen in other materials. The damage morphology of the 1/6λ HfO_2 films is uniform at all wavelengths.	Unexplained.

Of the fourteen observations the impurity model can explain thirteen. Figures (24-27, 30, 31) have also shown that the impurity theory gives more than just a qualitative prediction of the observations (1), (2), (4), (6), (8) and (9). The main issues which are unresolved by this

model are the unusual nature of the data and morphology of the 1/6μm HfO_2 film and the time dependence of HfO_2 at 0.26μm.

There are numerous problems with the avalanche and multiphoton models. These models can not explain the film thickness dependence of damage or in fact items 1-3, 10, 11, 14 and 15. The strong (almost linear) time dependence given by the avalanche model can not explain the dependence observed in the fluorides. Equation (11) from multiphoton theory would indicate that two photon absorption is operative in the fluorides because the observed dependence is close to $(t_p)^{1/2}$. However, if a process is two photon at 1.06μm it would be one photon at 0.53μm and there would be no pulse width dependence. In contrast, a pulse width dependence was observed. A combined avalanche and multiphoton model could explain observations (4) and (8), but the observed pulse width dependence in MgO at 0.26μm would be in contradiction, because two photon absorption at 0.53μm would be one photon at 0.26μm. The uniform morphology observed in the oxides at 0.26μm might be explained by intrinsic two photon absorption; however, the non-existant or weak pulse dependence in Al_2O_3, SiO_2 and ZrO_2 damage conflicts with this. In the final analysis none of the observed trends in the data can be explained in a consistant manner by the avalanche or multiphoton models.

There is another explanation of the uniform morphology in the oxide films (one photon absorption) that should be discussed. The measured absorptance of TiO_2, at 0.35μm was 0.133. At 0.26μm the absorptance of Al_2O_3, SiO_2, ZrO_2, and HfO_2 were 0.151, 0.171, 0.2

and 0.192 respectively. On the other hand the measured values for MgO, CaF_2, MgF_2, and ThF_4 were 0.032, --, 0.036, and 0.012. The linear absorption is comprised mainly of macroscopic impurity absorption and atomic impurity absorption. The first contributor has already been discussed through the Mie absorption cross-section and damage due to this effect is treated by the impurity model. The second contributor is somewhat different. Sparks (95) has given the atomic impurity energy levels of major impurities in many of the materials tested in this research. These energy levels lie in the band gap of the host material. The exact location depends on the particular impurity and the host material. If it is assumed that the atomic impurities are distributed almost uniformly throughout the thin film, then such a morphology at 0.26μm can be explained by one photon absorption and electron promotion to the conduction band from the impurity levels. In either case it could be concluded that the damage morphology at 0.26μm is explained by linear absorption. The correlation between the damage morphology and the measured absorption would also support this conclusion.

Table (8) gives a generalized summary of the results of the comparison between the theories and the experimental data. We conclude that the impurity model gives the best explanation of the experimental data. In fact, the impurity model gives excellent predictions of the trends in the experimental data particularly considering the unknowns which could not be fully incorporated in the model. These unknowns include the exact composition, shape, real and imaginary index of refraction, and number density as a function of size of the impurities.

MODEL / PARAMETER	WAVELENGTH	PULSE LENGTH	FILM THICKNESS
MULTIPHOTON	REASONABLE	POOR	POOR
AVALANCHE	POOR	POOR	POOR
COMBINED	INCONSISTENT	POOR	POOR
IMPURITY	GOOD	EXCELLENT	EXCELLENT

Table 8. Evaluation of the Avalanche, Multiphoton and Impurity Models when Compared to the Experimental Data

These must be known before more accurate predictions of damage thresholds can be calculated with this model. The shape of the impurities is one aspect of the problem that could be dealt with now. Although the shape of the impurities was modeled as a sphere in this research effort, it is known that in many films the impurities grow as columns or cylinders. This particular shape could be treated with Mie calculations at the present time by the model.

Another area of uncertainty in the model is the efficiency of thermal contact between the impurity and the host material. In the model it was assumed that there was perfect contact between the two. In reality the quality of contact may vary with size and type of impurity and composition of the host material.

For completeness the residual film stress must be discussed. When films are deposited, there is a residual stress in the film, which can be either tensile or compressive in form, and varies as a function of film thickness. Figure (14) showed the change in stress with film thickness for MgF_2. This stress can have an influence in all three theoretical models. There was no measured residual stress in the CaF_2 films and yet a marked variation of damage threshold with film thickness was observed. Therefore, the film thickness variation of damage is not due to stress. However, stress may be a factor in breakdown. For example, the residual stress was greater in a 0.25μm MgF_2 film than in a 1μm film. In this case a lower threshold could be obtained for the thin films than for the thick films. This point is substantiated by the work of Guenther, et al. (96) where they found that the damage

threshold decreased when either type of stress was dominant. Although the stress does not support the experimental data at 1.06 and 0.53μm it does not support the data at 0.26μm. The MgF_2 films damaged at a lower threshold for thin films than for thick. It is possible that the low energy densities required for damage at 0.26μm were influenced by the film stress which produced a decrease in damage threshold in the thinner films.

VI. UNRESOLVED QUESTIONS

Some features of the data have not been satisfactorily resolved; for example, it is not clear how to interpret the change in oxide film morphology at 0.26μm. The morphology can be addressed by either the impurity model or linear absorption by atomic impurities. If the uniform morphology was indicative of linear absorption it might help explain the low damage thresholds of the 1/6μm HfO_2 film. This type of morphology was observed at 0.53 and 0.35μm for this film, but not for the other HfO_2 films. The HfO_2 absorptance measurements were not made on the 1/6μm film and there is a possibility that the linear absorption in this film was much higher than in the other films. The SiO_2 films exhibited a strong film thickness dependence in conflict with the other oxide films. It should be noted, however, that this case is unique in that the film and the substrate were the same material. The ZrO_2 films had essentially no pulse length dependence except at 0.26μm. This could only be explained in the impurity model by either poor thermal contact between the impurity and the host material or by an extremely small thermal conductivity of either the host or impurity. The ZrO_2 films also showed the smallest crater sizes for damage at 1.06μm and the weakest change in morphology with wavelength.

In order to obtain better agreement between theory and experiment in future research, the unknown quantities mentioned in the previous section must be included. Most important are the impurity composition and number density as a function of size.

BIBLIOGRAPHY

1. Tenth Symposium of Optical Materials for High Power Lasers, Introduction by A. H. Guenther, NBS Special Publication 541, eds. A. J. Glass and A. H. Guenther, US GPO Washington, D.C., (1978).

2. Molchanov, A. G., "Development of Avalanche Ionization in Transparent Dielectrics Under the Action of a Light Pulse", Sov. Phys.-Solid State 12, No. 3, 749, (1970).

3. Epifanov, A. S., "Avalanche Ionization Induced in Solid Transparent Dielectrics by Strong Laser Pulses", Sov. Phys. JETP 40, No. 5, 897, (1974).

4. Smith, W. L., et al., "Picosecond Laser-Induced Breakdown at 5321 and 3547 A: Observation of Frequency Dependent Behavior", Phys. Rev B 15, No. 8, 4039, (1976).

5. Vinogradov, A. V. and Faizullov, F. S., "Role of Many-Photon and Impact Ionization in the Breakdown of Dielectrics by Picosecond Laser Pulses", Sov. J. Quant. Elect. 7, 650, (1977).

6. Schmid, A., et al., "Multiphoton Theory of Optical Breakdown in Alkali Halides", NBS Special Publication 509, eds. A. J. Glass and A. H. Guenther, US GPO Washington, D.C., (1977).

7. Epifanov, A. S., et al., "Frequency and Temperature Dependences of Avalanche Ionization in Solids Under the Influence of an Electromagnetic Field", Sov. Phys. JETP Lett. 21, No. 8, 223, (1975).

8. Gorshkov, B. G., et al., "Laser Induced Breakdown of Alkali Halide Crystals:, Sov. Phys. JETP 45, No. 3, 612 (1977).

9. Soileau, M. J. and Bass, M., "Optical Breakdown in NaCl and KCl From 0.53 to 10.6μm", Appl. Phys. Lett. 35, No. 5, 370, (1979).

10. Fradin, D. W., et al., "Comparison of Laser Induced Bulk Damage in Alkali-Halides at 10.6, 1.06 and 0.69 Microns", Laser Induced Damage in Optical Materials, NBS Special Publication 372, eds. A. J. Glass and A. H. Guenther, US GPO Washington D.C., (1972).

11. Bass, M., and Barrett, H. H., "Laser Induced Damage Probability at 1.06 and 0.69μm, Laser Induced Damage in Optical Materials, NBS Special Publication 372, eds. A. J. Glass and A. H. Guenther, US GPO Washington D.C., (1972).

12. Porteus, J. O., et al., "Laser Damage Measurements at CO_2 and DF Wavelengths", Laser Induced Damage in Optical Materials, NBS Special Publication 435, eds. A. J. Glass and A. H. Guenther, US GPO Washington D.C., (1975).

13. Newnam, B. E. and Gill, D. H., "Spectral Dependence of Damage Resistance of Refractory Oxide Optical Coatings", Laser Induced Damage in Optical Materials, NBS Special Publication 462, eds. A. J. Glass and A. H. Guenther, US GPO Washington D.C., (1976).

14. Porteus, J. O., et al., "Multithreshold Evaluation of 175 Nano-second Pulsed Laser Damage to Coating Materials at 2.7 and 3.8μm Wavelengths", Laser Induced Damage in Optical Materials, NBS Special Publication 541, eds. A. J. Glass and A. H. Guenther, US GPO Washington D.C., (1978).

15. Newnam, B. E. and Gill, D. H., "Ultraviolet Damage Resistance of Laser Coatings", NBS Special Publication 541, eds. A. J. Glass and A. H. Guenther, US GPO Washington D.C., (1978).

16. McMahon, J. M., "Damage Measurements with Sub-Nanosecond Pulses", Laser Induced Damage in Optical Materials, NBS Special Publication 372, eds. A. J. Glass and A. H. Guenther, US GPO Washington D.C., (1972).

17. Wang, V., et al., "Single and Multilongitudinal Mode Damage in Multilayer Reflectors at 10.6μm as a Function of Spot Size and Pulse Duration", Laser Induced Damage in Optical Materials, NBS Special Publication 435, eds. A. J. Glass and A. H. Guenther, US GPO Washington D.C., (1975).

18. Bettis, J. R., et al., "Spot Size and Pulse Dependence of Laser Induced Damage", Laser Induced Damage in Optical Materials, NBS Special Publication 462, US GPO Washington D.C., (1976).

19. Milam, D., "1064-nm Laser Damage Threshold of Polished Glass Surfaces as a Function of the Pulse Duration and Surface Roughness", Laser Induced Damage in Optical Materials, NBS Special Publication 541, eds. A. J. Glass and A. H. Guenther, US GPO Washington D.C., (1978).

20. Newnam, B. E., et al., "Influence of Standing-Wave Fields on the Laser Damage Resistance of Dielectric Films", Laser Induced Damage in Optical Materials, NBS Special Publication 435, eds. A. J. Glass and A. H. Guenther, US GPO Washington D.C., (1975).

21. Apfel, J. H., et al., "The Role of Electric Field Strength in Laser Damage of Dielectric Multilayers", Laser Induced Damage in Optical Materials, NBS Special Publication 462, eds. A. J. Glass and A. H. Guenther, US GPO Washington D.C., (1976).

22. De Shazar, L. G., et al., "Role of Coating Defects in Laser Induced Damage to Dielectric Thin Films", Appl. Phys. Lett. 23, (1978).

23. Apfel, J. H., "Further Studies of the Role of Electric Field Strength in Laser Damage of Dielectric Layers", Laser Induced Damage in Optical Materials, NBS Special Publication 509, eds. A. J. Glass and A. H. Guenther, US GPO Washington D.C., (1977).

24. Gill, D. H., et al., "Use of Non-Quater Wave Designs to Increase the Damage Resistance of Reflectors at 532 and 1064 Nanometers", Laser Induced Damage in Optical Materials, NBS Special Publication 532, eds. A. J. Glass and A. H. Guenther, US GPO Washington D.C., (1977).

25. Manenkov, A. A., "New Results on Avalanche Ionization as a Laser Damage Mechanism in Transparent Solids", Laser Induced Damage in Optical Materials, NBS Special Publication, eds. A. J. Glass and A. H. Guenther, US GPO Washington D.C., (1978).

26. Soileau, M. J., et al., "Frequency and Spot Size Dependence of Laser Damage in the Mid-IR Region", Laser Induced Damage in Optical Materials, NBS Special Publication 541, eds. A. J. Glass and A. H. Guenther, US GPO Washington D.C., (1978).

27. Aleshin, I. V., et al., "Optical Breakdown of Glass by a Sharply Focused Laser Beam", Sov. Tech. Phys. Lett. 4, No. 7, 348, (1978).

28. Epshtein, E. M., "Scattering of Electrons by Phonons in a Strong Radiation Field", Sov. Phys.-Solid State 11, No. 10, 2213, (1970).

29. Vinogradov, A. V., "Absorption of High-Intensity Light by Free Carriers in Dielectrics", Sov. Phys. JETP 41, No. 3, 540 (1975).

30. Rubinshtein, A. I., and Fain, V. M., "Theory of Avalanche Ionization in Transparent Dielectrics Under the Action of a Strong Electromagnetic Field", Sov. Phys.-Solid State 15, No. 2, 332, (1973).

31. Keldysh, L. V., "Concerning the Theory of Impact Ionization in Semiconductors", Sov. Phys. JETP 21, No. 6, 1135, (1965).

32. Epifanov, A. S., et al., "Theory of Avalanche Ionization Induced in Transparent Dielectrics by an Electromagnetic Field", Sov. Phys. JETP 43, No. 2, 377, (1976).

33. Zakharov, S. I., "Cascade Ionization in Transparent Dielectrics at Optical Radiation Intensities Close to the Breakdown Threshold", Sov. Phys. JETP 41, No. 6, 1065, (1975).

34. Bloembergen, N., "Laser Induced Electric Breakdown in Solids", IEEE J. Quant. Elect. QE-10, 375, (1974).

35. Basov, N. G., et al., "Semiconductor Quantum Generator with Two-Photon Optical Excitation", Sov. Phys. JETP 23, No. 3, (1966).

36. Braunstein, R. and Ockman N., "Optical Double-Photon Absorption in CdS", Phys. Rev. 134, No. 2A, A499, (1964).

37. Hassan, A. R., "Two-Photon Interband Transitions at Critical Points in Semiconductors", Nuovo Cimento L XX B, No. 1, (1970).

38. Kovarskii, V. A. and Perlin, E. Y., Phys. Status Solidi B 45, 47 (1971).

39. Keldysh, L. V., "Ionization in the Field of a Strong Electromagnetic Wave", Sov. Phys. JETP 20, No. 8, 1307, (1965).

40. Jones, H. D. and Reiss, H. R., "Intense-field Effects in Solids", Phys. Rev. B 16, No. 6, 2466, (1977).

41. Narducci, L. M., et al., "One-Photon Keldysh Absorption in Direct-gap Semiconductors", Phys. Rev. 13, 2508, (1976).

42. Yee, J. H. "Four-Photon Transition in Semiconductors", Phys. Rev. B 3, No. 3, 355, (1971).

43. Adduci, F., et al., "Direct and Indirect Two-Photon Processes in Layered Semiconductors", Phys. Rev. B 15, No. 2, 926 (1977).

44. Raizer, Y. P., "Laser Induced Discharge Phenomena (Consultants Bureau, New York), p. 177, (1977).

45. Vaidyanathan, A., et al., "Comparison of Keldysh and Perturbation Formulas for One-Photon Absorption", Phys. Rev. B 20, No. 6, (1979).

46. Vaidyanathan, A., et al., "One-Photon Absorption in Direct Gap Semiconductors", Solid State Commun. 21, 405, (1977).

47. Hopper, R. W. and Ulhmann, D. R., "Mechanism of Inclusion Damage in Laser Glass", Appl. Phys. 41, No. 10, 4023, (1970).

48. Milam, D., et al., "Laser Damage Threshold for Dielectric Coatings as Determined by Inclusions", Appl. Phys. Lett. 23, No. 12, 654, (1973).

49. Sparks, M. and Duthler, C. J., "Theory of Infrared Absorption and Material Failure in Crystals Containing Inclusions", Appl. Phys. 44, No. 7, 3038, (1973).

50. Danileiko, Y. K., et al., "Surface Damage of Ruby Crystals by Laser Radiation", Sov. Phys. JETP 31, No. 1, 18, (1970).

51. Danileiko, Y. K., et al., "The Role of Absorbing Inclusions in Laser Induced Damage of Transparent Dielectrics", Sov. Phys. JETP 36, No. 3, 541, (1973).

52. Anisimov, S. I. and Makshantsev, B. I., "Role of Absorbing Inclusions in the Optical Breakdown of Transparent Media", Sov. Phys. Solid State 15, No. 4. 743, (1973).

53. Milam, D., et al., "Laser Damage Threshold for Dielectric Coatings as Determined by Inclusions", Appl Phys. Lett. 23, No. 12, 654, (1973).

54. Sparks, M. and Duthler, C. J., "Theory of Infrared Absorption and Material Failure in Crystals Containing Inclusions", J. Appl. Phys. 44, No. 7, 3038, (1973.

55. Makshantsev, B. I., et al., "Effect of Absorbing Homogeneities on the Development of Avalanche Ionization", Sov. Phys.- Solid State 16, No. 1, 103, (1974).

56. Danileiko, Y. K., et al., "Role of Absorbing Defects in the Mechanism of Laser Damage of Real Transparent Dielectrics", Sov. J. Quant. Elect. 4, No. 8, 1005, (1975).

57. Zakharov, S. I., et al., "Phenomenology of Formation of Shock Waves in the Volume of a Dielectric by a Focused Monopulse", Sov. Phys.-Dakl. 19 No. 11, 779, (1975).

58. Kovalev, A. A., et al., "Dependence of the Damage Threshold of Polymethylmetacrylate on the Duration of Laser Pulses and Dimensions of Irradiated Region", Sov. Phys. JETP 43, No. 1, 69, (1976).

59. Danileiko, Y. K., et al., "Prethreshold Phenomena in Laser Damage of Optical Materials", Sov. J. Quant. Elect. 6, No. 2, 236, (1976).

60. Aleshin, I. V., et al., "Optical Breakdown of Transparent Media Containing Micro-inhomogeneities", Sov. Phys. JETP 43, No. 4, 631, (1976).

61. Libenson, M. N., "Plasma-chemical Model for Optical Breakdown of Transparent Dilectrics", Sov. Tech. Phys. Lett. 3, No. 5, 180, (1977).

62. Artem'ev, V. V., et al., "Statistics of Microscopic Inhomogeneities and Optical Breakdown of Transparent Media", Sov. Phys. Tech. Phys. 22, No. 1, 106, (1977).

63. Picard, R. H., et al., "Statistical Analysis of Defect Caused Laser Damage in Thin Films", Appl. Opts. 16, No. 6, 1563, (1977).

64. Karpov, O. V., et al., "Interaction of Laser Radiation with a Heterogeneous Medium", Zhurnal Prikladnoi Spektroskopii 29, No. 3, 414, (1978)

65. Lysikov, Y. I., "Calculation of the Kinetics of Propagation of a Powerful Light Beam in a Transparent Dielectric with Impurities", Zhurnal Prikladnoi Mekhanikii Tekhnicheskoi Fiziki, No. 5, 60, (1978).

66. Kosolobov, S. N., et al., "Shock Mechanism for Dissipation of Laser Energy in a Transparent Dielectric with Microscopic Inclusions and Impurities", Sov. Phys. Tech. Phys. 23, No. 9, 1133, (1978).

67. Kovalev, A. A. and Makshantsev, B. I., "Surface Damage Caused by Laser Radiation to Solid Transparent Dielectrics", Sov. J. Quant. Elect. 8, No. 5, 659, (1978).

68. Artem'ev, V. V., et al., "Correlation Between the Radiation Breakdown and Microscopic Inhomogeneities of a Dielectric Coating", Sov. Phys. Tech. Phys. 26, No. 12, 1467, (1978).

69. Kosolobov, S. N., et al., "An Impact Mechanism in Diverting Energy from Absorbing Inclusions at Laser Destruction of Transparent Dielectrics:, Opt. Commun. 24, No. 3, 355, (1978).

70. Morichev, I. E., et al., "Laser Breakdown and Temperature Dependence of Absorption in Quartz", Sov. Phys. Tech. Phys. 23, No. 10, 1254, (1978).

71. Ivanov, L. I., et al., "Laws Governing the Formation of Shock Waves Under the Influence of Laser Emission on the Absorbing Solids", Problemy Prochnosti, No. 6, 99, (1978).

72. Sokolovskiy, R. I. and Tyurin, Y. L., "Absorption of Intense Radiation in a Transparent Dielectric Which Contains Microcontaminants", Izvestiya Vysshikh Uchebnykh Zavedeniy Fizika, No. 6(193), 90, (1978).

73. Leonov, R. K., et al., "Methods of Investigating the Role of Absorbing Microinclusions in Damage to Transparent Dielectrics by Laser Radiation; I. Passive Methods", Sov. J. Quant. Elect. 8, No. 6, 729, (1978).

74. Danilieko, Y. K., et al., "The Mechanism of Laser Induced Damage in Transparent Materials Caused by Thermal Explosion of Absorbing Inhomogeneities", Sov. J. Quant. Elect. 8, No. 1, 116, (1978).

75. Zverev, G. M., "Resistance of Dielectric-coated Interference Mirrors to Laser Induced Damage", Sov. J. Quant. Elect. 8, No. 1, 20, (1978).

76. Zverev, G. M. and Pashkov, V. A., Sov. Phys. JEPT 30, 616, (1970).

77. Austin, R. and Ledger, A. H., Perkin-Elmer, private communications.

78. Humpherys, T. W., et al., "Surface Microanalysis Techniques for Characterization of Thin Films", to be published in Laser Induced Damage in Optical Materials, (1979).

79. Sparks, M. and Duthler, C. J., Theoretical Studies of High-Power Ultraviolet and Infrared Materials, p. 11, Eighth Technical Report, (1976).

80. Goldenberg, H. and Tranter, M. A., "Heat Flow in an Infinite Medium Heated by a Sphere", Brit. J. Appl. Phys., 296, (1952).

81. Van de Hulst, H. C., Light Scattering by Small Particles, John Wiley & Sons, Inc., New York, (1957).

82. Cook, R. J. and Butts, R. R., "Aerosol Induced Thermo-Optical Degradation of a High Intensity Laser Beam", Laser Digest, AFWL-TR-73-273, p. 69, (1973).

83. Bennett, H. S. and Rosasco, G. J., "Resonances in the Efficiency Factors for Absorption: Mie Scattering Theory", Appl. Opts. 17, No. 4, 491, (1978).

84. Rosasco, G. J. and Bennett H. S., "Internal Field Resonance Structure: Implications for Optical Absorption and Scattering by Microscopic Particles", J. Opt. Soc. Am. 68, No. 9, 1242, (1978).

85. Fuchs, R. and Kliewer, K. L., "Optical Modes of Vibration in an Ionic Crystal Sphere", J. Opt. Soc. Am. 58, No. 3, (1968).

86. Metz, H. J. and Dettmar, H. K., Kolloid Z. Z. Polym. 192, 107, (1963).

87. Jackson, J. D., Classical Electrodynamics, John Wiley & Sons, New York, (1966).

88. See previous references to measurement of laser damage thresholds.

89. Fradin, D. W. and Bass, M., "Comparison of Laser Induced Surface and Bulk Damage", Appl. Phys. Lett. 22, No. 4, (1973).

90. Fradin, D. W. and Bass, M., "Electron Avalanche Breakdown Induced by Ruby Laser Light", Appl. Phys. 22, No. 5, (1973).

91. Smith, W. L. and Bechtel, J. H., "A Simple Technique for Individual Picosecond Laser Pulse Duration Measurements" J. Appl. Phys. 47, No. 3, 1976).

VITA

Thomas W. Walker was born on 18 March 1943 in Amarillo, Texas. He obtained his undergraduate degree in Physics from the University of Southern California in 1965. After obtaining his commission in the USAF in 1966, he spent one year at Texas A & M University studying Meteorology. Following a four year tour in Air Weather Service he entered the School of Engineering, Air Force Insititute of Technology and received a Master of Science degree in Engineering Physics in 1972. Subsequently, he was assigned to the Air Force Weapons Laboratory at Kirtland Air Force Base, New Mexico where he performed research on laser propagation in the atmosphere until 1976 when he left to study for his PhD.

UNCLASSIFIED

SECURITY CLASSIFICATION OF THIS PAGE (When Data Entered)

REPORT DOCUMENTATION PAGE — READ INSTRUCTIONS BEFORE COMPLETING FORM

1. REPORT NUMBER: AFIT/DS/PH/80-4
2. GOVT ACCESSION NO.: AD-A096 051
3. RECIPIENT'S CATALOG NUMBER:
4. TITLE (and Subtitle): LASER-INDUCED DAMAGE TO THIN FILM DIELECTRIC COATINGS.
5. TYPE OF REPORT & PERIOD COVERED: PhD Dissertation
6. PERFORMING ORG. REPORT NUMBER:
7. AUTHOR(s): Thomas W. Walker, Major USAF
8. CONTRACT OR GRANT NUMBER(s):

9 Doctoral Thesis

9. PERFORMING ORGANIZATION NAME AND ADDRESS: Air Force Institute of Technology (AFIT/EN), Wright-Patterson AFB, Ohio 45433
10. PROGRAM ELEMENT, PROJECT, TASK AREA & WORK UNIT NUMBERS:
11. CONTROLLING OFFICE NAME AND ADDRESS: Air Force Weapons Laboratory, Kirtland AFB NM 87117
12. REPORT DATE: 11 October 1980
13. NUMBER OF PAGES: 134
14. MONITORING AGENCY NAME & ADDRESS (if different from Controlling Office):
15. SECURITY CLASS. (of this report): Unclassified
15a. DECLASSIFICATION DOWNGRADING SCHEDULE:

16. DISTRIBUTION STATEMENT (of this Report)

Approved for public release; distribution unlimited

17. DISTRIBUTION STATEMENT (of the abstract entered in Block 20, if different from Report)

FREDRIC C. LYNCH, Major, USAF
Director of Public Affairs

17 FEB 1981

18. SUPPLEMENTARY NOTES

Air Force Institute of Technology (ATC)
Wright-Patterson AFB, OH 45433

19. KEY WORDS (Continue on reverse side if necessary and identify by block number)

Laser Damage
Thin Films
Avalanche Ionization
Multiphoton Absorption

20. ABSTRACT (Continue on reverse side if necessary and identify by block number)

The laser-induced damage thresholds of dielectric thin film coatings have been found to be more than an order of magnitude lower than the bulk material damage thresolds. A program was conducted in which thin film damage thresholds were measured as a function of laser wavelength (1.06μm, 0.53μm, 0.35μm and 0.26μm), laser pulse length (5 and 15 nanoseconds), film material and film thickness. The large matrix of data was compared to predictions given by avalanche ionization, multiphoton ionization and impurity theories of laser damage. When Mie absorption cross-sections, and the exact thermal equations were included

DD FORM 1 JAN 73 1473

SECURITY CLASSIFICATION OF THIS PAGE (When Data Entered)

into the impurity theory, excellent agreement with the data was [illegible]. The avalanche and multiphoton damage theories could not account for most parametric variations in the data. For example, the damage thresholds for most films increased as the film thickness decreased and only the impurity theory could account for this behavior. Other observed changes in damage threshold with changes in laser wavelength pulse length and film material could only be adequately explained by the impurity theory. The conclusion which results from this study is that laser damage in thin film coatings results from absorbing impurities included during the deposition process.

DATE
ILMED
-8